Tidal forcing and internal tide energetics around Svalbard: a numerical study

UNIVERSITY OF BERGEN
GEOPHYSICAL INSTITUTE

Master's Thesis in Physical Oceanography

Aleksander Dürr Libæk

June 2020

Abstract

The hydrostatic and linear Regional Ocean Modeling System (ROMS) is used to examine the tidal forcing and the resulting baroclinic response and energetics of internal tides generated around Svalbard in the Arctic Ocean. In this region, the warm Atlantic water flows into the Arctic Ocean over variable bathymetric features, such as the Yermak Plateau and the continental slope and shelf break of Svalbard, where barotropic tidal velocity amplitudes of up to $0.5\,\mathrm{m\,s^{-1}}$ occur. Along its poleward path, vertical mixing processes contribute to removing heat from the Atlantic water. This research aims to quantify the tidal response in terms of, barotropic to baroclinic energy conversion and baroclinic energy dissipation using a realistic stratification distribution from autumn 2017, and forced separately by the dominant diurnal and semidiurnal tidal constituents. Tidal energetics are enhanced in distinct regions: the Yermak Plateau is dominated by the luni-solar and the principal lunar diurnal tides (K_1 and O_1), and the continental shelf and slope northeast of Svalbard by the principal lunar and solar semidiurnal tides (M_2 and S_2). The volume-integrated and time-averaged K_1 energy conversion and dissipation of the tide in the Yermak Plateau region is 780 MW (31 % of the barotropic tidal energy input), whereas the M_2 at the continental slope northeast of Svalbard is 70 MW (2 %). Over the sloping bathymetry, conversion mainly occurs in the $0.7-1.8\,\mathrm{km}$ isobath range (upper and central slope), where radiation of internal waves is highly limited by rotational constraints. Generally, a substantial part of the converted energy dissipates locally in the $1.5-2.5\,\mathrm{km}$ isobath range (central and lower slope), implying an important contribution to vertical mixing and the evolution of water mass properties in the region.

Acknowledgments

Jeg vil benytte anledningen til å gi en stor takk til de som har bidratt til arbeidet med masteroppgaven min. Aller først vil jeg takke min hovedveileder professor Ilker Fer som tok med meg på tokt nord for Svalbard og ga meg veiledning og motivasjon under dette prosjektet. Jeg vil også takke min medveileder Zoé Koenig for verdifulle innspill og alltid tilgjengelig for diskusjon. Mange takk til Malte Müller som har sørget for god data og gitt meg et større innblikk i modellering.

Takk til medstudenter og undervisere for fem lærerike år med spennende feltarbeid og ekskursjoner. Ikke mist vil jeg takke venner og familie for å ha gitt meg god støtte gjennom hele studietiden.

Contents

List of Abbreviations

AEDB Arctic Environmental Drifting Buoy. 36

AOBC Arctic Ocean Boundary Current. ii, 58, 60

APE Available Potential Energy density. 14, 24, 25, 32, 45, 51

AROME-arctic Application of Research to Operations at MEsoscale arctic model. 17

AW Atlantic Water. 1–3, 21, 22, 58, 60, 61, 63

BC Baroclinic. 31, 42, 43, 50

BT Barotropic. 31, 42, 43, 50

CEAREX Coordinated Eastern Arctic Experiment. 39, 55, 59

CFL Courant-Friedrichs-Lewy criterion. 18, 19

CICE The Los Alamos Sea Ice model. 17

HKE Horizontal Kinetic Energy density. 14, 23–26, 32–34, 44–46, 51, 54

HYCOM HYbrid Coordinate Ocean Model. 17

IBCAO International Bathymetric Chart of the Arctic Ocean. 17

NBS Nansen Basin Slope. 4, 22, 44, 47, 51, 56–58, 61–63

NBSs Nansen Basin Slope section. 4, 20, 21, 24, 47–49, 53, 57, 59, 60

ROMS Regional Ocean Modeling System. 5, 17, 18, 51, 54, 62, 63

SB Spitsbergen Bank. 4, 20, 22, 24–26, 31, 51, 52, 58, 62, 63

SBs Spitsbergen Bank section. 4, 20–22, 24, 26, 28–31, 53, 54, 61

TOPAZ4 Ocean-sea ice data assimilation system for the North Atlantic and Arctic. 5, 17

WSC West Spitsbergen Current. 2, 3, 61

XBT Expendable Bathythermograph. 17

YP Yermak Plateau. 3, 4, 20, 22, 24, 32, 34–37, 41, 42, 49, 54–59, 61–63

YPNs Yermak Plateau Northern section. 4, 20–22, 24, 32, 37, 39, 40, 53, 59

YPSs Yermak Plateau Southern section. 4, 20–22, 24, 35–38, 53, 58, 60, 61

List of Figures

1 Introduction

Ocean mixing is an important player in the global ocean circulation. The main sources of mixing are tides and winds which provide a portion of their energy in mixing both the upper and lower ocean layers. The astronomical gravitational attraction generates surface (barotropic) ocean tides, which interacts with bathymetric features such as continental slopes, plateaus and ridges. This interaction generates perturbations in the stratified water column which propagate as (typically linear) internal waves. Such waves are a supply for mechanical energy and as they break they lead to dissipation and mixing in the abyssal ocean and are important to maintain the deep ocean stratification. Munk and Wunsch (1998) proposed a global tidal energy flux budget where 3.5 TW ($1\,\mathrm{TW} = 10^{12}\,\mathrm{W}$) total tidal energy is lost in the ocean. Of the total tidal energy lost, approximately 2 TW is dissipated in shallow marginal seas through bottom friction, while the remaining portion is lost in the deep ocean. By inferring dissipation from a global tidal model, Egbert and Ray (2001) have confirmed that approximately 1 TW, or $25\,\% - 30\,\%$ of the global total tidal energy, is lost in the deep ocean. The observed global deep ocean diapycnal diffusivity is on the order of $10^{-5}\,\mathrm{m^2\,s^{-1}}$, which is one order of magnitude lower than required to sustain the global stratification and deep water formation (Munk and Wunsch, 1998).

When a barotropic tide flows over topography, a fraction of the barotropic tidal energy is lost by bottom friction to local dissipation, whereas the rest is used up to generate internal (baroclinic) wave energy. Thereafter, the internal wave energy is partly radiated away from generation and conversion site, and partly lost to dissipation locally or away from generation site where energy flux convergence occurs (Kang and Fringer, 2012). The potential for the internal wave conversion rate depends on the bottom topography, tidal currents and stratification. The rate of dissipation of propagating internal wave energy is influenced by shear instability, scattering to higher frequency and higher wave number waves over mid-ocean rough topography or at the continental shelf break (Martini et al., 2011), and wave-wave interaction (Müller et al., 1986) including parametric sub harmonic instability (Hibiya and Nagasawa, 2004).

The Arctic Ocean is a region sensitive to climate change. The inflow of warm Atlantic Water (AW) and its variability can affect Arctic sea ice. Even though the mixing rates in the Arctic Ocean are dominated by small double diffusion fluxes and lateral intrusions (Sirevaag and Fer, 2012), there has been observed local enhanced mixing rates that are related to topography and barotropic tides (Padman and Dillon, 1991).

At the latitude of the Arctic Ocean, most linear internal tides cannot propagate freely and

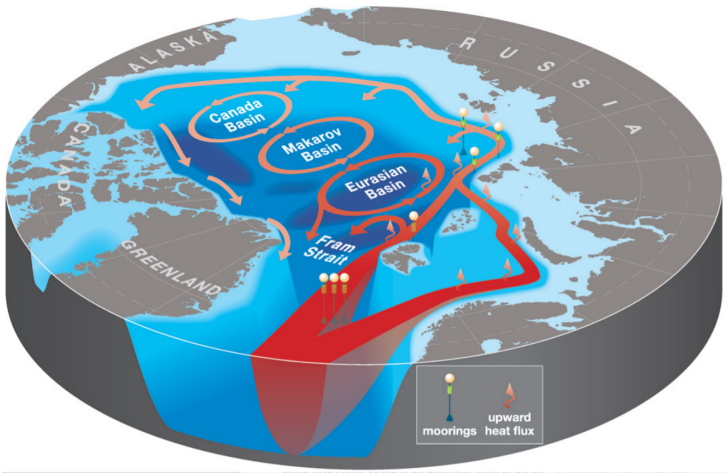

Figure 1: Arctic circulation pattern where the Atlantic Water (red path) enters the Arctic in Fram Strait. While propagating cyclonically along the continental slope and the Arctic, the upward heat fluxes decrease (less and less red). Surface circulation is shown in blue and pacific intermediate water in (pink/blue) (from Carmack et al. (2015)).

either propagate along topography guidelines or dissipate locally creating hotspots of increased turbulence. Holloway and Proshutinsky (2007) stated that the global climate models do not reproduce the coupling between ocean and ice/atmosphere in the Arctic. Analyzing only the barotropic tides, Holloway and Proshutinsky (2007) found that tidal currents created highly variable stress at the ice/water interface and increased the ocean heat flux to the ice cover. This influenced the local extent and retreat rate of sea ice. Further, results depending on baroclinic waves increased the stress divergence with amplifying effects on sea ice (Koentopp et al., 2005). A sensitivity study, specifically with higher spatial resolution, is required to better quantify the impact of tides in the Arctic. Today, it is unclear how far internal tides generated at the different Arctic regions travel before being dissipated and how much they contribute to enhanced mixing at the boundaries.

The regional focus of this study is around Svalbard where the warm inflow into the Arctic can be affected by mixing driven by tides. The interaction of surface tides with bathymetric features around Svalbard can generate interior mixing that modifies water mass properties as well as sea ice distribution (Meyer et al., 2017). This is a key region for an inflow of warm and salty AW in the West Spitsbergen Current (WSC) that enters the Arctic Ocean and subducts below the fresh and cold surface water (Figure 1). In the WSC, at the western slope of Bear Island (Figure 2 at 74°5′ N) the AW core has been observed to reach almost the surface centered at

the slope (Boyd and D'Asaro, 1994). The WSC brings the AW northwards along with the shelf break (Svalbard branch) and cools rapidly as its core subducts in Fram Strait and further north of Svalbard (81° N). On the pathway towards the Arctic, the Yermak Plateau (YP) function as an obstacle for the inflow of the AW (Figure 2). When the flow reaches the YP, the AW splits into branches as isobaths diverge. Above the 1500 m isobath, one branch recirculates in Fram Strait and the remaining makes up the Yermak branch along the outer flanks of the YP (Manley, 1995). Another branch, the Yermak Pass branch, is a short cut across the YP at about 80°8′ N, and is observed to have a relatively strong volume transport in winter compared to summer (Koenig et al., 2017, Crews et al., 2018). Thereafter, the Yermak branch and the Yermak Pass Branch merge with the Svalbard branch along the continental slope north of Svalbard (Koenig et al. 2017, Menze et al., 2019). Further downstream, the warm boundary current joins with a flow through the Barents Sea and flow together along the Arctic Basin's upper slope and oceanic ridges.

The barotropic tides travel along the coast of Svalbard cyclonically or anticyclonically around amphidromic points. The two most dominating tidal components that show the largest spatial variability over the YP, north-west of Svalbard, are the lunar semidiurnal tide M_2 and the luni-solar diurnal tide K_1 (Fer et al., 2015). The transfer of energy from internal waves in the ocean is an important mechanism to sustain high levels of mixing on the continental shelf slopes, at the shelves and over plateaus. Internal waves can break and enhance turbulence-driven diapycnal mixing. Breaking occurs at a small scale where vertical shear of horizontal currents associated with internal tides or with other internal waves are sufficiently energetic to cause instability and turbulence (Garrett and Kunze, 2007). The stratification acts as a barrier for upward heat flux from the AW towards the atmosphere or the sea ice. One possibility that can reduce this barrier is vertical mixing driven by tidal forcings, such as that observed over the continental slope north of Svalbard (Rippeth et al., 2017) or in general along the Arctic margins (Rippeth et al., 2015). The dissipation rate across the AW thermocline varies significantly with bathymetry and is modulated by tidal forcing (Rippeth et al., 2015). Resulting dissipation rates imply significant turbulent mixing and are important for the exchange of water masses between the warmer AW and the colder surface layer. Further, these vertical fluxes associated with the uplift of underlying water with phytoplankton and nutrients into the sunlit layer of the upper ocean can lead to enhanced productivity (Denman, 1976).

Internal waves observed around Svalbard are not always at the forcing tidal frequency, but with shorter wavelength and higher frequency. These are typically lee waves generated at regions

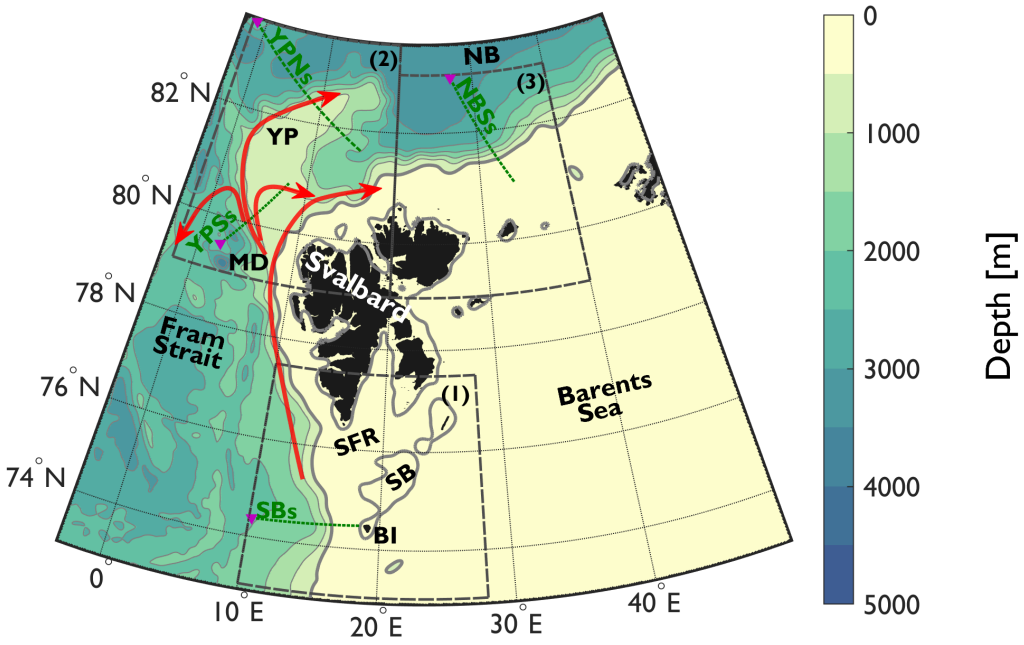

Figure 2: Bathymetry around Svalbard with thick gray contours at 100 m and 500 m depth, and thereafter at intervals of 500 m with thin gray contours. The red arrows represent the pathways of the Atlantic Water across and around the Yermak Plateau. Places marked are Fram Strait to the west covering the Molloy Deep (MD) and the Yermak Plateau (YP), Nansen Basin (NB) to the north. Barents Sea to the southeast with Spitsbergen Bank (SB), Storfjordrenna (SFR) and Bear Island (BI). The region is divided into three numbered subdomains: (1) SB, (2) YP and (3) Nansen Basin Slope (NBS) where each subdomain has sections (green stippled lines) defined as SB section (SBs), YP Southern section (YPSs), YP Northern section (YPNs) and NBS section (NBSs).

with strong tidal currents where a topographic feature has less width than the tidal excursion. Lee waves have different properties than the baroclinic tidal waves. Further more, near-inertial waves, generated in response to variable wind forcing, can force and accelerate currents and induce turbulent mixing in other regions of rough topography where at present tidal flows are too weak for lee wave formation (Rippeth et al., 2017).

In this thesis, results from a numerical model are used to characterize and quantify the tidal forcing and the associated linear internal wave energy fluxes, energy conversion rates and dissipation rates as a source of energy for mixing around Svalbard. The aim is to identify regions of enhanced barotropic to baroclinic conversion rates and hotspots of vertical mixing that can have consequences for the heat budget in the region. For this purpose, the output from

the Regional Ocean Modeling System (ROMS) is analyzed, including fields from one-month long experiments forced separately with different tidal constituents. The forced tides are the principal lunar and solar semidiurnal (M_2 and S_2) and the luni-solar and lunar diurnal (K_1 and O_1) constituents. The model domain has 2.5 km horizontal resolution and 42 vertical depth levels, and covers the Barents Sea, Fram Strait and parts of the Nansen Basin. The model is forced by output from 12 km resolution TOPAZ4. Based on the output from the model, three subdomains shown in Figure 2 have been identified for further analysis. The study provides a comprehensive picture of internal tides characteristics in regions around Svalbard.

Relevant theory about internal waves, their conversion rate and radiation is given in section 2. Section 3 describes the numerical model setup with represented tidal forcing and validation. Section 4 gives the results of the barotropic tide interaction with the different topographies regionally. These are discussed in section 5 in the context of other energy sources for mixing and of global relevance. A summary with a conclusion is given in section 6.

2 Background and Theory

When the stable equilibrium state of the interface between air and water is perturbed, horizontally propagating surface waves are generated at the sea surface owing to the gravity force. Similarly, waves can also be generated between different density layers within the ocean. The internal stratification from temperature and salinity variations is weaker than the stratification between air and water, which causes these internal waves to not only propagate horizontally at the interfaces but also vertically, across the interfaces. Depending on the scale of motion, the Earth's rotation inflicts a deflecting motion with a fictitious force, called the Coriolis force that is perpendicular to the velocity vector. The Coriolis force can act as a restoring force producing inertial waves. When both the Coriolis force and the gravity force take part in the restoring motion, the waves are called inertia-gravity waves and are referred to as 'internal waves' hereafter.

The source of internal waves can be difficult to trace because of nonlinear interactions (Staquet and Sommeria, 2002). Mainly, it is winds and tides that force internal waves. The perturbation needed to generate internal tides lies in the origin of the barotropic flow from the astronomical tide generating forces. These forces and the corresponding barotropic tidal energy can be measured from the gravitational pull of the Moon, and to some extent, the Sun. When the horizontal tidal current flows over bathymetric slopes, a vertical component must emerge at every tidal cycle. This gives rise to a baroclinic response, allowing pressure fluctuations to travel across isopycnals. Isopycnic surfaces are displaced upward and downward in the water column, in response to emitted internal waves at tidal frequency. These waves transport energy, with or without actual transport of matter, both horizontally and vertically. A significant loss of energy may occur over ridges in the open ocean and on the continental slopes and shelves. Barotropic tide over bathymetric slopes is one way of exciting internal waves. Another important generation mechanism is the impulsive atmospheric forcing (Alford et al., 2011). The near-inertial internal wave field, generated in response to wind forcing is expected to be weak in ice-covered waters (Rainville et al., 2011). The wind generated internal waves are not considered in this study, and we will focus on the tidal forcing.

Two important approximations to the total equation of motion are used, the traditional and the Boussinesq approximation. When using the traditional approximation, the Coriolis terms involving the cosine of latitude is neglected. The Boussinesq approximation assumes that the density variations can be neglected, which is appropriate for all near-incompressible fluids, and

only accounted for in the buoyancy term where vertical variation of density is important.

2.1 Total Equations of Motion

The study of internal waves in a continuously stratified fluid can be expressed with the Reynolds-averaged momentum equation, the buoyancy equation and the continuity equation, using the traditional and Boussinesq approximations (Cushman-Roisin and Jean-Marie, 2011):

$$u_t + \mathbf{u} \cdot \nabla u - fv = -\frac{1}{\rho_0} p_x + \nabla_H \cdot (\nu_H \nabla_H u) + (\nu_V u_z)_z \,, \tag{2.1}$$

$$v_t + \mathbf{u} \cdot \nabla v + fu = -\frac{1}{\rho_0} p_y + \nabla_H \cdot (\nu_H \nabla_H v) + (\nu_V u_z)_z \,, \tag{2.2}$$

$$w_t + \mathbf{u} \cdot \nabla w = -\frac{1}{\rho_0} p_z + \nabla_H \cdot (\nu_H \nabla_H w) + (\nu_V u_z)_z + b \,, \tag{2.3}$$

$$u_x + v_y + w_z = 0 \,, \tag{2.4}$$

$$b_t + wN^2 = 0 \,, \tag{2.5}$$

where subscripts x, y, z, t denote partial derivative in space and time, $\mathbf{u}\,(x, y, z, t) = \{u, v, w\}$ are the velocity in the horizontal and vertical direction, respectively, p is the pressure, $\rho_0 = 1027\,\mathrm{kg\,m^{-3}}$ the reference density, $b = -g\rho/\rho_0$ the buoyancy, ρ the density, and N^2 the buoyancy frequency squared related to the stability of the water column, created by ocean internal stratification (Cushman-Roisin and Jean-Marie, 2011). The buoyancy frequency is

$$N(z) = \left(-\frac{g}{\rho_0} \rho_{\theta z} \right)^{1/2} \,, \tag{2.6}$$

where ρ_θ is the background potential density at depth z. The buoyancy frequency can vary from $\mathcal{O}(10^{-4})\,\mathrm{s^{-1}}$ ($0.06\,\mathrm{cph}$, $1\,\mathrm{cph} = 2\pi/3600\,\mathrm{s^{-1}}$) in weakly stratified deep waters to $\mathcal{O}(10^{-2})\,\mathrm{s^{-1}}$ ($5.7\,\mathrm{cph}$) in the pycnocline. The peak in buoyancy frequency often corresponds to the largest gradient in density which depends on temperature, salinity and pressure. The internal wave propagation inflicts small elevations and depression of the sea surface. Compared to the excursion in the ocean interior, the surface signature is very small due to a larger density gradient from ocean to the atmosphere. This small sea surface elevation variability modifies the roughness of the sea surface and can be detected by satellites.

The free surface is at $z = \eta$, and the bottom is described by $z = -h(x, y)$. The pressure is related to the surface displacement via the hydrostatic balance, $p|_{z=0} = g\eta$. The boundary conditions can then be written as a linear free surface condition where $w|_{z=0} = \eta_t$ at the surface

where $\eta \ll h$ is required (Kelly et al., 2010). At the bottom, the condition is no normal flow where $w|_{z=-h} = -h_x u|_{z=-h} - h_y v|_{z=-h}$.

2.2 Barotropic and baroclinic decomposition

2.2.1 Tidal amplitude and phase

Specific movements of the Earth, Moon and Sun produce patterns in the overall tidal motion that can be extracted based on the unique frequency inflicted by individual astronomical tidal forcing. The tidal wave signal is built up of superpositioned sinusoids symbolized as harmonic constituents (Doodson and Lamb, 1921), and this build-up is produced by the mathematical procedure called Harmonic Analysis. The amplitude and phase of each harmonic are unique to the location due to coastal boundaries and bathymetry, and need to be extracted. The model is forced through a specific surface elevation, density anomaly and horizontal current velocity induced by tides at the boundaries of the domain with tidal frequency ω. This forcing can be expressed by the following equation,

$$\xi = \xi_a \, cos(\omega t + \phi_\xi) \; , \tag{2.7}$$

where ξ denotes different variables such as the tidal surface displacement amplitude η_a with phase ϕ_η, the density tidal amplitude ρ_a with phase ϕ_ρ, and the horizontal tidal velocity amplitudes (u_a, v_a) with phases (ϕ_u, ϕ_v).

2.2.2 Depth and time-averaging

When a fluid parcel is excited, a restoring force pushes the parcel back toward the equilibrium position, which may overshoot because of its inertia and be pushed back, thus generating an oscillation. There are two forces at present, the reduced gravity (buoyancy force) and the Coriolis force due to the Earth rotation. The propagating internal waves can be identified by subtracting the depth average (barotropic) pressure and horizontal velocity from the total value. This represents the perturbed (baroclinic) pressure and velocity (Kunze et al., 2002).

The decomposition of surface and internal tides require depth averaging expressed as

$$\frac{1}{h}\overline{(\cdot)} = \frac{1}{h}\int_{-h}^{0} (\cdot) \, dz \; , \tag{2.8}$$

where h is the water column thickness (total depth) and $\overline{(\cdot)} = \int_{-h}^{0}(\cdot) \, dz$ is the operator for depth-integration. Over variable spatial gradients of bottom elevation, a depth average of horizontal

gradients is expressed using the Leibniz's notation and the product rule, resulting in

$$\frac{1}{h}\overline{(\cdot)}_x = \frac{1}{h}\overline{(\cdot)} + \frac{h_x}{h}\left[\frac{1}{h}\overline{(\cdot)} - (\cdot)|_{z=-h}\right] , \tag{2.9}$$

where h_x is the horizontal gradient of bottom elevation. Eq. (2.9) reduces to Eq. (2.8) over flat bottom. Time-averaging over a period T in time t is defined as

$$\langle(\cdot)\rangle = \frac{1}{T}\int_t^{t+T}(\cdot)\,dt . \tag{2.10}$$

2.2.3 Horizontal velocity decomposition

The horizontal velocity $\mathbf{u}_H$ is decomposed into a zonal and meridional component u and v, respectively (positive in the east and north direction). Further, decomposing these into surface and internal wave parts is expressed as

$$\mathbf{u}_H = \mathbf{U}_H + \mathbf{u}'_H , \tag{2.11}$$

where the surface tidal velocity $\mathbf{U}_H = \{U, V\}$ is the depth average of $\mathbf{u}_H$ using Eq. (2.8) and $\mathbf{u}'_H = \{u', v'\}$ is the residual after the depth average, i.e. perturbation wave velocity.

2.2.4 Pressure decomposition

The decomposition of pressure is in the same manner defined as the total pressure as a sum of its depth average and perturbations, $p(x, y, z, t) = P + p'$. The surface and internal tide pressure do not individually satisfy the boundary equation that is produced by depth-integrating the continuity equation using Eq. (2.8) over variable bottom elevation (in one direction):

$$(hU)_x + \eta_t = 0 , \tag{2.12}$$

where η_t is the time-varying surface displacement. When not taking into account for this boundary equation, a spurious energy conversion term occurs in the energy balance equations. The internal tides do not individually satisfy Eq. (2.12) as a linear free-surface boundary condition which states that the surface tide is responsible for all surface displacement and volume convergence. The decomposition is suitable for normal modes over flat bottom and the shallow water equations. For the internal tide, this becomes a rigid-lid approximation and the corresponding depth average over topography is consistent. The pressure decomposition includes now additionally a p^η term representing the contribution to spurious energy removal expressed as

$$p^s(x, y, z) = P + p^\eta , \tag{2.13}$$

$$p^i(x, y, z) = p' - p^\eta , \tag{2.14}$$

where p^s and p^i is the surface and internal tide pressure, respectively. The elimination procedure of this spurious energy conversion is derived in Kelly et al. (2010), and the resulting internal tide pressure accounting for this is expressed as

$$p^\eta(x,y,z) = \int_0^z b^\eta \, dz \; , \tag{2.15}$$

where b^η is the internal wave buoyancy force due to the spurious energy conversion. The internal wave buoyancy force and its inflicting change to the internal wave vertical velocity are

$$b^\eta(x,y,z) = \eta_t \left(\frac{z+h}{h} \right) \; , \tag{2.16}$$

$$w^\eta(x,y,z) = -N^2 \eta \left(\frac{z+h}{h} \right) \; . \tag{2.17}$$

2.3 Internal wave equation

The study of internal waves in a continuously stratified fluid is expressed through the linearized momentum equation, the continuity equation and the buoyancy equation with the Boussinesq, f-plane and hydrostatic approximations with decomposition into a barotropic and a baroclinic part representing the surface and internal wave field, respectively. We assume plane waves in (x,z) with no change in y-direction. Following the methodology in Kelly et al. (2010), the surface tide momentum and buoyancy equations are

$$U_t - fV = -\frac{1}{\rho_0} p^s_x - (D - p^\eta_x) \; , \tag{2.18}$$

$$0 = -\frac{1}{\rho_0} p^\eta_z + b^\eta \; , \tag{2.19}$$

$$b^\eta_t + w^\eta N^2 = 0 \; , \tag{2.20}$$

where D is the internal-wave drag due to sloping topography

$$D(x) = \frac{-h_x}{h} p'|_{z=-h} \; . \tag{2.21}$$

By applying linearization and hydrostatic approximation to the total momentum Eqs. (2.1, 2.2 and 2.5) and removing the surface tide, Eqs. $(2.18 - 2.20)$ produce the internal tide equations

$$u'_t - fv' = -\frac{1}{\rho_0} p^i_x + (D - p^\eta_x) \; , \tag{2.22}$$

$$0 = -\frac{1}{\rho_0} p^i_z + (b - b^\eta) \; , \tag{2.23}$$

$$(b - b^\eta)_t + (w - w^\eta) N^2 = 0 \; . \tag{2.24}$$

An equation for the vertical velocity w is useful for describing internal waves in a continuously stratified fluid. We eliminate u and v from Eqs. (2.1 and 2.2) using the time derivation of the continuity Eq. (2.4), and thereafter eliminate ρ in Eqs. (2.3 and 2.5). We then eliminate p by taking the Laplacian. This results to a single equation for w:

$$\nabla^2 w_{tt} + f^2 w_{zz}^2 + N^2 \nabla_H^2 w = 0 \,, \tag{2.25}$$

where ∇^2 is the Laplace operator in 3 directions and ∇_H^2 only in the horizontal. If we take another variable (e.g. pressure) instead of the vertical velocity as the unknown, it can be shown to satisfy the same equation. The choice of choosing the vertical velocity lies in the easy interpretation of the boundary conditions.

Further, solution to Eq. (2.25) can be expressed using the wavenumber vector $\boldsymbol{\kappa} = k\vec{x} + l\vec{y} + m\vec{z}$, where k and l are the horizontal wavenumbers in x- and y-direction respectively, and m is the vertical wavenumber in z-direction. A possible sinusoidal wave solution in x-direction is

$$w(x, z, t) = W(z) e^{i(kx - \omega t)} \,, \tag{2.26}$$

where $W(z)$ is a vertical structure function and ω is the wave frequency. Substituting the suggested solution into Eq. (2.25) gives an ordinary differential equation

$$W_{zz} + k^2 \left[\frac{N^2(z) - \omega^2}{\omega^2 - f^2} \right] W = 0 \,. \tag{2.27}$$

The method of vertical modes is used to represent the variables as a superposition of orthogonal modes. This distinguishes surface tide from the internal tide which requires flat horizontal boundary conditions. Applying these boundaries and solving Eq. (2.27) gives a set of eigenvalues c_n with corresponding eigenfunctions W_n where n represents the mode number (Gerkema and Zimmerman, 2008). The same procedure can be done for the pressure shown by Brink (1989b) in which the superposition of the modes represents the general solution only if the orthogonality relation

$$\delta_{nm} \Gamma_n = \frac{1}{f} \left(\int_{-h}^{0} p_n p_m \, dz|_{s=0} + \int_{0}^{\infty} \frac{dh}{ds} \, p_n p_m \, ds|_{z=-h} \right) \tag{2.28}$$

is satisfied when the magnitude of the cross product Γ_n is zero for mode $m \neq n$ between the pressure mode p_n and p_m. The δ_{nm} is the Kronecker-delta, and s the along-shelf distance (Musgrave, 2019). Kelly et al. (2010) takes into account and approximate the modal solution due to the dynamically coupling between the surface and internal tide in Eq. (2.12). The ocean's boundary confines the propagation of internal waves as a waveguide. The internal waves act as standing waves in the vertical while solutions exist for eastward propagation (k^+) and westward propagation ($k^- = -k^+$).

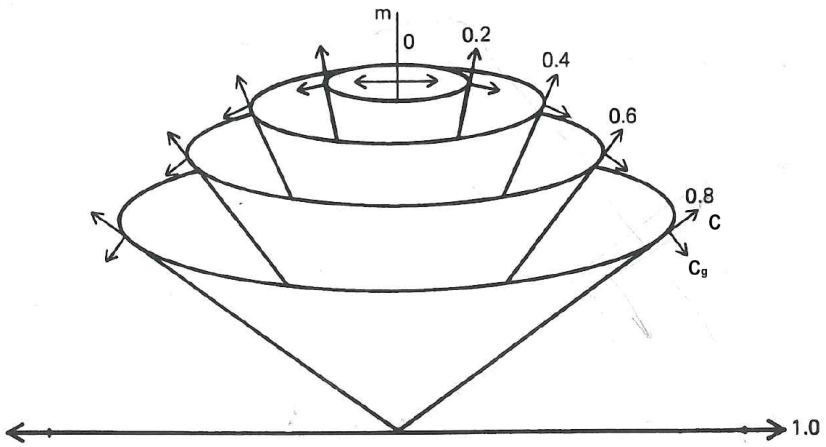

Figure 3: Internal wave surfaces of constant frequency in wavenumber space adapted from Gill (1982). The contours are values of wave frequency to buoyancy frequency, ω/N. The phase velocity $\mathbf{c}$ is parallel to the cones surface, thus the wavenumber vector, whereas the group velocity $\mathbf{c}_g$ is perpendicular to the wavenumber vector.

2.3.1 Dispersion relation, group velocity and phase velocity

The dispersion relation is found substituting $w = e^{i(kx+mz-\omega t)}$ into Eq. (2.25), giving a relation between wavenumber and frequency. By converting to polar coordinates, where θ is the angle between the wave vector and the vertical, it can be shown that

$$\cot^2\theta = \frac{\omega^2 - f^2}{N^2 - \omega^2}\,. \tag{2.29}$$

The velocity for phase propagation of the waves is defined as $\mathbf{c} = \omega/\boldsymbol{\kappa}$, whereas the group velocity is defined as $\mathbf{c}_g = \omega_{\boldsymbol{\kappa}}$. These two velocities have unequal magnitude, where it follows from Eq. (2.29) that the wave frequency depends on the direction θ of the wavevector and not on its wavenumber $\boldsymbol{\kappa}$. Therefore, the group velocity vector must be perpendicular to the lines of constant phase $\mathbf{c}_g \perp \boldsymbol{\kappa}$, and the group velocity direction makes an angle θ from the vertical. This can be visualized in the wavenumber space shown in Figure 3 taken from Gill (1982). The surfaces of constant ω are shown as cones where the group velocity is at right angle to the wavenumber vector, thus to a cone's surface. Consequently, energy propagates along the group velocity vector, at an angle θ between the vertical wavenumber axis and the cone's surface. According to the phase, the fluid particles oscillate forward and backward along the cone's surface.

2.3.2 Critical latitude

For linear internal waves to propagate, ω must be confined between the inertial frequency f and the buoyancy frequency N, implied by Eq. (2.29). This leads to a singularity at the critical latitudes where the inertial frequency f (Coriolis parameter) equals to the wave frequency ω (Vlasenko et al., 2012). Outside of this region, the vertical and horizontal derivatives of the structure function $W(x, y, z)$ will have different signs if the term confined by square brackets is positive. The propagation of linear plane internal tides is only possible equatorward from a critical latitude (Fer et al., 2015). The critical latitudes are $85°46'$, $74°30'$ and $30°$ for S_2, M_2 and K_1, respectively. At these latitudes and northward, the rotation becomes important, and no linear plane-wave solution is allowed when the wave equation changes from hyperbolic to elliptic (Vlasenko et al., 2012). Over continental slopes and other bathymetric features favorable for barotropic to baroclinic energy conversion, the action of Coriolis force will trap the internal tides topographically (zero horizontal group velocity normal to isobaths) at the critical latitude and poleward (Fer et al., 2015). These resulting waves are called bottom-trapped internal tides. A large fraction of such internal tides will dissipate locally near the conversion site with exponential cross-isobath decay.

Background currents can alter the critical latitude by several degrees due to added relative vorticity. Positive relative vorticity will move the critical latitude poleward while negative relative vorticity moves it equatorward. This is not considered in the current analysis since the exact impact is not well known (Dong et al., 2019).

2.4 Energy balance equations

Energy from the barotropic tide is lost through viscous friction and conversion into and radiation of internal tides. The potential energy can be converted into kinetic energy that ultimately ends up in mixing. Following Kang and Fringer (2012), this can be presented using the barotropic and baroclinic energy equations. The depth-integrated and time-averaged barotropic and baroclinic energy equations are derived from the product of the surface tide momentum equation (Eqs. $2.18 - 2.20$) with $\rho_0 \mathbf{U}_H$, and the internal wave momentum equation (Eqs. $2.22 - 2.24$) with $\rho_0 \mathbf{u}'_H$, respectively. These are individually expressed as (averaged in time):

$$\langle(\overline{E_{Hk0}} + \overline{E_{p0}})_t\rangle + \nabla_H \cdot \overline{\langle \mathbf{F}_0 \rangle} = -\overline{\langle C \rangle} - \overline{\langle \epsilon_0 \rangle} \ , \tag{2.30}$$

$$\langle(\overline{E_{Hk}}' + \overline{E_p}')_t\rangle + \nabla_H \cdot \overline{\langle \mathbf{F}' \rangle} = \overline{\langle C \rangle} - \overline{\langle \epsilon' \rangle} \, . \tag{2.31}$$

The energy is partitioned into 4 apparent terms, beginning from left: the tendency, flux divergence, barotropic to baroclinic energy conversion, and energy dissipation as the last term. These different terms will now be explained considering the linear theory.

Assuming a steady state, the time-varying tendency term is zero. Depth-integrated and time-averaged total kinetic energy (KE) and total potential energy (PE) are defined as the sum of their barotropic and baroclinic parts as

$$KE = \overline{\langle E_{Hk0} \rangle} + \overline{\langle E'_{Hk} \rangle} \,, \tag{2.32}$$

$$PE = \overline{\langle E_{p0} \rangle} + \overline{\langle E'_{p} \rangle} \,, \tag{2.33}$$

where E_{Hk0} is the horizontal barotropic kinetic energy density, E'_{Hk} the horizontal baroclinic kinetic energy density (HKE), E_{p0} the barotropic tidal perturbed potential energy density defined as density disturbance from the undisturbed state, and E'_p the available potential energy density (APE) defined as a small portion of potential energy that can be converted into kinetic energy and is then available for contributing to mixing (Chen et al., 2013). By following Holloway and Merrifield (1999) and from linear theory with assuming slowly varying stratification, the time-averaged internal wave energy density over a wave period is defined as

$$\langle E' \rangle = \langle E'_p \rangle + \langle E'_{Hk} \rangle = \frac{1}{4} \rho_b \left[N^2 \, \zeta_a^2 + {u'_a}^2 + {v'_a}^2 \right] , \tag{2.34}$$

where the vertical displacement amplitude $\zeta_a^2 = b^2/N^4$, $\rho_b(x, y, z)$ is the background density, and (u'_a, v'_a) is the perturbed horizontal velocity amplitudes. The time-averaged barotropic energy density over a wave period is

$$\langle E_0 \rangle = \langle E_{p0} \rangle + \langle E_{Hk0} \rangle = \frac{1}{4} \rho_0 \left[\, g \eta_a^2 + h(U_a^2 + V_a^2) \, \right] , \tag{2.35}$$

where η_a is the surface displacement amplitude, U_a and V_a are the amplitude of the barotropic wave velocity, ρ_0 is a reference density and h is total depth.

In internal wave energetics, the energy flux term $\mathbf{F}$ is used for identifying sources, sinks and wave propagation of energy (Kang and Fringer, 2012). The horizontal divergence of energy flux $\nabla_H \cdot \overline{\mathbf{F}}$ is decomposed into two terms where $\nabla_H \cdot \overline{\mathbf{F}_0}$ defines the available barotropic energy for baroclinic energy conversion, and $\nabla_H \cdot \overline{\mathbf{F}'}$ defines the portion of the baroclinic energy conversion that is radiating from the conversion site. The flux divergence is also called the radiation. Regarding the energy flux, the dominating part in producing kinetic energy for linear, hydrostatic

waves is given by

$$\overline{\mathbf{F}_0} = \mathbf{U}_H h \rho_0 g \eta + \overline{\mathbf{U}_H p'} \,, \tag{2.36}$$

$$\overline{\mathbf{F}'} = \overline{\mathbf{u}'_H p'} \,. \tag{2.37}$$

This standard approach of flux calculations is only treated for hydrostatic pressure fluctuations (Nash et al., 2005). The advection and diffusion generated energy fluxes and the non-hydrostatic pressure work have been neglected. The portion of the barotropic energy that is converted into baroclinic energy is called the conversion term, estimated from barotropic and baroclinic energy equations, as

$$C = -p'|_{z=-h}\, \mathbf{U} \cdot \nabla_H h \,, \tag{2.38}$$

where $-p'|_{z=-h}$ is the baroclinic pressure at the bottom. The conversion is a sink and a source in the barotropic and baroclinic equations, respectively. In the conversion term, the non-hydrostatic part is neglected compared to Kurapov et al. (2003). Finally, the dissipation term ($\epsilon = \epsilon_0 + \epsilon'$), in the barotropic and baroclinic energy balance equations is derived as the residual at steady state after calculating the radiation and conversion terms.

2.5 Relevant nondimensional parameters

When internal tides are generated, their evolution is governed by different parameters. The 6 independent dimensional variables are used: ω, f, N, k_h, h_0 and U_0, where $1/k_h$ is the horizontal scale of the topography, U_0 the cross-shelf barotropic velocity amplitude, and h_0 the topographic amplitude. By combining these variables, four key dimensionless parameters are obtained which can characterize internal tide generation. The first parameter is the ratio of the topographic slope to the slope of the wave

$$\alpha = \frac{\gamma}{\theta} \,, \tag{2.39}$$

where $\gamma = |\nabla_H h|$ is the topographic slope, and $\theta = \sqrt{(\omega^2 - f^2)/(N^2 - \omega^2)}$ is defined by the wave characteristic slope from Eq. (2.29). When the slope of the topography is smaller than the characteristic slope ($\alpha < 1$), the topography is called subcritical where internal wave propagation is towards shallower water. For the opposite ($\alpha > 1$), the topography is called supercritical slope where internal wave propagation is towards deep water. A continental slope has commonly both subcritical and supercritical topography which gives transitions where the topography is critical ($\alpha = 1$).

The second dimensionless parameter is the tidal excursion parameter given as

$$\beta = \frac{U_0 k_h}{\omega} \, . \tag{2.40}$$

This parameter represents the ratio of the tidal excursion U_0/ω to an approximated sinusoidal topographic length scale $1/k_h$. When the excursion is larger than the topographic length scale ($\beta > 1$), lee wave formation is expected (Garrett and Kunze, 2007). When the excursion is smaller than the topographic length scale ($\beta < 1$), internal tides are generated at the forcing frequency.

The third dimensionless parameter is the Froude number defined by

$$Fr = \frac{U_0}{N h_0} \, . \tag{2.41}$$

After the tidal flow has slackened and the depression of tidal flow is released, the movement of propagating internal tide is controlled by the Froude number (Holloway and Merrifield, 1999). The Froude number measures the ratio of barotropic to baroclinic wave speed and is related to the horizontal scale of the topography to the internal tide. The Froude number is helpful to investigate the role of non-linearity of the wave. When $Fr \ll 1$, linear theory is valid with a generation of propagating internal waves or steady lee waves, while for $Fr \simeq 1$ or larger, non-linearity becomes important with allowed generation of bores, solitary waves and unsteady lee waves.

The ratio of the barotropic amplitude to the initial depth of the incoming barotropic wave before meeting the slope is given as

$$\nu = \frac{h_0}{h_i} \, . \tag{2.42}$$

When the topographic height is much smaller than the incoming depth ($\nu \ll 1$), the energy conversion tends to be small, while for $\nu \to 1$ and further increasing, the conversion rate tends to increase for subcritical slope.

The last important non-dimensional parameter is the Burger number which compares the buoyancy force with the Coriolis force, expressed as

$$B = \frac{N^2 \, h \, k_h}{f^2} \, . \tag{2.43}$$

For plateaus, seamounts and continental shelf-slopes where trapped internal waves are inhabited, the dynamics are essentially barotropic when $B \ll 1$ and baroclinic when $B \gg 1$ (Thomson and Emery, 2014).

3 Numerical experiment

The numerical experiment in this study is conducted using the Regional Ocean Modeling System (ROMS) (Shchepetkin and McWilliams, 2005) coupled fully with the sea ice model (CICE). ROMS is a 4 dimensional, primitive equations, free-surface, terrain-following ocean model with gridded vertical layers and horizontal orthogonal curvilinear coordinates. The hydrostatic approximation is used in ROMS where the horizontal scales of motions are taken as much greater than the vertical scales. The internal tides meet this criterion in the absence of wave breaking and steepening into highly nonlinear (solitary) waves (Carter et al., 2008). The presence of the latter features can be identified with a hydrostatic model, but can not be accurately described (Holloway and Merrifield, 1999).

The model is forced by the large-scale ocean data assimilation system TOPAZ4 which uses ensemble Kalman filter. IBCAO is used for constructing the coastline which lies in the European Arctic domain between latitude 72° N and 84° N and longitude 5° W and 70° E. A one autumn month period in 2017 is studied with an initial field at rest from version 2.2 of the HYbrid Coordinate Ocean Model (HYCOM). The HYCOM model uses a 24-hour model forecast of background stratification, velocity field and sea surface height assimilated by the Navy Coupled Data Assimilation system. The system assimilates available satellite altimeter observations, satellite and in-situ sea surface temperature as well as in-situ vertical temperature and salinity profiles from XBTs, Argo floats and moored buoys. These fields at the lateral boundaries are relaxed spatially and temporally to monthly climatology within 20 grid cells and e-folded over 30 days times the mixed layer depth divided by 15 m.

The initialization of the barotropic M_2, S_2, K_1 and O_1 tides requires spatial maps of tidal amplitudes and phases. These data are from the TOPEX/Poseidon altimeter and are further processed in an inverse model described by Egbert et al. (1994) and further by Egbert and Erofeeva (2002). The data are obtained from the Oregon State University TOPEX/Poseidon 7.2 Global Inverse solution database.

An hourly atmospheric forcing is applied to ROMS at an equal horizontal resolution of 2.5 km produced by the AROME-arctic weather forecasting system. AROME-arctic has an improved representation of the convective-scales at the surface and in the representation of the stable boundary layer, compared to the global ones (Müller et al., 2017), which gives a more accurate computation of momentum and heat fluxes to the ocean and sea ice.

In computation, the governing equations used in the model require a discretization method of

the derivatives into an algebraic expression. A frequently used technique is the finite-difference method in which discrete intervals replace the infinitesimal differentials. The use of this method can induce nonphysical properties to the model solution, and limiting the resolution in time and space is necessary (Warner, 2011).

The differencing scheme is stable if the time step of the relevant oceanographic process is resolved inside the discrete spatial grid. The stability criterion on the space and time differencing is called the Courant-Friedrichs-Lewy (CFL) criterion. The upper limit of resolution is chosen by the amount of computational power available for the simulation to be efficient enough for producing the data. The spatial grid is equidistant with a resolution of 2.5 km. Li et al. (2015) showed with a global assessment that a 10 km horizontal resolution model captured the two first modes of M_2 and K_1 tide which have been argued to account for $60-90\,\%$ baroclinic wave energy of propagating internal tides (Simmons et al., 2003). However, the wavelength of the internal tide depends on stratification and latitude through buoyancy and Coriolis frequency. As the wavelength approaches infinity near the critical latitude, bottom trapped waves are expected and the associated dispersion relation is different. A truncation error arises due to replacing the spatial and time derivative in the Taylor series expansion, thus it quantifies the accuracy of the model representing the continuous function. The truncation error also includes the approximation of a finite number of steps to approximate an infinite process.

The standard setup of the vertical grid in ROMS is a generalized terrain-following coordinate system where the vertical coordinate transformation is given by

$$z(x,y,\sigma,t) = S(x,y,\sigma) + \zeta(x,y,t)\left[1 + \frac{S(x,y,\sigma)}{h(x,y)}\right] , \tag{3.1}$$

$$S(x,y,\sigma)) = h_c\sigma + [h(x,y) - h_c]\, B(\sigma) , \tag{3.2}$$

where $S(x,t,\sigma)$ is a nonlinear vertical transformation functional, $h(x,y)$ is the unperturbed water depth, σ is a fractional vertical stretching coordinate, $B(\sigma)$ is a stretching function, and h_c is a thickness controlling the stretching. The sigma-coordinate avoids the step-structure inflicted at the bottom when using z-coordinates. From the other side, the z-coordinate applies higher resolution in the desired depth range of oceanographic processes, and particularly, is used in the upper part of the deep ocean where the sigma-grid is coarser (vertical distances between each grid point generally increase away from the continental shelves). A disadvantage with the sigma-grid is its representation of horizontal pressure gradients that inflict difficulties since sigma-surfaces are not horizontal. The S-coordinate is similar to the general sigma-coordinate models with the advantage of lower resolution in the abyss and higher resolution towards coastal areas, which

provides an accurate representation of vortex stretching terms regarding coastal-trapped wave dynamics and bathymetric coastal steered currents (Chassignet and Verron, 2006). In addition, the S-coordinate transformation offers different options of vertical grid distribution which can be weighted towards the bottom or surface as with the z-coordinates. In a sensitivity study to the number of sigma-levels, increasing the number of sigma-levels from 41 to 81 had a negligible effect on the depth-integrated baroclinic energy flux (Holloway and Merrifield, 1999).

A rectangular grid on a spherical Earth is inadequate for scales on the order of basin circulation and larger. The difficulties are related to the convergence of the meridians near poles with smaller zonal grid spacing leading to complications with the CFL condition. Another implication with the use of spherical coordinates is the singularity at the pole in horizontal derivatives (Bentsen et al., 1999). To avoid these, a short time step needs to be applied where 1 hour steps are sufficient. The model has a horizontal structured staggered Arakawa-C grid with boundary fitted, orthogonal curvilinear coordinates applied. The use of a curvilinear coordinate transformation is advantageous for fluids that are confined horizontally within an irregular region. The C-grid resolves the inertia-gravity waves, but afflicts the geostrophy due to the off-set displacement between west-east and south-north velocity in the grid. C-grid has a good representation of Kelvin waves where density perturbation is resolved parallel to solid boundaries (Griffies et al., 2000). At the horizontal step-wise coastline, a wall boundary condition is set to the free slip case. The change in horizontal grid spacing from 2 to 4 km has shown to affect the peak value of the depth-integrated baroclinic energy flux of around 30 % (Holloway and Merrifield, 1999). Applying a higher resolution of 1 km showed only 5 % decrease from the 2 km grid case. Holloway and Merrifield (1999) found that the energy density at the topography generally increased with coarser resolution, where the peak value increased 80 % from 1 to 2 km and 75 % from 2 to 4 km grids. This was emphasized that further studies on generated internal waves in a near field tidal response requires at least 1 km grid spacing.

In time, the hydrostatic primitive equations of momentum are determined by applying a split-explicit time-stepping scheme in which the fast modes (barotropic) and the slow modes (baroclinic) are separated. Then, aliasing of frequency is avoided if the barotropic field is averaged before they replace the values made with a longer baroclinic step. A third order accurate predictor (Leap-Frog) and corrector (Adams-Molten) time discretizing is used in all equations.

A detailed analysis of energetics is attempted in areas around Svalbard to quantify the contribution of different regions in providing energy fluxes and dissipation locally and remotely.

The Svalbard domain (Figure 2) is divided into 3 subdomains which have shown a stronger prevalence of barotropic to baroclinic energy conversion. The first subdomain covers the SB with the Spitsbergen Bank section (SBs) across the western shelf. The second subdomain covers the YP with two sections, the Yermak Plateau Southern section (YPSs) across the southern flank and the Yermak Plateau Northern section (YPNs) across the northern flank. The last subdomain confines the continental slope north-east of Svalbard where a section called the Nansen Basin Slope section (NBSs) is made across the shelf. The section positions are fixed where strong horizontal kinetic energy with represented energy fluxes has been quantified with a resulting energy dissipation contributing to mixing. Harmonic analysis will be applied to the four main harmonic tidal constituents M_2, S_2, K_1 and O_1 for the analysis.

4 Results

We first present the hydrography in sections selected along the pathway of the AW flow, and regional barotropic tidal forcing for each constituent together with the regional internal kinetic and available potential energy. We then present the internal tide energetics in identified subdomains. Section location and the subdomains are shown on the map in Figure 2.

4.1 Hydrography and regional energetics overview

Figure 4 shows the Conservative Temperature (Θ, left panels) and Absolute Salinity (S_A, right panels) along the four sections SBs, YPSs, YPNs and NBSs defined in section 3. The panels

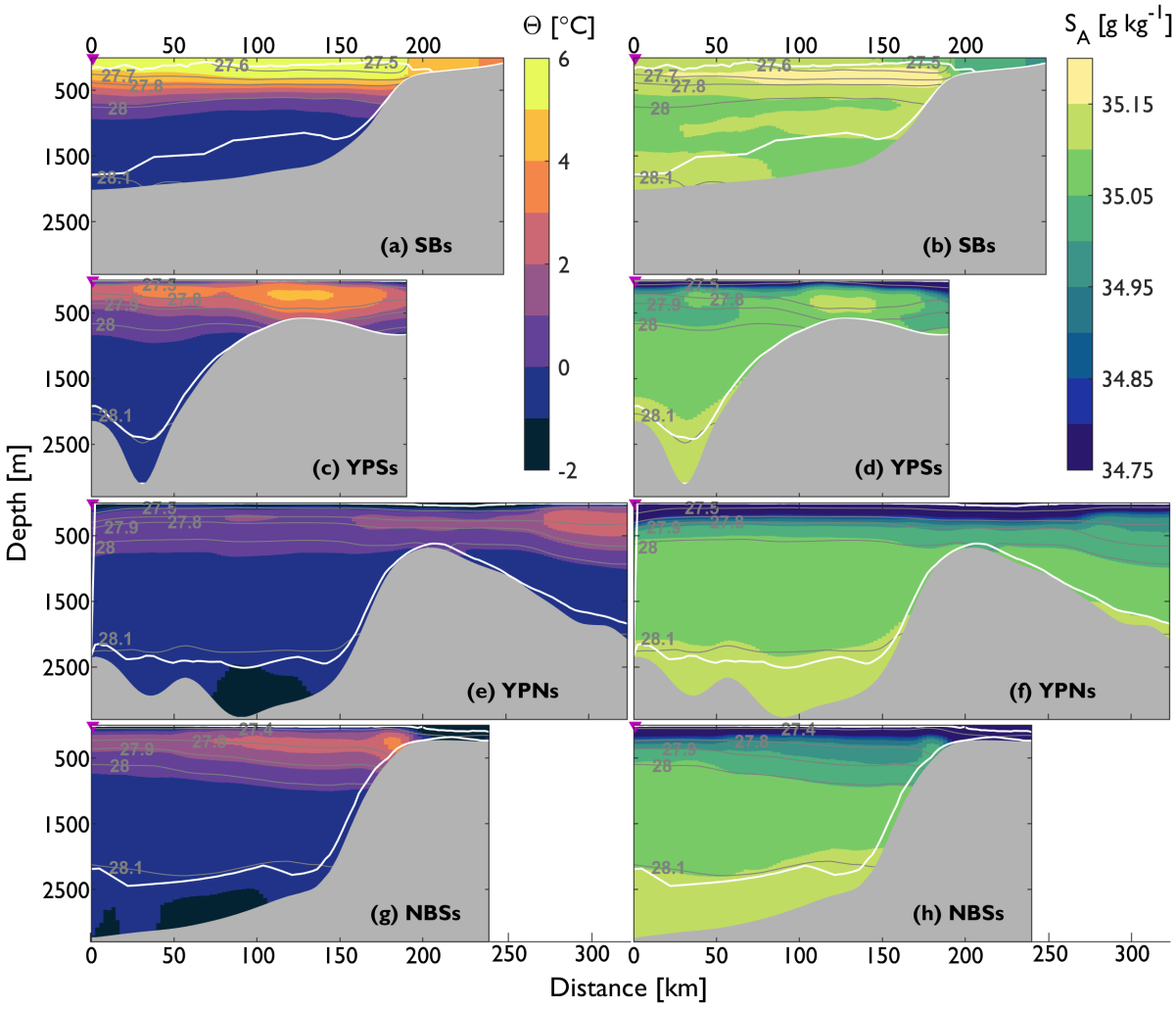

Figure 4: Conservative Temperature (Θ, left panels) and Absolute Salinity (S_A, right panels) for each section. Gray lines are constant potential density levels. Surface and bottom mixed layers are shown with white lines.

are organized so that top panels are upstream and bottom panels are downstream with respect to the AW inflow. The warmest and most saline water is found in the southernmost section, SBs, occupying the layer above the continental shelf with temperatures above 6° C and with Absolute Salinity above 35.1 g kg^{-1}. The salinity maximum is found off-shelf and slightly above the level of the continental shelf (Figure 4b). Both the salinity and temperature decrease towards shallower depths.

In general for the other sections, the temperature decreases and salinity increases with depth except for a few locations where a subsurface maximum of temperature and salinity are found at the shelf break. At these locations, the isopycnals tend to curve downwards when approaching the shelf break and upwards above the temperature and salinity maxima, revealing a relatively mixed region of the water column. As the warm AW is brought farther north, the temperature and salinity of the AW core decreases. From the YPSs towards the YPNs, the AW temperature differs by $\sim 2°$ C at 250 m depth above the plateau. Also, the large salinity in the AW core is

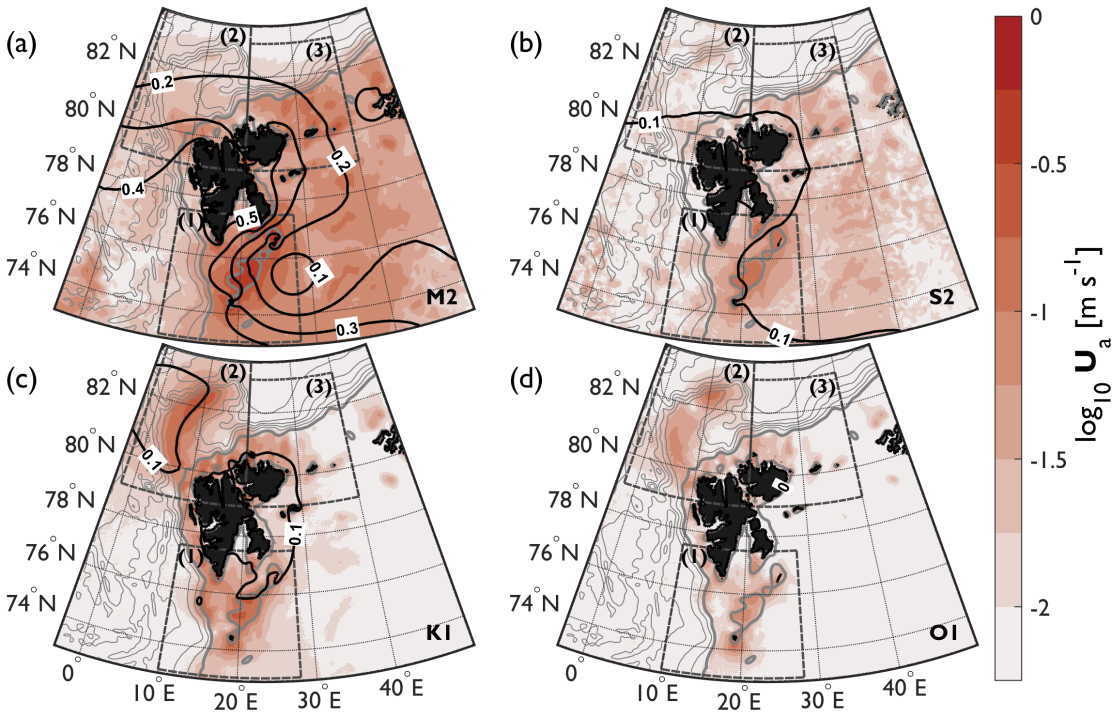

Figure 5: Barotropic tidal velocity amplitude [m s^{-1}] (colors) for each tidal constituent with a logarithmic color scale. Surface displacement amplitude [m] is shown with black thick lines. Subdomains analyzed and discussed in this study are: (1) SB, (2) YP and (3) NBS. Thick gray lines are the 100 and 500 m bottom contours, and thereafter gray thin lines are drawn every 500 m.

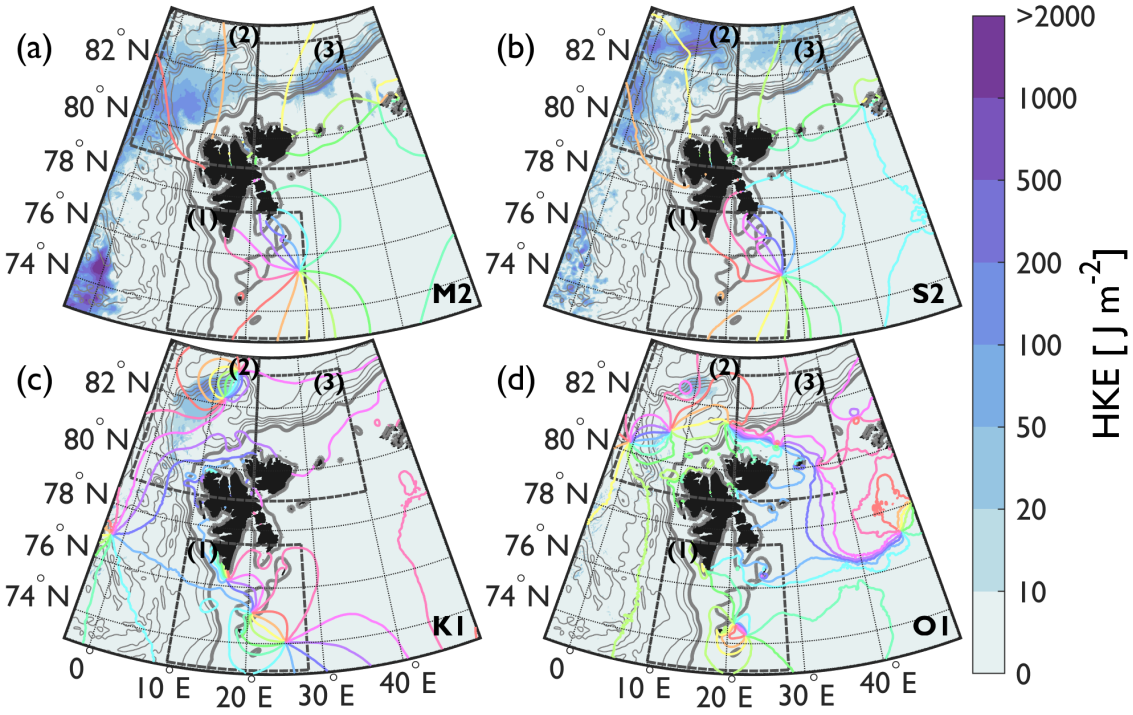

Figure 6: Depth-integrated and time-averaged baroclinic HKE [$\mathrm{J\,m^{-2}}$] ($\langle\overline{E'_{Hk}}\rangle$). Note the non-linear color scale. Colored contours are cotidal lines of surface amplitude phases plotted every 30° where the red and orange lines are the 0° and 30° cotidals, respectively. See Figure 5 for bottom contours and subdomains.

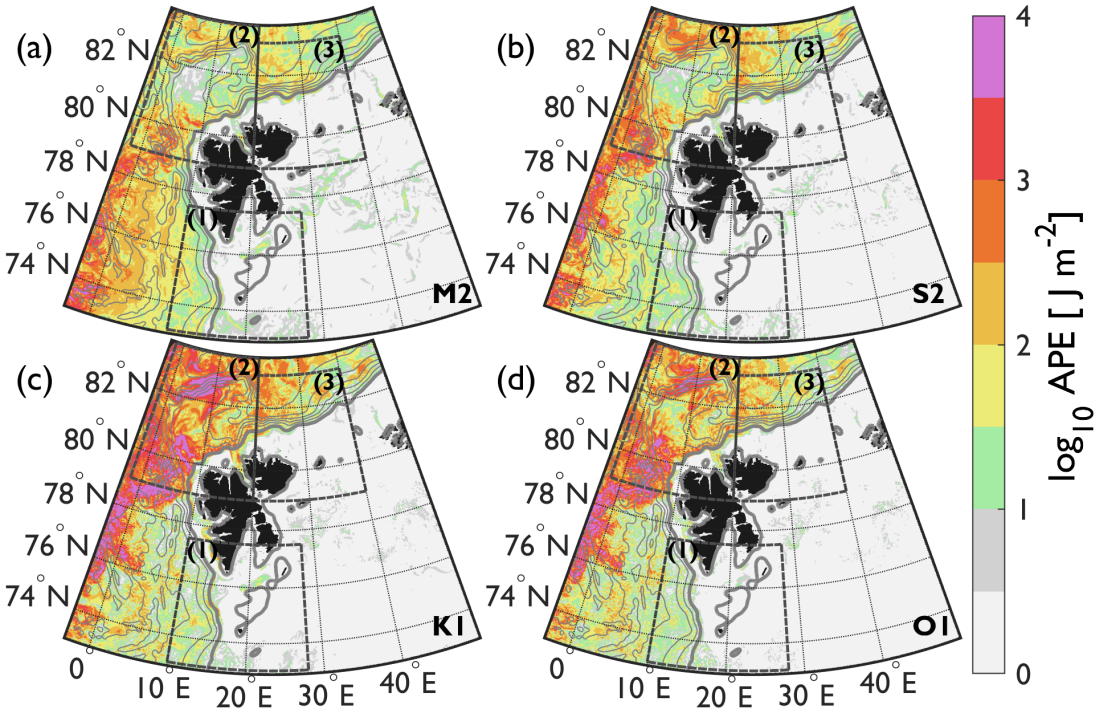

Figure 7: Available potential energy density [$\mathrm{J\,m^{-2}}$] ($\langle\overline{E'_p}\rangle$) (logarithmic color scale) for the four constituents. See Figure 5 for bottom contours and subdomains.

present at the YPSs whereas at the YPNs the maximum is smaller. The NBSs is warmer than the YPNs, suggesting that most of the NBSs originates from the SBs.

Regional distribution of barotropic tidal forcing in the model is obtained using harmonic analysis. Tidal current amplitude ($\mathbf{U}_a$) and surface displacement amplitude (η_a) are shown in Figure 5 for each constituent. The semidiurnal constituents have large barotropic velocity amplitude with wide coverage, especially in shallow regions such as the Barents Sea and the continental shelves of Svalbard, where the SB is particularly energetic. The diurnal barotropic current and surface displacement amplitudes are relatively restricted to specific places such as the YP and parts of the SB, which are locally intensified. The depth-integrated and time-averaged baroclinic HKE ($\langle\overline{E'_{Hk}}\rangle$) and APE ($\langle\overline{E'_p}\rangle$) are shown in Figure 6 and 7, respectively. These energetics show that each constituent is forced locally where the HKE is enhanced in subdomain 2 and 3 over steep slopes in particular. The APE is large over these steep slopes and for deep ocean depths, whereas it tends towards zero in shallow regions. Further investigation of the barotropic forcing, HKE and APE of the three subdomains defined in section 3 are explored separately, since the energetics are on a different scale.

4.2 Spitsbergen Bank, Subdomain 1

Around the SB, high frequency internal waves have been observed in earlier studies where 71 % of the barotropic tidal energy is converted to baroclinic waves (Rippeth et al. (2017)). In subdomain 1, the M_2 barotropic forcing is largest over the SB (Figure 5) where the barotropic tidal ellipse is approximately rectilinear (not shown) with the main axis oriented approximately in the south-west to north-east direction. A barotropic current that sweeps back and forth across the slope is favorable for barotropic to baroclinic conversion. The dominant M_2 barotropic tidal velocity amplitude, taken as the average of mean total velocity amplitude, has a cross-shelf component of $\sim 0.7\,\mathrm{m\,s^{-1}}$ over the shallow regions of SB (Figure 5). The other constituents are comparable at the center of the bank, but enclose a smaller area. In the southern region on the continental slope towards Fram Strait with bottom depths exceeding 500 m, $\mathbf{U}_a$ is less than $0.1\,\mathrm{m\,s^{-1}}$ for all constituents.

The thick lines of Figure 5 for the M_2 constituent show tidal surface displacement amplitude that exhibits large displacement at the bank increasing west- and northward and decreasing east- and southward. Despite the large surface displacement amplitude of 0.4 m with resulting $\mathbf{U}_a > 0.1\,\mathrm{m\,s^{-1}}$, the depth-integrated and time-averaged baroclinic HKE is small and less than $10\,\mathrm{J\,m^{-2}}$ (Figure 6). The internal wave equation (Eq. 2.27) is not satisfied in the layers of low

stratification, $N(x, y, z) \leq \omega$, and the resulting internal wave solution is trapped between the surface and bottom mixed layers, and reflects at these boundaries. In the calculations, the APE and the baroclinic energy flux in the mixed layers have been set to zero. This leads to APE values of zero at the central SB until the 500 m isobath (Figure 7). In general, the APE increases towards the open ocean for bottom depths deeper than 2000 m. At the western slope of SB from 500 m and below, M_2 shows relatively larger APE at the southern slope, whereas K_1 has more pronounced values farther north along the slope with a maximum of $10^3\,\mathrm{J\,m^{-2}}$ occurring at the 500 m isobath.

The irregular shapes of continents and the elliptical Earth's rotation make up different am-

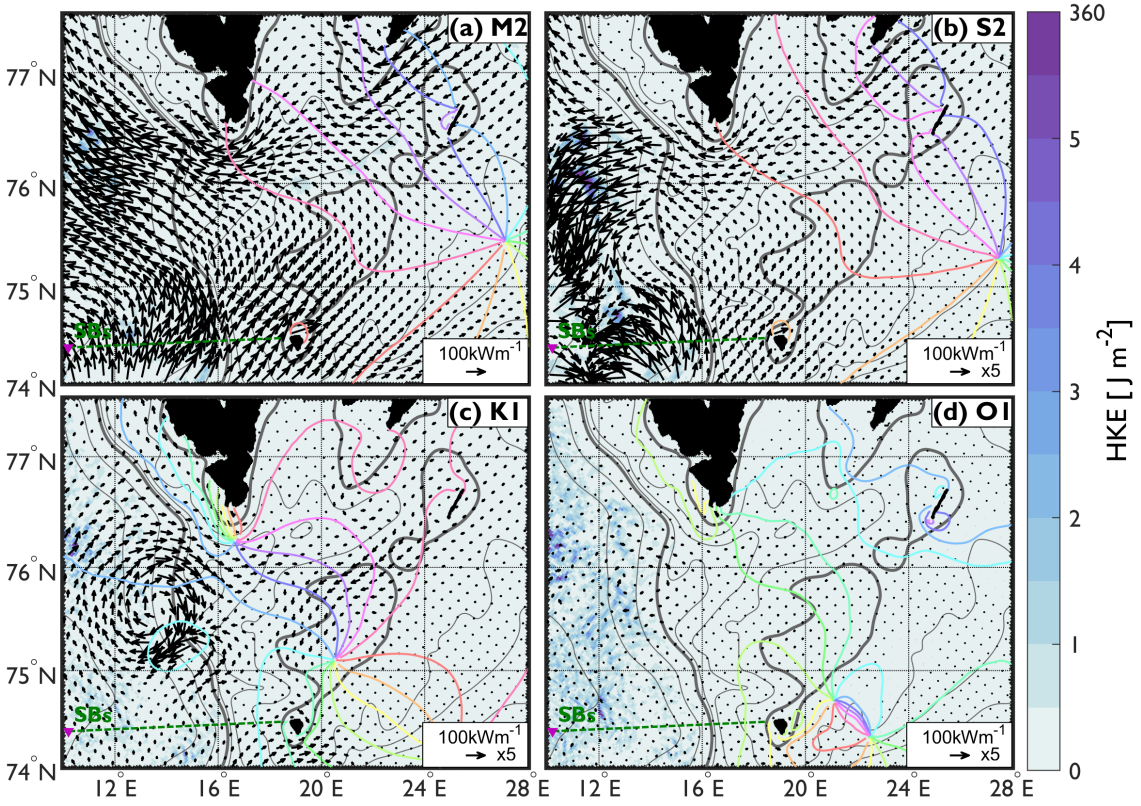

Figure 8: Depth-integrated and time-averaged baroclinic HKE [$\mathrm{J\,m^{-2}}$] ($\langle\overline{E'_{Hk}}\rangle$) colored in background at the Spitsbergen Bank (subdomain 1). Maximum value is $15\,\mathrm{J\,m^{-2}}$ for bottom depths of 2000 m in (b). Barotropic energy flux ($\langle\overline{\mathbf{F}_0}\rangle$) is shown with arrows where (b), (c) and (d) are multiplied by 5 and all with a reference scale of $100\,\mathrm{kW\,m^{-1}}$. Colored contours are cotidal lines of surface amplitude phases plotted every 30° where the red and orange lines are the 0° and 30° cotidals, respectively. The 100 m and 500 m isobaths are shown with thick gray lines. Gray thin lines until 500 m is at every 100 m, and thereafter at every 500 m.

phidromic systems where the tide travels around in a clockwise or counterclockwise rotation. The semidurnal amphidromic points and cotidal lines have a similar pattern (Figure 8a,b), both clockwise propagating around an amphidromic point located further west (out of the domain) and one around the southern part of Svalbard. The western amphidromic point may cause the on-shelf M_2 barotropic energy flux at the southern slope with enhanced barotropic energy fluxes ($\langle\overline{\mathbf{F}_0}\rangle$) on the order of $10^5\,\mathrm{W\,m^{-1}}$ across the southern slope crossing the 500 m isobath (Figure 8a, black arrows). The Svalbard amphidromic point brings the propagation towards north through Fram Strait with an off-shelf barotropic energy flux further northwest along the 500 m isobath. Here, the slope is milder due to Storfjorden Trough (Storfjordrenna) and the barotropic energy flux is directed north-west. The baroclinic HKE is weak, on the order of $1\,\mathrm{J\,m^{-2}}$, and mainly occurs where the barotropic energy flux is directed perpendicular to the slope, in the southern and northern region of the western slope. The SBs marked with green stippled lines, covers one region of M_2 baroclinic HKE, on the western slope between $1000-1500$ m isobath. The S_2 constituent is very similar to the M_2 pattern, but with much lesser strength in the barotropic energy flux as these are multiplied by 5 in Figure 8b.

The diurnal constituents have are weaker compared to the semidiurnals, and the tidal phase propagation system is more complex. One amphidromic point located at the central SB with clockwise propagation causes the off-shelf tidal propagation which has been brought up on the shelf by the counterclockwise amphidromic point system close to the south cape of Svalbard. The K_1 barotropic energy flux is directed on-shelf north of Storfjorden Trough and off-shelf south of it, with one order of magnitude less than the M_2 barotropic energy fluxes.

For all constituents, the depth-integrated and time-averaged baroclinic energy flux ($\langle\overline{\mathbf{F}'}\rangle$) is concentrated at the slope below the 1000 m isobath and is nearly 0 on the shelf. The depth-integrated and time-averaged barotropic to baroclinic conversion rate ($\langle\overline{C}\rangle$) is confined between the 500 m and 1500 m isobaths with values in the range of $10^{-3}-10^{-2}\,\mathrm{W\,m^{-2}}$ (Figure 9). This is weak relative to the other subdomains shown in the following sections. The central slope towards Fram Strait shows different patterns of energetics in the south ($74^\circ\,\mathrm{N}-75^\circ\,\mathrm{N}$) and north of 75° N. At the southern slope, the M_2 conversion rate is positive reaching up to a maximum of $0.015\,\mathrm{W\,m^{-2}}$ between the 500 and 1000 m isobaths. The depth-integrated and time-averaged baroclinic energy flux is directed northward along with the shelf between 1000 m and 1500 m depth, with a maximum of $4\,\mathrm{W\,m^{-1}}$. Further north along the slope, the topographic steepness is weaker and the negative conversion rate indicates that the baroclinic tide is losing energy to the barotropic tide, as would occur when perturbed pressure at the bottom is between 90° and 270°

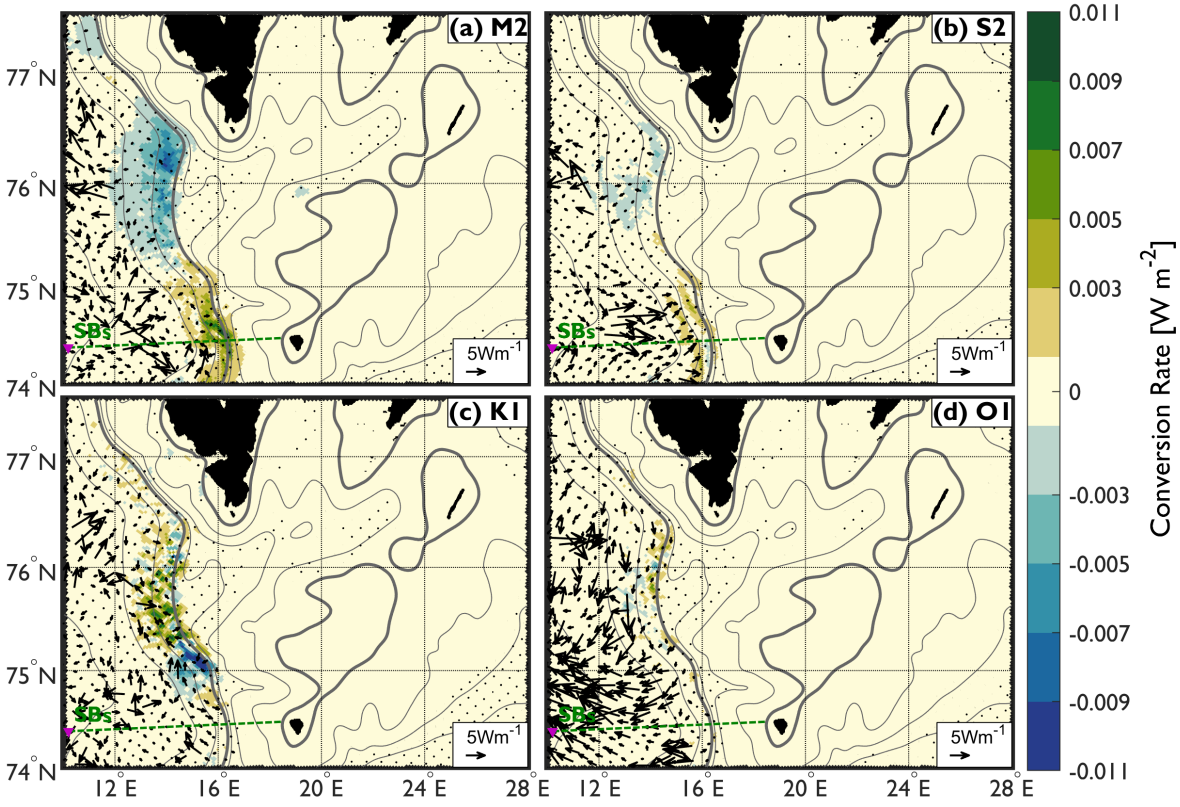

Figure 9: Depth-integrated and time-averaged barotropic to baroclinic energy conversion in colors ($\langle \overline{C} \rangle$) with depth-integrated and time-averaged baroclinic energy flux vectors ($\langle \overline{\mathbf{F}'} \rangle$) following the $5\,\mathrm{W\,m^{-1}}$ reference scale. The maximum conversion rate is $\pm 0.015\,\mathrm{W\,m^{-2}}$. Bathymetry contour spacing as in Figure 8.

out of phase with the barotropic vertical velocity. The internal tide energy that was generated at the southern slope interacts now with the barotropic convergence along the shelf break. The largest negative conversion rate of $0.001\,\mathrm{W\,m^{-2}}$ is found at the same isobaths ($500 - 1500\,\mathrm{m}$) as the largest positive conversion rate. The negative conversion rate region has baroclinic energy fluxes directed towards the deeper ocean, although they are weak $4\,\mathrm{W\,m^{-1}}$ reaching up to $10\,\mathrm{W\,m^{-1}}$ in the deeper regions. The conversion rate pattern for S_2 is similar to M_2, but covers less area and has a maximum of $0.004\,\mathrm{W\,m^{-2}}$, 4 times less than M_2. The S_2 baroclinic energy flux at the southern slope is directed on-shelf instead of along, with approximately $3\,\mathrm{W\,m^{-1}}$ between 1000 m and 1500 m bottom depth decaying to nearly zero at 500 m.

The K_1 constituent has positive and negative conversion rate regions shifted, negative at the southern slope and positive at the northern slope with maximum and minimum of $\pm 0.013\,\mathrm{W\,m^{-2}}$, respectively. The baroclinic energy flux is directed north along the shelf in the negative conver-

sion rate area, whereas the energy flux over the positive conversion rate area is much smaller with no defined direction. The O_1 constituent has a weak conversion rate but larger baroclinic energy flux than M_2, up to a maximum of $25\,\mathrm{W\,m^{-1}}$ towards deeper regions perpendicular to the slope.

Relatively large baroclinic energy dissipation ($\langle\overline{\epsilon'}\rangle$) occurs at the locations of relatively strong conversion rate on the southern slope for M_2 and northwestern slope for K_1 (Figure 10), both on the order of $10^{-2}\,\mathrm{W\,m^{-2}}$. The dissipation pattern echoes the positive conversion rate for M_2 and K_1 and suggests local dissipation after internal tide generation where no baroclinic radiation occurs. The S_2 has a weak dissipation rate of about $0.003\,\mathrm{W\,m^{-2}}$ and is less spatially prevalent than M_2, implying a lack of generation of internal tides propagating and dissipating their energy in the open ocean. In bottom depths below 500 m, K_1 and especially O_1 have an irregular pattern of relatively enhanced dissipation. The diurnal internal tides are trapped at these latitudes, and radiation to greater bottom depths cannot occur.

The along-slope velocity along the SBs, section is shown in Figure 11. The M_2 component

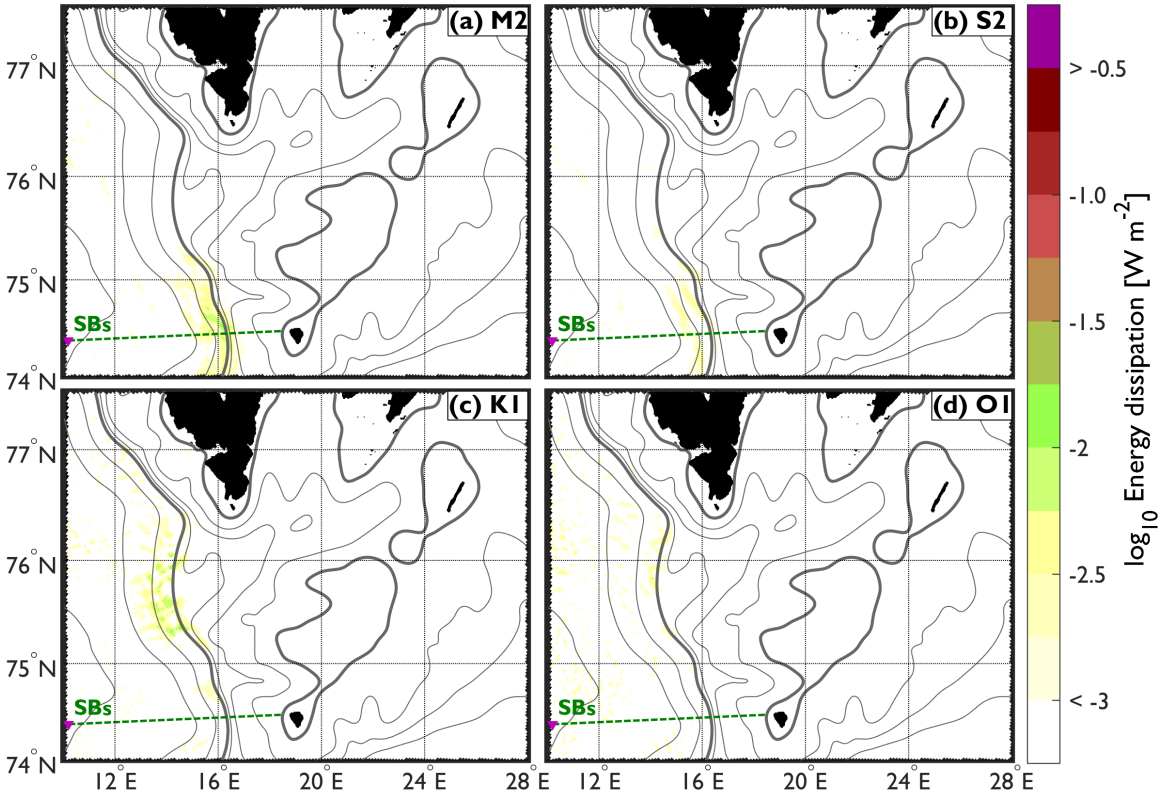

Figure 10: Depth-integrated and time-averaged baroclinic energy dissipation ($\langle\overline{\epsilon'}\rangle$) in subdomain 1. Bathymetry contour spacing as in Figure 8.

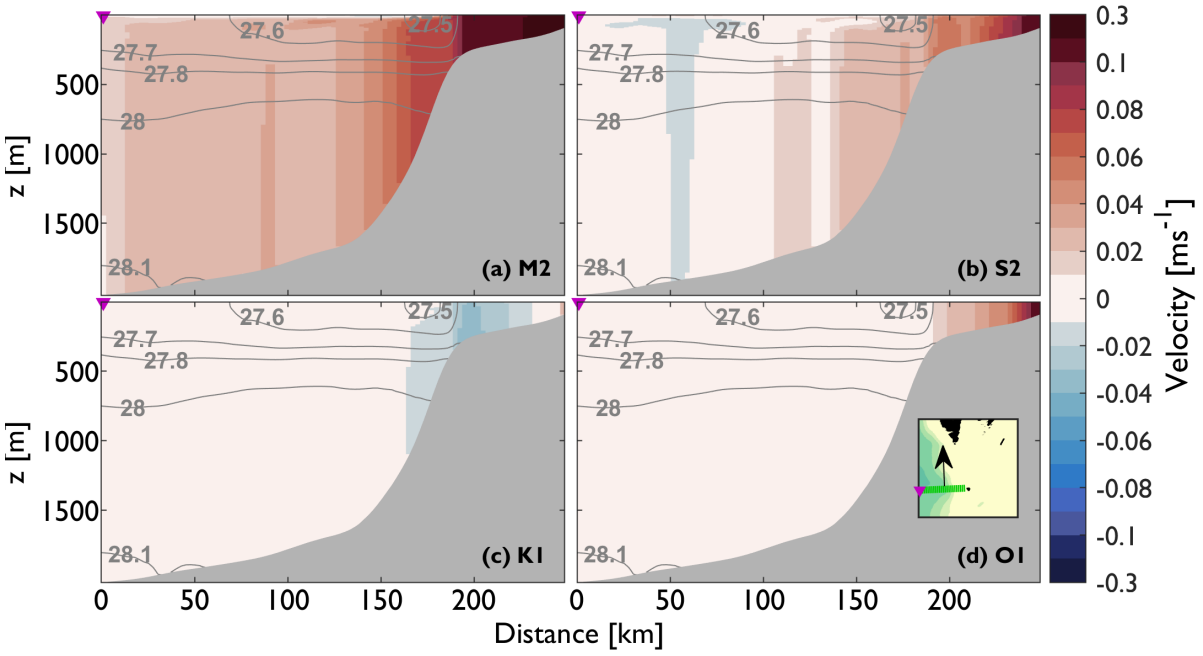

Figure 11: Cross-shelf distribution of the time-averaged along-shelf tidal current ($\langle \mathbf{u}_{along} \rangle$) along the SBs section. At $0.1\,\mathrm{m\,s^{-1}}$ the color-scale changes to intervals of $0.1\,\mathrm{m\,s^{-1}}$. Purple triangle indicates the start of SBs (green line) shown in the elevation map of subdomain 1 in the inset. The black arrow on the map indicates positive direction of the along-shelf tidal current. Potential density anomaly contours (gray lines) are shown at indicated values.

is largest with values up to $0.5\,\mathrm{m\,s^{-1}}$ at the shallowest depth. Throughout the section, all constituents have a nearly constant velocity with depth, especially on the shelf. A small bottom intensification for the S_2 and K_1 components is seen at the shelf break approaching the surface, which could indicate topographic trapped waves. The K_1 has barotropic to baroclinic conversion rate located further north along the slope. A section perpendicular to the slope has been created in that region (not shown) and the along-shelf velocity is similarly bottom intensified, but now with velocity up to $0.08\,\mathrm{m\,s^{-1}}$ at a depth of 500 m, increasing the possibility of trapped internal waves occurring at the slope. Supercritical topography where the slope of the topography exceeds the wave characteristic slope is located between $400 - 1500$ m depth, with the steepness parameter between 1 and 3 for the S_2 constituent. Therefore, a large number of baroclinic modes would be generated from the barotropic forcing. The superposition of these modes would form tidal beams along which baroclinic energy radiates from the bottom (Vlasenko et al., 2012). Above 400 m the S_2 steepness parameter decreases to 0 and becomes imaginary at a distance of 200 km, at the center of Spitsbergen Bank due to well mixed water column (Figure 4). The S_2

velocity amplitudes have the possibility to form beams at this latitude. With weak barotropic energy flux directed along the slope (Figure 8) and weak depth-integrated and time-averaged baroclinic energy flux that radiates on-slope rather than off-slope, no internal tide beams are seen in the along-shelf baroclinic energy flux distribution in the SBs (Figure 12). If the requirement for tidal beam occurrence is satisfied without a change of background stratification or latitude, the tidal wave characteristic lateral distance can be calculated with Eq. (2.29). This would result in approximately 142 km for one round-trip between the bottom and the surface where the beam starts at a distance of 100 km and extends towards deeper ocean. The whole section is above the critical latitude of the M_2 constituent, and no indication is seen of M_2 baroclinic energy flux that radiates perpendicular to the slope nor any velocity structure in forms of beams.

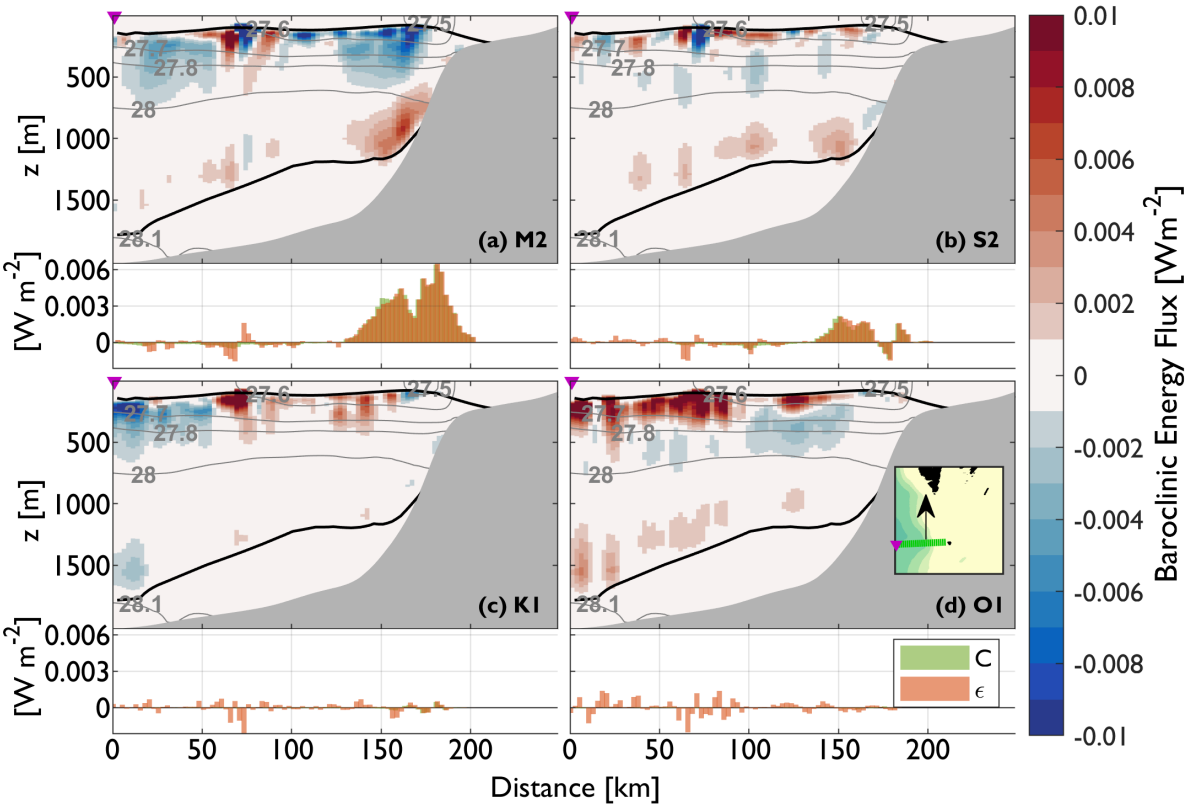

Figure 12: Cross-shelf distribution of the time-averaged along-shelf baroclinic energy flux along the SBs section. Below each section, a graph shows the depth-integrated and time-averaged conversion rate and baroclinic dissipation. Purple triangle indicates the start of SBs (green line) shown in the elevation map of subdomain 1 in the inset. The black arrow on the map indicates the positive direction of the along-shelf baroclinic energy flux. Upper and lower black contours indicate mixed layers where N is less than the tidal frequency ω.

The distribution of time-averaged along-shelf baroclinic energy flux ($\langle \mathbf{F}' \rangle$) along section SBs (Figure 12) confirms the weak tidal forcing. At the slope, the baroclinic energy flux is on the order of $10^{-2}\,\mathrm{W\,m^{-2}}$, less than the Yermak Plateau in subdomain 2. The baroclinic energy flux is positive in direction of shallower depths. Below each section, the depth-integrated and time-averaged barotropic to baroclinic conversion rate and baroclinic dissipation along the section are shown. The M_2 has a weak bottom intensification at the slope between 1000 m and 1500 m depth. With a maximum of $0.009\,\mathrm{W\,m^{-2}}$ close to the bottom, the local baroclinic dissipation almost fully accounts for the conversion rate, indicating that the produced baroclinic energy is dissipated locally.

A total tidal energy budget of each constituent in the SB subdomain is presented in Table 1. The semidiurnal barotropic radiation is large, but the barotropic dissipation is almost 100 %. As a result, the total barotropic to baroclinic conversion rate integrated over the subdomain is actually negative, making the positive conversion rate, baroclinic radiation and dissipation negligible. The diurnal constituents with a different barotropic input produce similarly low magnitude of the energy conversion as the semidiurnals. Negative dissipation is due to larger negative baroclinic radiation than the conversion rate or due to a total negative amount of energy conversion.

Table 1: Tidal energy budget of each subdomain and constituent. The energetic terms (Eqs. $2.30 - 2.31$) are area-integrated over each subdomain with a grid resolution $\Delta A = 2.5\,\mathrm{km}^2$. The percentage of the BT radiation (black), and of the conversion (gray) are indicated.

	Spitsbergen Bank (1)				Yermak Plateau (2)				Nansen Basin Slope (3)			
$\sum(\cdot)\,\Delta A$	M_2	S_2	K_1	O_1	M_2	S_2	K_1	O_1	M_2	S_2	K_1	O_1
BT Radiation $\nabla_H \cdot \langle \overline{\mathbf{F}_0} \rangle$ [GW]	13.32	5.42	1.09	0.20	8.41	0.21	2.51	0.92	3.27	1.02	0.31	0.1
BT dissipation $\overline{\langle \epsilon_0 \rangle}$ [GW]	13.30 100%	5.42 100%	1.08 100%	0.19 99%	8.40 100%	0.20 94%	1.73 69%	0.81 87%	3.20 98%	1.02 100%	0.31 98%	0.1 99%
Conversion $\langle \overline{C} \rangle$ [MW]	-18.8 $< 1\%$	-5.5 $< 1\%$	1.9 $< 1\%$	2.8 1%	11.5 $< 1\%$	12.7 6%	778 31%	118 13%	70 2%	-7 $< 1\%$	6 2%	1 1%
BC Radiation $\nabla_H \cdot \langle \overline{\mathbf{F}'} \rangle$ [MW]	-0.4 2%	-0.6 10%	0.1 4%	0.6 23%	4.4 38%	-3 -24%	-8 -1%	9 8%	6 9%	-4 58%	-1 -17%	0.7 70%
BC dissipation $\langle \overline{\epsilon'} \rangle$ [MW]	-18.4 98%	-4.9 90%	1.8 96%	2.2 77%	7.1 62%	15.7 124%	786 108%	109 92%	64 91%	10 -160%	7.3 116%	0.1 10%

4.3 Yermak Plateau, Subdomain 2

The YP is confined in the subdomain 2 (Figure 2). The semidiurnal surface displacement amplitude (Figure 5a,b) decreases from south of the domain to the northern flank of the YP, where the M_2 amplitude is 3 times larger than the S_2. The K_1 surface displacement amplitude (Figure 5c) separates the western flank of the YP with values exceeding 0.1 m from the eastern flank along the top of the plateau. Overall, the O_1 displacement is negligible. The barotropic velocity is energetic at the southern flank (latitude of 80° N for M_2, K_1 and O_1) and at the northern flank (latitude of 82° 5′ N for K_1 and O_1) with amplitudes between $0.1 - 0.3\,\mathrm{m\,s^{-1}}$ (Figure 5a,c).

The depth-integrated and time-averaged HKE (Figure 6) partly replicates the barotropic velocity amplitude where M_2, K_1 and O_1 are larger at the southern flank and K_1 and O_1 at the northern flank. On the other hand, S_2 with the weakest barotropic velocity amplitude compared to the other tidal constituents, produces the largest HKE at the northern flank with values between 500 and $1000\,\mathrm{W\,m^{-2}}$ (Figure 6b), a factor of 5 larger than the M_2 and K_1 values. The depth-integrated and time-averaged APE (Figure 7) suggests two hotspots at the northern flank with a northwest-band slope and on the southern flank with a southwest-band slope, both between 700 m and 3000 m depth. The diurnal constituents have APE slightly above $10^4\,\mathrm{J\,m^{-2}}$ at these hotspots, whereas the semidiurnals have a maximum close to $3000\,\mathrm{J\,m^{-2}}$.

When the tidal flow interacts with rough bottom topography, baroclinic HKE is enhanced (colored coded in Figure 13). The semidiurnal barotropic HKE energy flux follows the coastline in a way that Svalbard serves as an amphidromic point. The tidal flow meets the southern flank of the YP, resulting in an increased M_2 barotropic HKE in response to its steep slope obstructing a large barotropic velocity and pressure perturbation (arrows in Figure 13). Relatively weaker surface displacement and barotropic velocity amplitude for S_2 result in barotropic HKE energy flux along the topography at the southern flank. On the northern flank, the S_2 barotropic velocity is directed on-shelf, most likely due to an amphidromic point located in the Canadian basin (not shown) that contributes to the on-shelf tidal flow. The barotropic velocity is forced to spread out as the flow is too weak to overcome the top of the plateau, and therefore propagates along the slope in both directions. A relatively large S_2 baroclinic HKE with values up to $600\,\mathrm{J\,m^{-2}}$ is then produced in the region where the barotropic velocity is directed in the opposite direction of the tidal phase propagation. Further west, the barotropic HKE flux is directed off-shelf, aligned with the YP Northern section (YPNs), and the baroclinic HKE weakens.

The K_1 barotropic HKE energy flux is generally trapped in the region (Figure 13c), where at

least three amphidromic points with the bathymetry regulate the corresponding flux direction. On the western flank at bottom depths below 1500 m, the barotropic HKE energy flux (on the order of $10^5\,\mathrm{W\,m^{-1}}$) follows the phase lines of a southwestern amphidromic point (located out of the extent of the region) until meeting the northern flank where two amphidromic points force the flow onto the steep slope on the northern flank. Over the plateau, the barotropic tidal signal is divided into one flow between the shown amphidromic point with a decrease in velocity amplitude in the deeper ocean, and one along the plateau above bottom depths of 1000 m toward

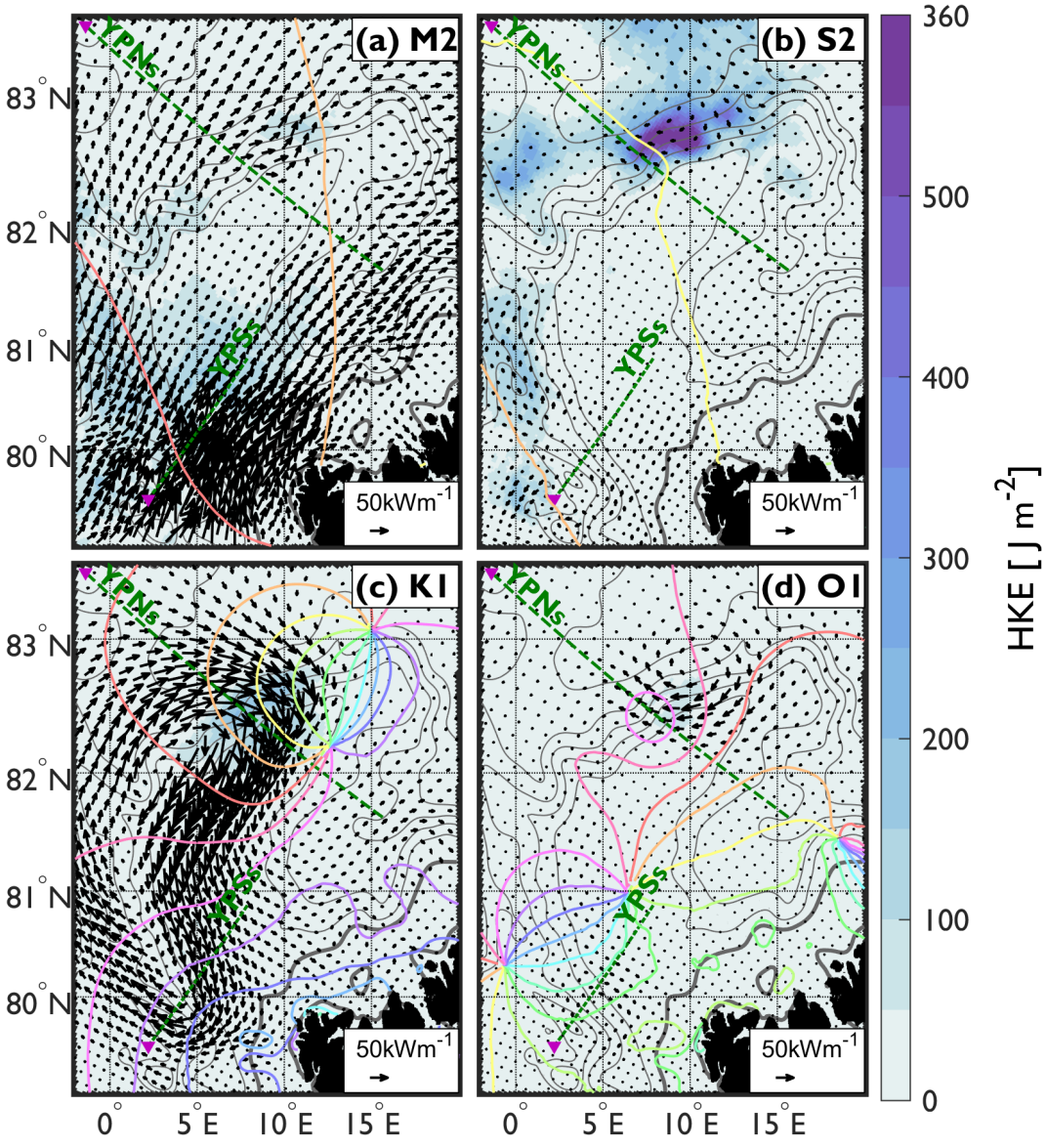

Figure 13: Depth-integrated and time-averaged baroclinic HKE [$\mathrm{J\,m^{-2}}$] ($\langle\overline{E'_{Hk}}\rangle$) colored in background at the Yermak Plateau (subdomain 2). Depth-integrated and time-averaged barotropic energy flux ($\langle\overline{\mathbf{F}_0}\rangle$) is shown with arrows following a reference scale of $50\mathrm{k\,W\,m^{-1}}$. Colored contours are cotidal lines of surface amplitude phases plotted every 30° where the red and orange lines are the 0° and 30° cotidals, respectively. See Figure 5 for bottom contours and subdomains.

the south-western flank where it connects a circulation with the northward propagating tidal flow.

The on-shelf barotropic energy flux of M_2 at the southern flank results in a barotropic to baroclinic energy conversion rate reaching $0.035\,\mathrm{W\,m^{-2}}$ (Figure 14a). The spatial structure of the baroclinic energy flux is highly variable with an overall mean direction directed off-shelf in the conversion region for bottom depths of 1000 m and 2500 m, until meeting a depression below 3000 m where the large baroclinic energy flux is oriented along the isobaths. Similarly, the S_2 energy conversion is relatively weak with a maximum of $0.03\,\mathrm{W\,m^{-2}}$ at the northern flank between 1000 m and 1500 m with baroclinic energy flux vectors directed along-shelf. Despite weak S_2 barotropic forcing, the mean barotropic energy flux vectors are directed normal to the isobaths with a resulting enhanced baroclinic HKE. This is the most favorable direction for efficient conversion. For bottom depths below 2000 m at the northern hotspot, the energy conversion is negative, with a larger baroclinic energy flux directed along the isobaths.

The diurnal constituents show much larger energy conversion rates both at the southern and northern flanks (Figure 14). At the southern flank, a highly variable K_1 energy conversion field is seen with alternating signs along isobaths at all bottom depths of the YP in which baroclinic energy flux is somewhat steered along the isobaths. This can be a region of propagating trapped waves where the negative energy conversion indicates locations of a phase difference between the locally and remotely generated trapped internal waves. Near 81° N along the slope, the baroclinic energy flux is on-shelf but decays substantially toward the top of the plateau.

At the northern flank hotspot, approximately at bottom depths of 2000 m, the energy conversion rate ranges between $0.05 - 0.10\,\mathrm{W\,m^{-2}}$. The K_1 energy conversion values exceed $0.9\,\mathrm{W\,m^{-2}}$ over 2000 m depth, making it the most energetic region. Through the slope, the baroclinic energy flux seems to be divided, one occupying the upper and middle part of the slope between 800 m and 1800 m that is directed off-slope, and another at the lower slope, where the flux veers along the slope with less energetic baroclinic energy flux and conversion. A similar pattern is seen for the O_1 energy conversion and baroclinic energy flux direction (Figure 14d), but with less spatial coverage and weaker magnitudes.

In general, an exponential decrease with distance and a resulting negligible baroclinic energy flux for larger bottom depths than 2500 m away from the slope is seen for all constituents. At the northern flanks, the dissipation rates for the diurnal constituents are exceptional. A depth-integrated and time-averaged dissipation of $0.5\,\mathrm{W\,m^{-2}}$ corresponds to an average dissipation rate per unit mass (typically measured by microstructure profilers) of $5 \times 10^{-7}\,\mathrm{W\,kg^{-1}}$ over 1000 m

depth. This is a highly energetic, turbulent water column. As the baroclinic energy flux is confined within a small distance from the generation site, immediate dissipation or along-shelf propagation are expected (Figure 15). The energy dissipation pattern is nearly identical to the energy conversion pattern for all constituents over the represented subdomain.

Along the YP Southern section (YPSs), at the southern flank of the YP, the M_2 along-shelf tidal currents show a weak surface intensification down to 500 m (Figure 16a) whereas S_2 is negligible. A bottom intensified diurnal tidal current of maximum 0.11 m s^{-1} approaches the surface and is nearly constant with depth (Figure 16c). The tidal current amplitudes compare

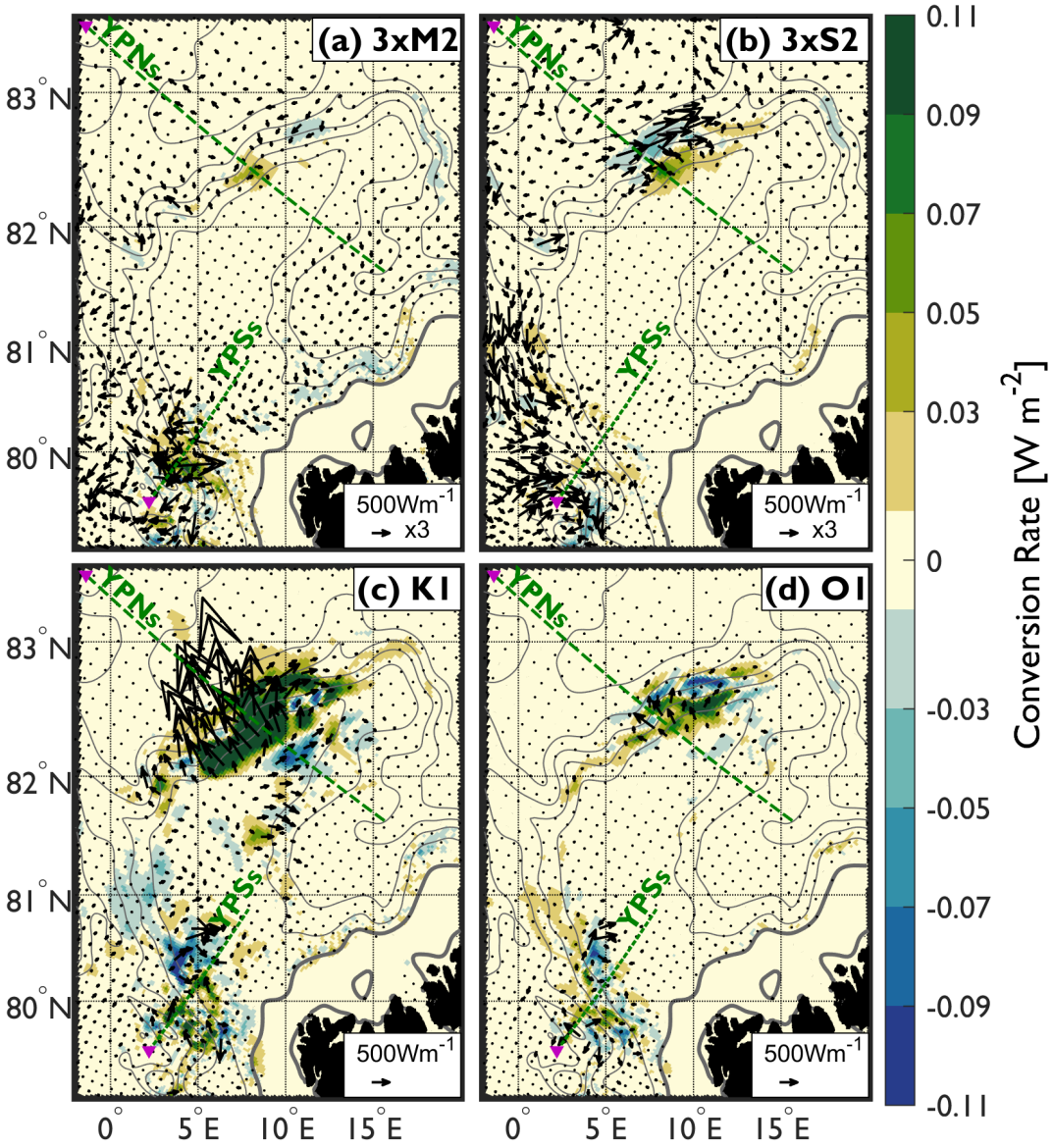

Figure 14: Depth-integrated and time-averaged barotropic to baroclinic energy conversion in colors ($\langle \overline{C} \rangle$) with depth-integrated and time-averaged baroclinic energy flux vectors ($\langle \overline{\mathbf{F}'} \rangle$) following the 500 W m^{-1} reference scale. The semidiurnal values are multiplied with 3. The maximum conversion rate for K_1 is 1.0 W m^{-2}. See Figure 5 for bottom contours and subdomains.

fairly well with the amplitudes found from observational stations with less than $0.14\,\mathrm{m\,s^{-1}}$ in the same region (Fer et al., 2015), except for O_1 which is stronger here. The Arctic Environmental Drifting Buoy (AEDB), that proceeded from the NB along the eastern flank of YP and crossing over to the southern flank, showed that the decay scale of tidal current away from the YP is very short with weak values within 50 km from the bottom of the plateau which corresponds well with the shown diurnal amplitudes. Furthermore, the southern flank slope currents, approximately for bottom depth of 2000 m compare well with the AEDB diurnal currents of $0.15\,\mathrm{m\,s^{-1}}$, which is slightly below the shown values when the tidal currents of K_1 and O_1 are added together (Plueddemann, 1992).

The baroclinic energy flux along section YPSs shows that the energy is contained in the

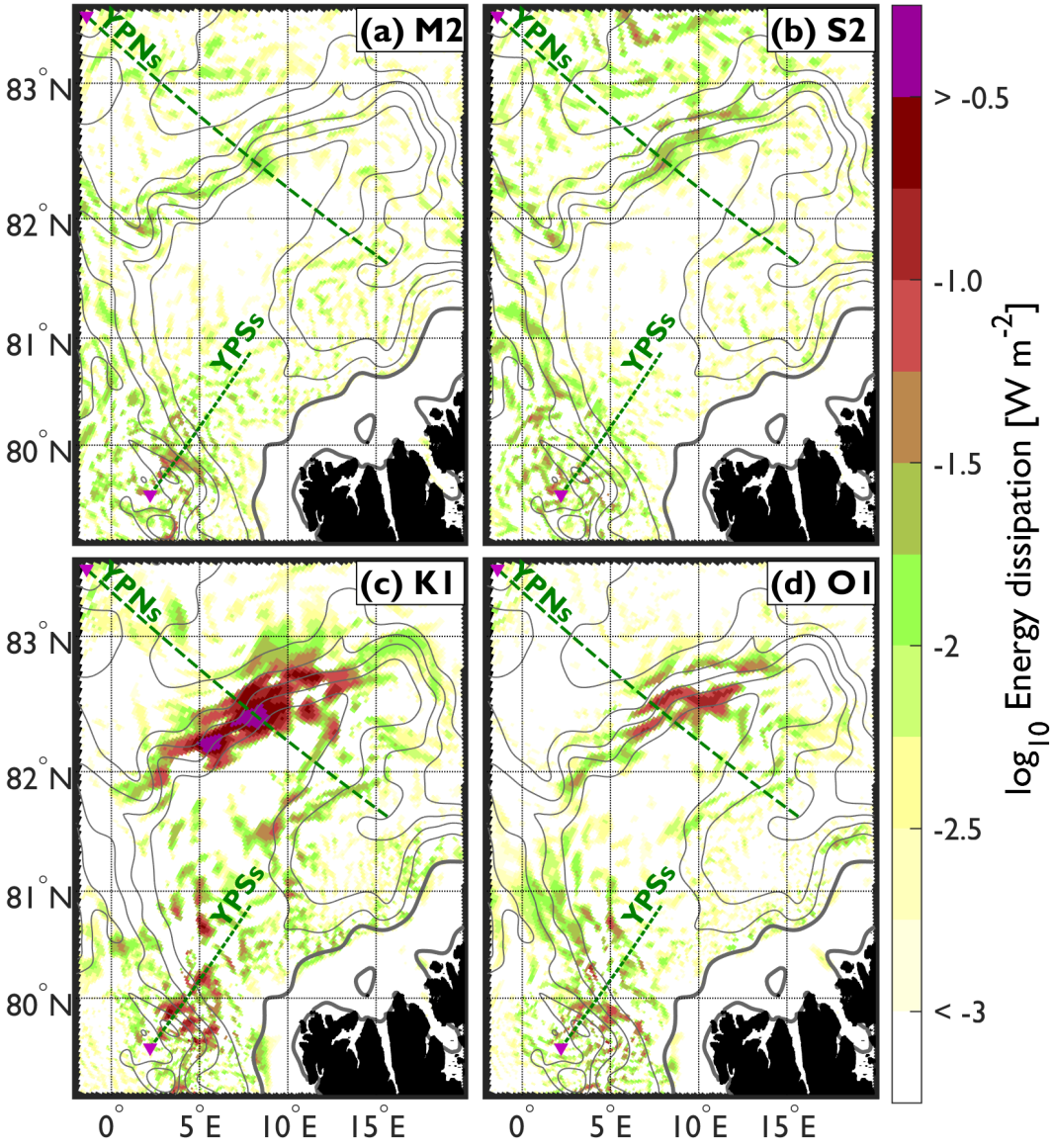

Figure 15: Depth-integrated and time-averaged baroclinic dissipation ($\langle\overline{\epsilon'}\rangle$) in subdomain 2. See Figure 5 for bottom contours and subdomains.

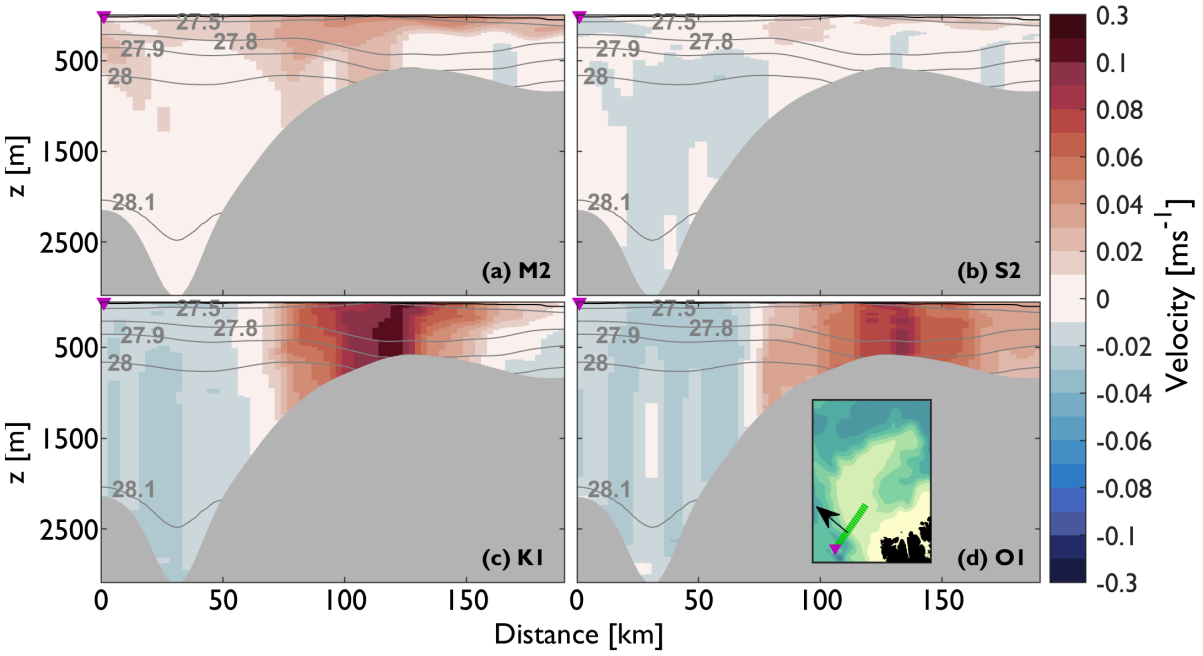

Figure 16: Cross-shelf distribution of the time-averaged along-shelf tidal current ($\langle \mathbf{u}_{along} \rangle$) along the YPSs section. At $0.1\,\mathrm{m\,s^{-1}}$ the color-scale changes to intervals of $0.1\,\mathrm{m\,s^{-1}}$. Purple triangle indicates the start of YPSs (green line) shown in the elevation map of subdomain 2 in the inset. The black arrow on the map indicates the positive direction of the along-shelf tidal current. Potential density anomaly contours (gray lines) are shown at indicated values.

upper and lower layers with several shifts between positive and negative flux directions along the slope (Figure 17c). For larger water depths, K_1 seems to be bottom intensified at a distance of 95 km, with a maximum of $0.3\,\mathrm{W\,m^{-2}}$. The depth-integrated and time-averaged energy conversion dissipates locally at this depth with no baroclinic radiation of internal waves. Where the dissipation is larger than the conversion are regions of negative radiation which indicates a sink of baroclinic energy. For bottom depths of 2800 m, a surface flux intensification is seen down to 700 m that is close to the topographic depression at a distance of 30 km.

At the northern flank of the YP, the cross-shelf tidal current of section YPNs (Figure 18) is typically 2 times larger than the along-shelf current (not shown). In this section, the cross-shelf component of the tidal current is shown since the baroclinic energy flux is directed off-shelf. The M_2 current is relatively strong close to the top of the plateau and is enhanced from the bottom and up to the pycnocline at 200 m. With similar magnitudes, S_2 has a different pattern with a slight resemblance of an internal wave propagating from the surface area at the top of the plateau and intensifies in the interior at 1300 m when meeting a reflected beam in the bottom layer where

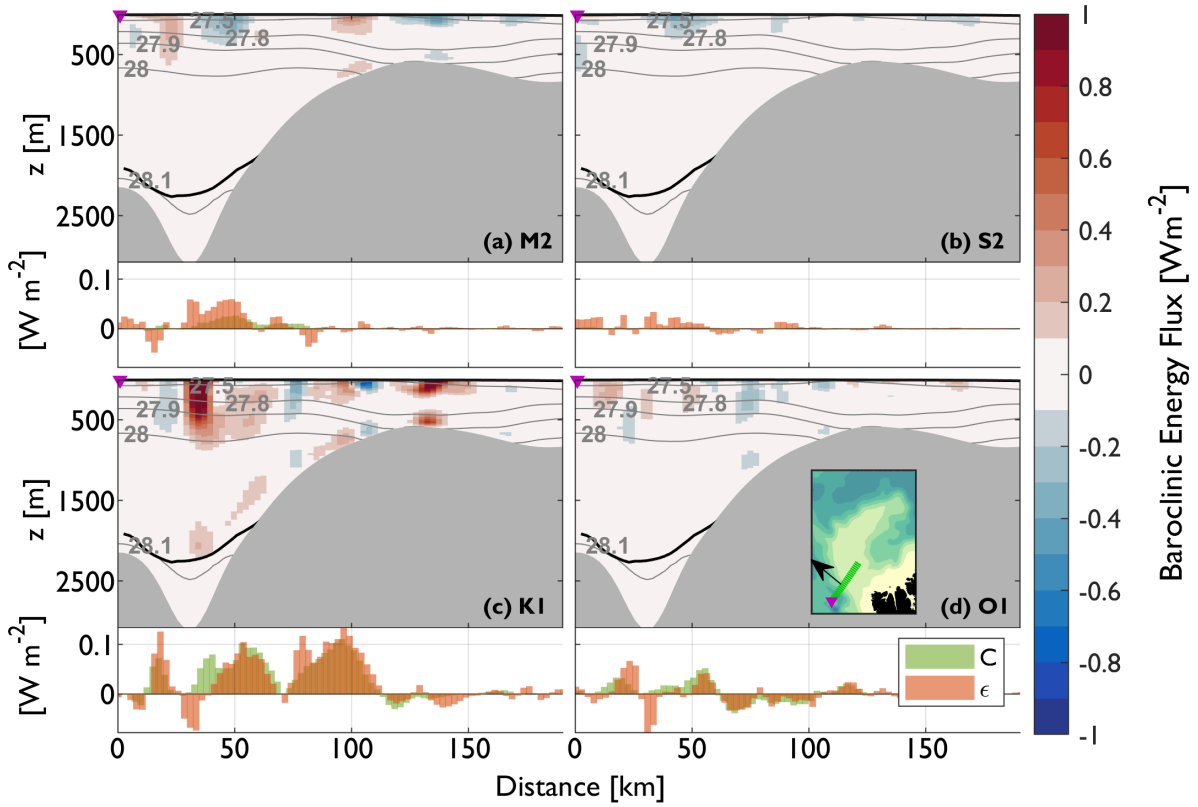

Figure 17: Cross-shelf distribution of the time-averaged along-shelf baroclinic energy flux along the YPSs section. Below each section, a graph shows the depth-integrated and time-averaged conversion rate and baroclinic dissipation. Purple triangle indicates the start of YPSs (green line) shown in the elevation map of subdomain 2 in the inset. The black arrow on the map indicates the positive direction of the along-shelf baroclinic energy flux. Upper and lower black contours indicate mixed layers where N is less than the tidal frequency ω.

$N(x, y, z) \leq \omega$. Thereafter, the reflected beam signal reaches the surface again at 50 km. The maximum value is $0.4\,\mathrm{m\,s^{-1}}$ at top of the plateau for the K_1 constituent (Figure 18c). The O_1 current is directed off-slope, consistent with the outer edge of the counterclockwise barotropic energy flux circulation shown in Figure 13. As in the YPSs, the diurnal current amplitudes are nearly constant with depth and tend to curve towards the top of the plateau.

In the negative energy conversion regions shown for K_1 at the northern flank (distance of $200 - 220$ km, Figure 19c), a sharp change in the phase of density variation ρ_a of approximately 180° takes place at 400 m depth (not shown) with depth-constant phase above and below, which suggests a vertical standing behavior. Inside the high energy conversion region ($100\,\mathrm{km} - 200\,\mathrm{km}$), the phase increases slightly with depth until 200 m, which means that the

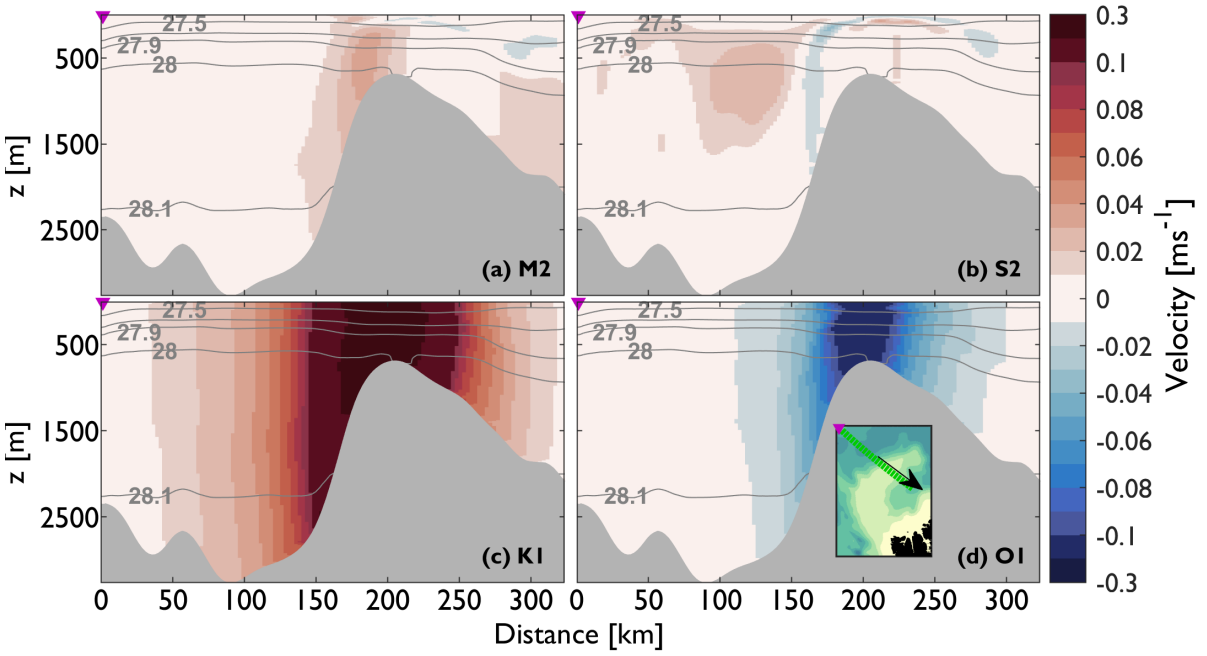

Figure 18: Cross-shelf distribution of the time-averaged cross-shelf tidal current ($\langle \mathbf{u}_{across} \rangle$) along the YPNs section. At 0.1 m s^{-1} the color-scale changes to intervals of 0.1 m s^{-1}. Purple triangle indicates the start of YPNs (green line) shown in the elevation map of subdomain 2 in the inset. The black arrow on the map indicates the positive direction of the cross-shelf tidal current. Potential density anomaly contours (gray lines) are shown at indicated values.

tide is delayed with depth, so the phase velocity is downward with an energy propagation upward. Below 400 m, the density amplitude again slightly increases until reaching 600 m and thereafter nearly constant with depth until the bottom is reached with a total difference of approximately 40° from the top. The current phases have little change with depth with a constant amplitude as it is the case for the CEAREX shown by Plueddemann (1992) where measurements were down to 300 m.

As the S_2 baroclinic energy flux is directed along-shelf (Figure 14b), the S_2 along-shelf baroclinic energy flux in the YPNs (Figure 19b) is emitting from the surface region above the slope and spreads out similarly to the velocity amplitude. For K_1 and O_1, the depth-integrated and time-averaged baroclinic energy flux over the slope is directed in the cross-shelf direction above bottom depths of 1800 m (Figure 14c,d). There are two enhanced flux structures over the slope, one intensified in the upper 500 m layer and one near the bottom. The separation of the structures is dependent on each other and seems to behave in a similar way where baroclinic energy flux is directed in the cross-shelf direction with zero group velocity corresponding to wave energy

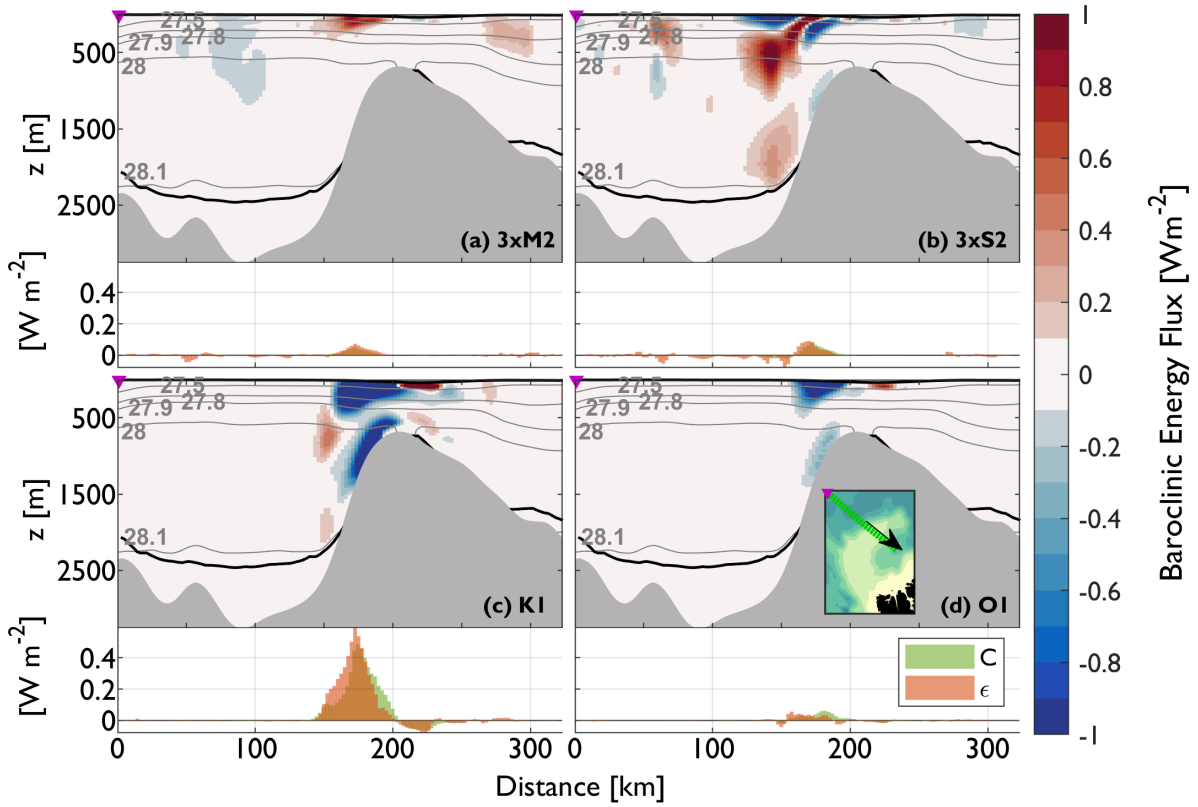

Figure 19: Cross-shelf distribution of the time-averaged cross-shelf baroclinic energy flux in the YPNs section. Below each section, a graph shows the depth-integrated and time-averaged conversion rate and baroclinic dissipation. The M_2 and S_2 values are multiplied with 3. Purple triangle indicates the start of YPNs (green line) shown in the elevation map of subdomain 2 in the inset. The black arrow on the map indicates the positive direction of the cross-shelf baroclinic energy flux. Upper and lower black contours indicate mixed layers where N is less than the tidal frequency ω.

not leaving the site. The maximum value is 11 W m^{-2} where the K_1 and O_1 baroclinic energy flux is confined to the topography and is trapped to the location of conversion at the bottom and in the surface region. The lower slope with bottom depths below 1400 m functions as a sink for the energy converted, whereas in the upper slope more barotropic energy is converted to baroclinic energy than dissipated, indicating a region of radiation. This is also seen for S_2 and O_1 constituents (Figure 19b,d) but with a much smaller magnitude. One would expect that the S_2 baroclinic energy flux is directed outwards as the internal tide is free to propagate, but when the S_2 wave frequency is close to the Coriolis frequency ($f/\omega_{S_2} = 0.996$), the baroclinic energy flux tends to follow the topography, in agreement with the experiment using the Princeton Ocean

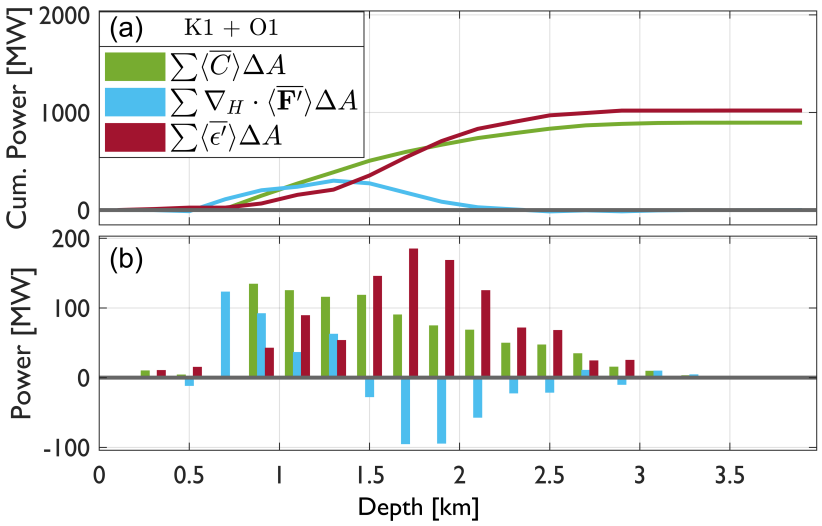

Figure 20: Volume-integrated and time-averaged diurnal energetic terms of Eq. (2.31) binned in isobaths of 200 m in subdomain 2. The shown energetics is the barotropic to baroclinic conversion rate (green), baroclinic radiation (blue) and baroclinic dissipation (red). Panel (a) is the cumulative power and panel (b) is the power per isobath divided into 200 m depth bins, both in MW (10^6 W).

Model and selectively adjusting between near inertial and subinertial frequencies (Smith et al., 2017).

The depth-integrated and time-averaged sum of K_1 and O_1 area-integrated total energetics are shown in Figure 20. Each grid cell of size $\Delta A = 2.5\,\mathrm{km}^2$ is bounded by isobaths with bins of 200 m. Figure 20b shows the energy distribution of the barotropic to baroclinic energy conversion, baroclinic radiation and dissipation within each depth bin, and the upper panel (Figure 20a) shows the corresponding cumulative power. The strongest tidal influenced regime lies between $700 - 2500$ m bottom depth whereas above and below the energetics are weak. Below 900 m, the barotropic to baroclinic conversion has a continuous decrease from a maximum of 130 MW at the 900 m isobath, i.e. most conversion occurs in the upper slope. Likewise, the radiation is strongest for the upper isobaths and becomes negative below 1500 m bottom depth, which acts as a sink for the converted energy in which all converted energy is dissipated. The dissipation is strong below that depth and has its maximum at the bottom depth of 1700 m. At 700 m, radiation is the only significant contributor which means that some of the converted energy can escape from deeper isobaths and radiate toward the shallower part of the YP. The isobath distribution of conversion rate, baroclinic radiation and dissipation is very similar to

that calculated in Fer et al. (2015) (who reported K_1 only from the diurnals). Figure 21 displays the waterfall of energetic consumption of the barotropic tide to energy dissipation through the energetic terms of Eqs. (2.30 and 2.31), similar to the presentation by Kang and Fringer (2012). Of the 3.43 GW total energy from the diurnal barotropic tide, 26 % (∼ 900 MW) is converted to baroclinic tides in which 0.1 % (1 MW) is contributing to radiation and rest to local dissipation. These estimates corresponds well with the conversion rate of 0.94 GW computed from STORMTIDE (see Discussion, Section 5.4) where ∼ 99 % is dissipated of the converted energy (Table 2) at the YP, despite difference in subdomain sizes. The large difference between the barotropic input and how much is converted is because of the subdomain size where the conversion only occurs over limited regions whereas the barotropic input is energetic in regions where no conversion occur. In Table 2, the other presented regions are below the critical latitude, and a much larger amount of the barotropic input is used up for conversion compared to the YP. Also, of the converted energy, a large amount is used to produce the freely propagating internal waves. A total tidal energy budget of each constituent of the YP is presented in Table 1. The YP has the largest barotropic to baroclinic conversion rate in magnitude and percentage of the K_1 barotropic radiation.

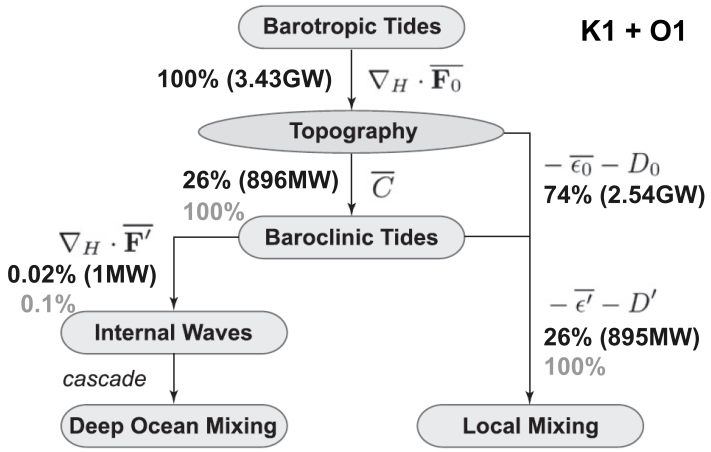

Figure 21: Volume-integrated and time-averaged $K_1 + O_1$ energetic terms of Eqs. (2.30 and 2.31) over subdomain 2. The shown energetics are BT input ($\nabla_H \cdot \overline{\mathbf{F}_0}$), BT to BC energy conversion ($\overline{C}$), BC radiation ($\nabla_H \cdot \overline{\mathbf{F}'}$), BT dissipation ($-\overline{\epsilon_0} - D_0$) and BC dissipation $\overline{\epsilon'} - D'$. Units are in GW ($10^9$ W) and MW (10^6 W).

Table 2: Total BT tidal energy input, BT to BC energy conversion rate, radiation and dissipation in units of 10^9 W [GW], for studies in different regions. The % given in black denotes the energy lost from the BT tide, whereas the one in gray denotes the energy used from the BT to BC energy conversion.

	Constituents analyzed	Barotropic Input	BT Dissipation	Conversion	Radiation	BC Dissipation
Monterey Bay Area[a]	M_2	0.15	0.02 $\sim 12\,\%$	0.13 $\sim 88\,\%$	0.06 $\sim 42\,\%$	0.77 $\sim 58\,\%$
Hawaiian Islands[b]	M_2	2.70	0.16 $\sim 6\,\%$	2.30 $\sim 85\,\%$	1.70 $\sim 74\,\%$	0.45 $\sim 20\,\%$
Luzon Strait[c]	M_2, S_2, K_1, O_1	-	-	24.07	14.57 $\sim 61\,\%$	9.50 $\sim 39\,\%$
Andaman Sea[d] (Three subdomains)	M_2, S_2	17.49	3.09 $\sim 18\,\%$	14.37 $\sim 82\,\%$	4.20 $\sim 29\,\%$	9.82 $\sim 68\,\%$
Yermak Plateau[e]	M_2, K_1	-	-	0.94	0.01 $\sim 1\,\%$	0.93 $\sim 99\,\%$

[a]Kang and Fringer (2012), [b]Carter et al. (2008), [c]Alford et al. (2011), [d]Mohanty et al. (2018), and [e]Fer et al. (2015).

4.4 Nansen Basin Slope, Subdomain 3

In subdomain 3, the Nansen Basin Slope (NBS) has typical surface displacement amplitudes of $0.1 - 0.2\,\mathrm{m}$ with barotropic tidal velocity amplitudes ranging from a maximum of $0.5\,\mathrm{m\,s^{-1}}$ close to the 500 m isobath to $0.01\,\mathrm{m\,s^{-1}}$ for bottom depth of 2000 m where the semidiurnals are more prevalent (Figure 5). The diurnals are relatively less energetic compared to the semidiurnals

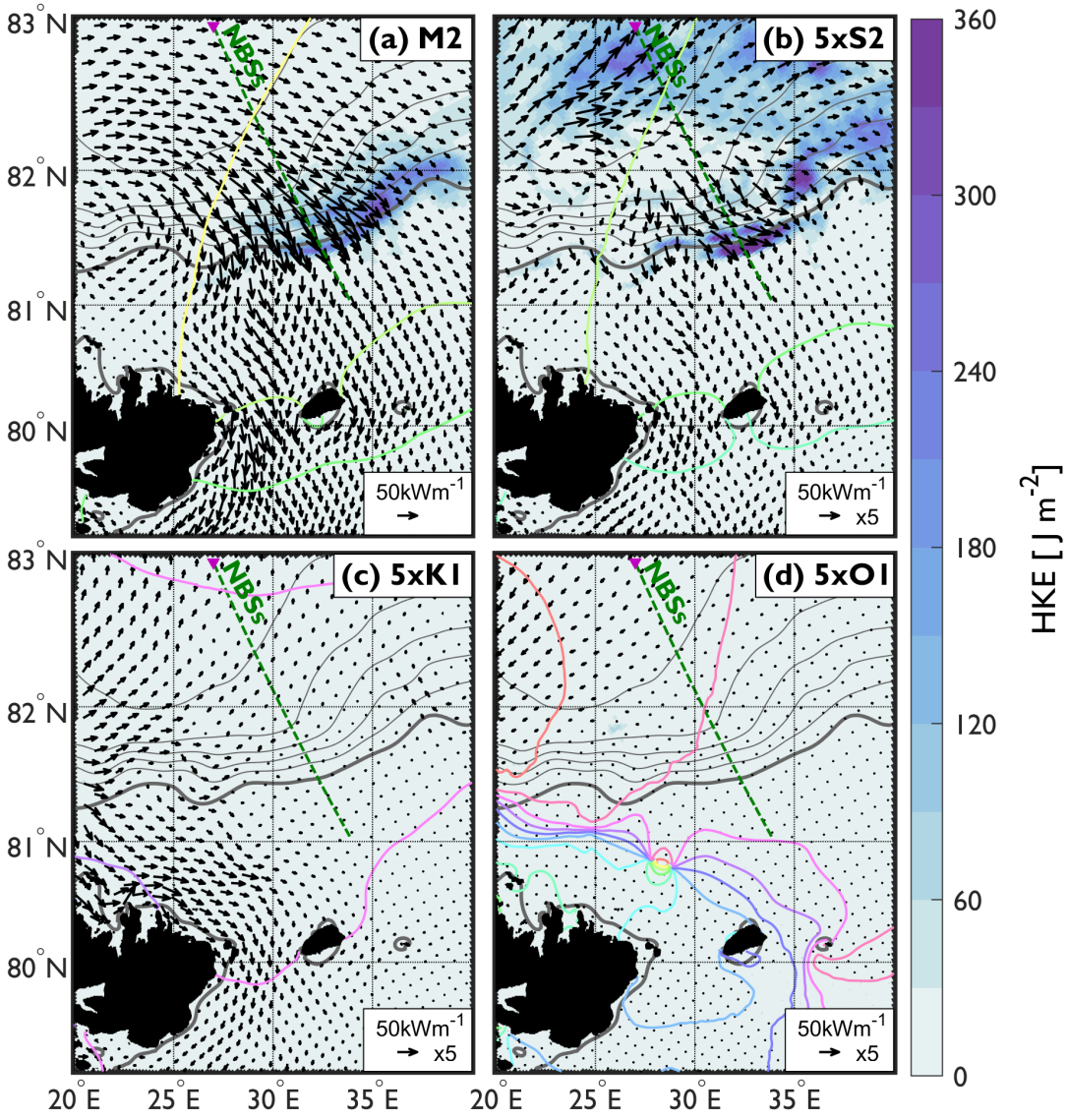

Figure 22: Depth-integrated and time-averaged baroclinic HKE $[\mathrm{J\,m^{-2}}]$ ($\langle\overline{E'_{Hk}}\rangle$) on the continental slope north of Svalbard (subdomain 3). Maximum value is $320\,\mathrm{J\,m^{-2}}$ at the slope in (a). Depth-integrated and time-averaged horizontal barotropic energy flux ($\langle\overline{\mathbf{F}_0}\rangle$) is shown with arrows with a reference scale of $50\,\mathrm{kW\,m^{-1}}$. The S_2, K_1 and O_1 values are multiplied with 5. See Figure 5 for bottom contours and subdomains.

in this subdomain. The depth-integrated and time-averaged baroclinic HKE (Figure 6) for M_2 is particularly enhanced around 81°5′ N and 33° E, where the bottom contours change their orientation from mainly west-east to towards north. In this region, the baroclinic HKE is comparable with the depth-integrated and time-averaged APE on the order of $10^2\,\mathrm{J\,m^{-2}}$ at bottom depth between 500 m and 2500 m (Figure 7) for both semidiurnal constituents.

A close-up in subdomain 3 (Figure 22) in this energetic region, shows that the barotropic

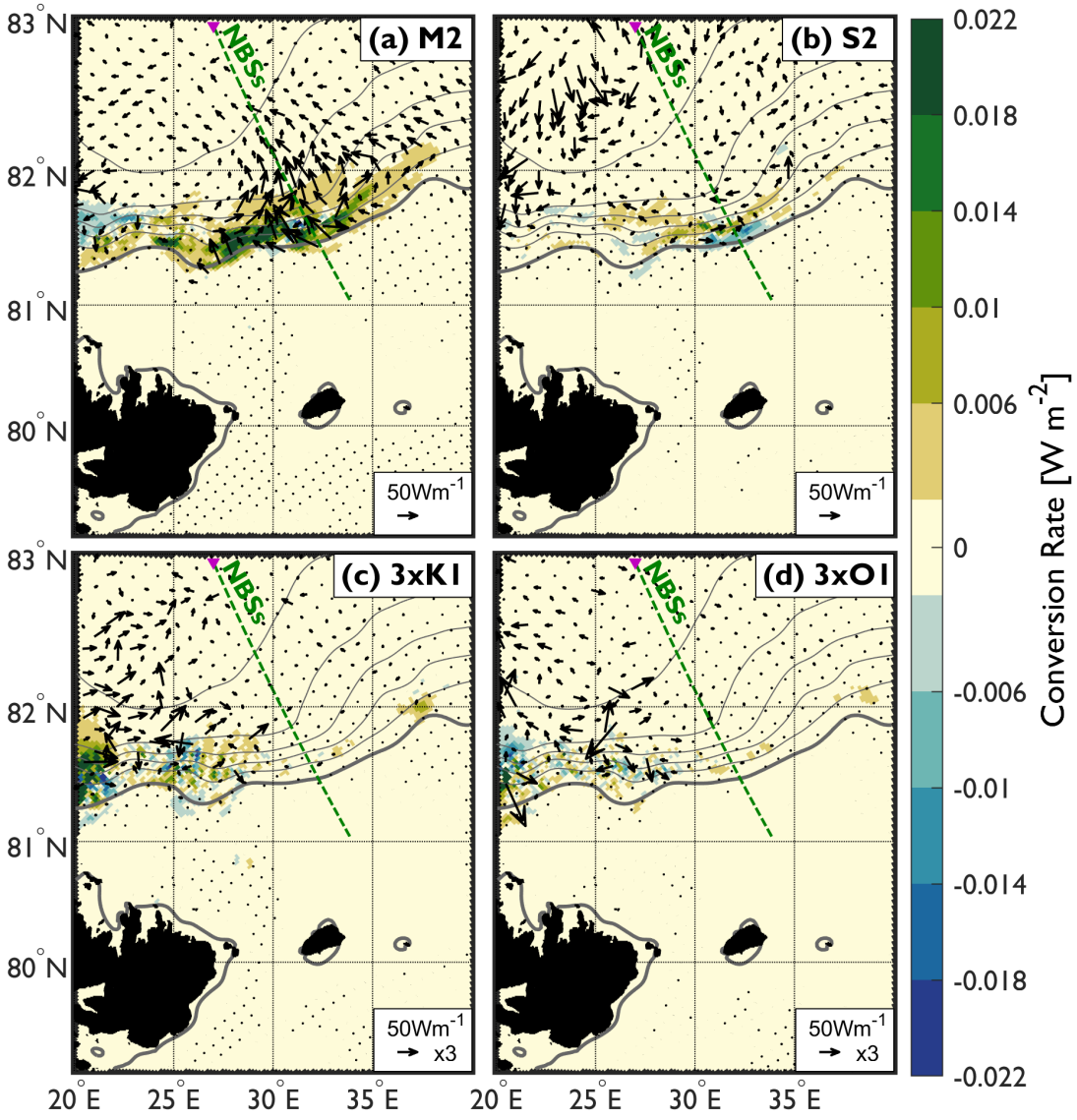

Figure 23: Depth-integrated and time-averaged barotropic to baroclinic energy conversion in colors ($\langle\overline{C}\rangle$) with depth-integrated and time-averaged baroclinic energy flux vectors ($\langle\overline{\mathbf{F}'}\rangle$) following the $50\,\mathrm{W\,m^{-1}}$ reference scale. The diurnal values are multiplied with 3. A maximum conversion rate of $\pm 0.04\,\mathrm{W\,m^{-2}}$ is reached for M_2. See Figure 5 for bottom contours and subdomains.

energy flux vectors are directed on-shelf for M_2 and S_2 with a maximum of 110 kW m^{-1} occurring at the 500 m isobath (Figure 22a). On the other hand, S_2 has weaker barotropic energy flux and change of direction to a comparable along-shelf component when reaching the 500 m isobath from deeper bottom depths. The diurnal barotropic energy flux and the baroclinic HKE are much weaker than the semidiurnals as expected from Figure 5.

The depth-integrated and time-averaged conversion rate for M_2 has a maximum value of 0.04 W m^{-2} at the slope region (Figure 23a). With a mean on-shelf barotropic energy flux in

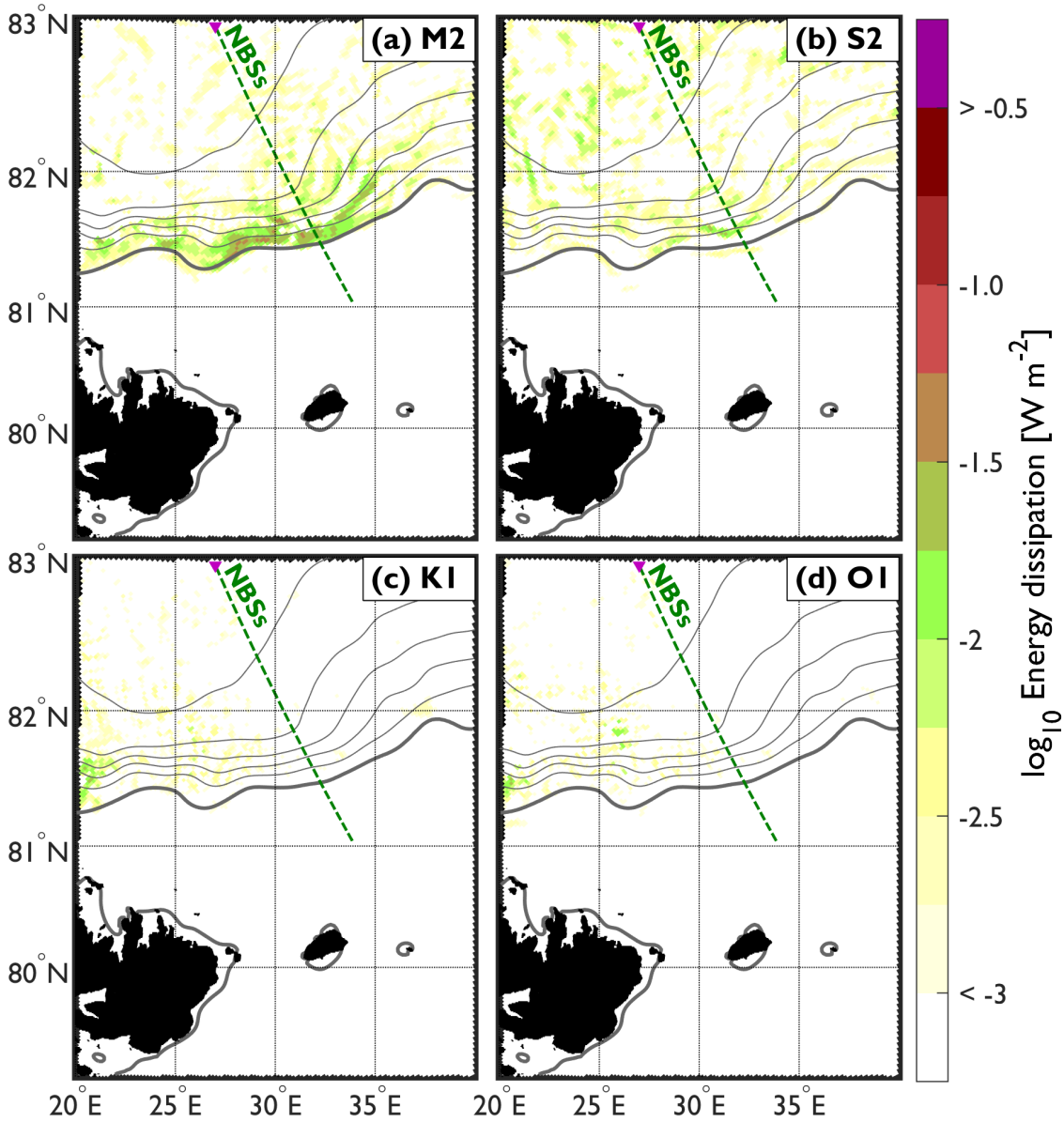

Figure 24: Depth-integrated and time-averaged baroclinic dissipation ($\langle\overline{\epsilon'}\rangle$) in subdomain 2. See Figure 5 for bottom contours and subdomains.

Figure 22a, an off-shelf baroclinic energy flux is seen above 500 m and below 1800 m bottom depths, where the bottom contours are further apart. In between these depths, with comparable magnitude, the baroclinic energy flux vectors have a slightly larger component along instead of across the slope, especially where the barotropic to baroclinic conversion lies. For S_2, a weaker resemblance is seen.

The depth-integrated and time-averaged energy dissipation (Figure 24) follows the pattern of barotropic to baroclinic conversion at the steepest part of the slope. The M_2 energy dissipation has a maximum of $0.05\,\mathrm{W\,m^{-2}}$ and accounts for the barotropic to baroclinic conversion at most depths. Further, as in the other subdomains, there are patches of energy dissipation on the order of $10^{-2}\,\mathrm{W\,m^{-2}}$ on the lower slope with bottom depth below 2500 m. Because of the trapping above critical latitudes, these values do not occur due to radiation of barotropic to baroclinic conversion. The patches of energy dissipation occurrence are also more prevalent for the S_2 constituent as it is free to propagate at the latitude, but the distribution and magnitude of barotropic to baroclinic conversion rates do not suggest the NBS as a generation site for S_2 internal tides.

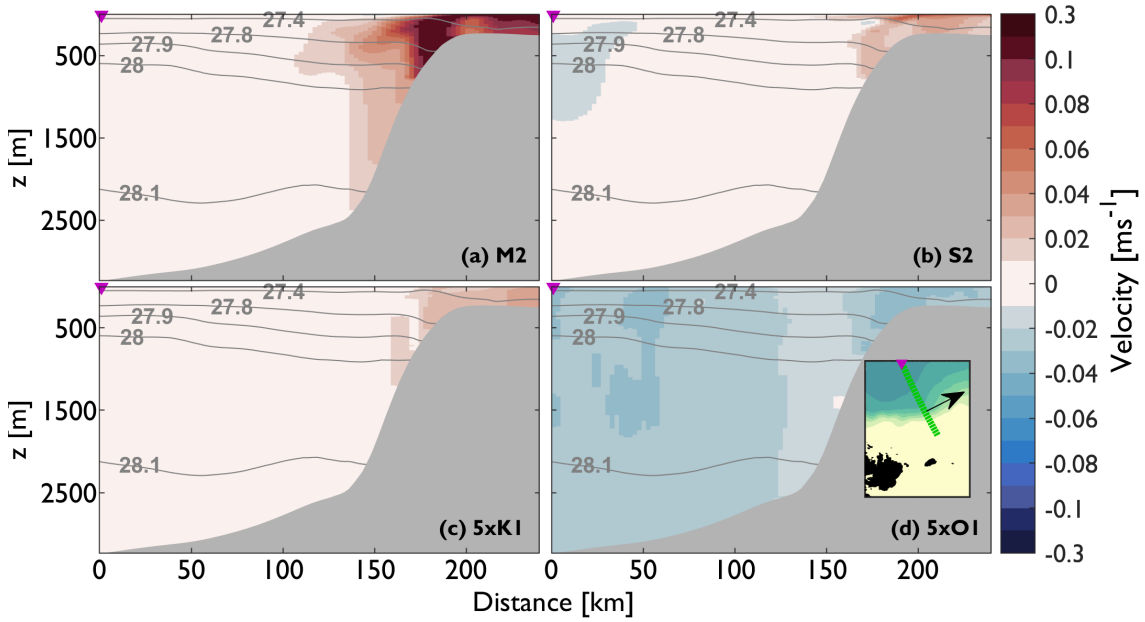

Figure 25: Cross-shelf distribution of the time-averaged along-shelf velocity along the NBSs section. At $0.1\,\mathrm{m\,s^{-1}}$ the color-scale changes to intervals of $0.1\,\mathrm{m\,s^{-1}}$. Purple triangle indicates the start of NBSs (green line) shown in the elevation map of subdomain 3 in the inset. The black arrow on the map indicates positive direction of the along-shelf velocity current. Potential density anomaly contours (gray lines) are shown at indicated values.

A representative section across the slope, NBSs (Figure 22) is extracted. Figure 25 shows the along-shelf tidal velocity along NBSs. Along the section, M_2 tidal current is intensified over the slope with an existing near surface intensification of $0.2\,\mathrm{m\,s^{-1}}$ that seems to begin from the pycnocline at approximately 50 m depth over top of the shelf. In this region, the density phase increases both upwards and downwards from the pycnocline. The surface intensification seems to influence the interior for deeper ocean. The structure stretches out in the cross-shelf direction and decays over approximately 130 km from the slope to $0.01\,\mathrm{m\,s^{-1}}$ at 800 m depth. Another structure is produced at the bottom close to the top of the slope, which seems to exist independently from the surface intensification. It has its maximum close to the bottom and decreases in the cross-shelf direction and vertical but seems to coincide with the near surface intensification. The potential density contours are farther apart from each other indicating a more mixed water column with a shallower pycnocline at 20 m depth. The S_2 has a similar pattern but with a weaker velocity and smaller horizontal and vertical extent. The maximum is at the surface at the same spot as M_2 and protrudes into the abyss.

For domain 3, the Froude number is close to zero which means linear internal tides can be generated. The topography is supercritical with values of the topographic slope much larger than the slope of the characteristics ($\alpha > 10$) at the conversion region, and therefore, higher modes would be generated where the superposition creates tidal beams. No S_2 radiated internal tides is observed in the velocity radiating along or across the slope, which is most likely due to the weak barotropic forcing seen in Figure 22b. If there are large velocities, we would expect high velocity shears and increased mixing.

Figure 26 shows high semidiurnal along-shelf baroclinic energy flux at mainly two locations, the bottom and the surface hotspots of the slope. The M_2 surface intensification of baroclinic energy flux extends over a 100 km distance with a change of direction at 500 m depth. For two places at the slope, the surface intensification reaches 250 m, separated by an approximately 25 km cross-shelf distance. The baroclinic energy flux has a maximum of $0.2\,\mathrm{W\,m^{-2}}$ comparable with sites below critical latitude where the internal wave activity is weak (Holloway and Merrifield, 1999). The enhanced near surface intensification can be due to strong along-shelf current and stratification effects. The mixed layer depth is much larger in the shallow regions which may be the reason for the extent of the surface intensification on the shelf, whereas for deeper ocean than the slope's extent, the currents are generally weak (not shown).

The M_2 depth-integrated and time-averaged barotropic to baroclinic energy conversion is fully used up for dissipation along the section except for the surface intensification at a dis-

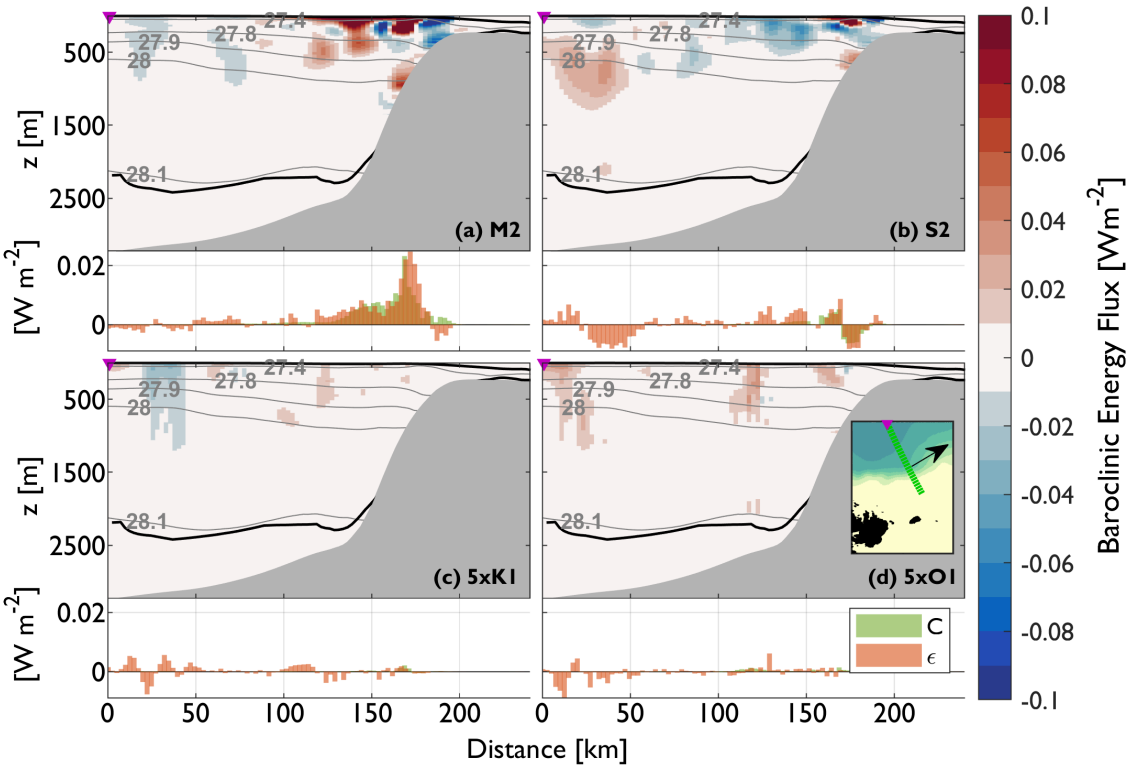

Figure 26: Cross-shelf distribution of the time-averaged along-shelf baroclinic energy flux in the the NBSs section. Below each section, a graph shows the depth-integrated and time-averaged conversion rate and baroclinic dissipation. Purple triangle indicates the start of NBSs (green line) shown in the elevation map of subdomain 3 in the inset. The black arrow on the map indicates positive direction of the along-shelf baroclinic energy flux. Upper and lower black contours indicate mixed layers where N is less than the tidal frequency ω.

tance of 140 km. The depth-integrated and time-averaged sum of M_2 area-integrated per depth interval energetics are shown in Figure 27. The strongest tidal-influenced regime lies between $500-1500$ m depth, whereas above and below the energetics are weakly forced. Below 700 m and down, the barotropic to baroclinic conversion decreases continuously from a maximum of 15 MW at the 700 m isobath. The radiation is strong at the 300 m isobath and, as in the YP subdomain, is the only place where propagation occurs without any dissipation. The dissipation is stronger than the conversion around 700 m with negative radiation, and is therefore a sink for baroclinic radiation. For greater bottom depths, the dissipation follows the conversion as the cumulative power indicates. Figure 28 displays the cascade of energetic consumption of the M_2 barotropic tide to energy dissipation over subdomain 3. Of the $\sim$3.27 GW total energy from the M_2 barotropic tide, 2% (70 MW) is converted to baroclinic tides in which 9 % (6 MW) is

contributing to radiation and rest (64 MW) to local dissipation.

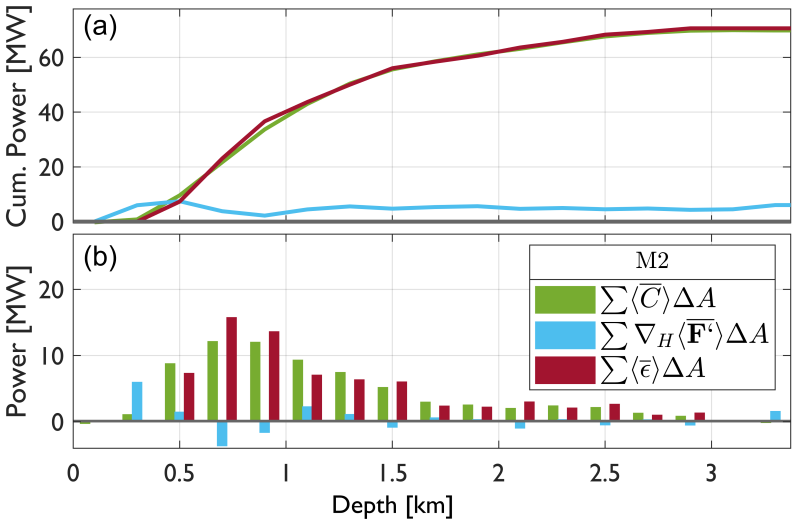

Figure 27: Volume-integrated and time-averaged M_2 energetic terms of Eq. (2.31) binned in isobaths of 200 m in subdomain 3. The shown energetics is the barotropic to baroclinic conversion rate (green), baroclinic radiation (blue) and baroclinic dissipation (red). Panel (a) is the cumulative power and panel (b) is the power per isobath divided into 200 m depth bins, both in MW (10^6 W).

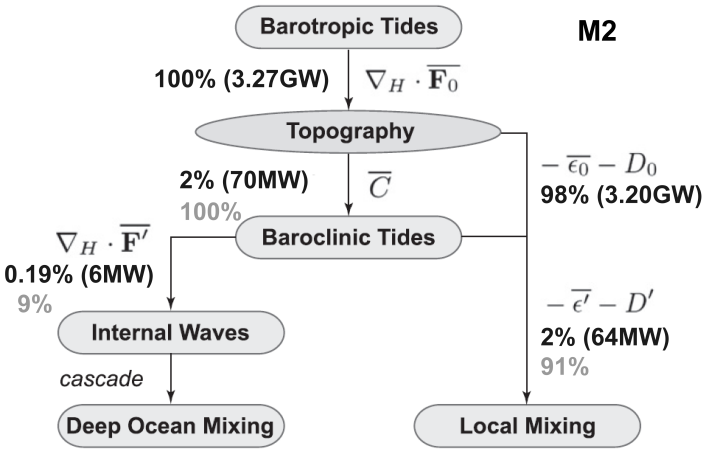

Figure 28: Volume-integrated and time-averaged M_2 energetic terms of Eqs. (2.30 and 2.31) over subdomain 3. The shown energetics are the BT radiation ($\nabla_H \cdot \overline{\mathbf{F}_0}$), BT to BC energy conversion ($\overline{C}$), BC radiation ($\nabla_H \cdot \overline{\mathbf{F}'}$), BT dissipation ($-\overline{\epsilon_0} - D_0$) and BC dissipation $\overline{\epsilon'} - D'$. Units are in GW ($10^9$ W) and MW (10^6 W).

5 Discussion

5.1 Validity and limitations of the model

The APE values obtained from the ROMS analysis compare reasonably well with the global calculations by Falahat and Nycander (2015) and case studies over idealized topography by Holloway and Merrifield (1999), except in some regions with weak stratification in the shallow and deep ocean. High APE is found over the central SB (not shown) reaching nonphysical values, of up to $10^6\,\mathrm{J\,m^{-2}}$, where M_2 and K_1 are more prevalent. The nonphysical APE occurs because of the weak stratification ($N^2 \to 0$) in the mixed layers where $1/N^2$ becomes singular. At the western slope of SB, at bottom depths deeper than 500 m, large K_1 APE (a maximum of $10^3\,\mathrm{J\,m^{-2}}$, Figure 7c) is one order of magnitude less than the magnitude of the first two baroclinic modes of K_1 and O_1 presented by Falahat and Nycander (2015). Falahat and Nycander (2015) calculated the first 10 baroclinic modes of the M_2 total energy density below 500 m bottom depth at the western slope to be on the order of $100 - 300\,\mathrm{J\,m^{-2}}$, which has the same order of magnitude with the APE shown in Figure 7a. This available portion of the potential energy that can be converted to internal wave energy is not in the same magnitude as the baroclinic HKE that would be expected from the results of Holloway and Merrifield (1999). At the NBS, just below the 500 m isobath, Falahat and Nycander (2015) found M_2 total energy density to be around 300 to $1000\,\mathrm{J\,m^{-2}}$ which do correspond well with the sum of the shown APE and HKE (Figure 6a and 7a).

At the SB above the 200 m isobath, Rippeth et al. (2017) estimated barotropic to baroclinic conversion rate with values as high as $0.25\,\mathrm{W\,m^{-2}}$ in early August stratification. This was achieved with the high resolution nonlinear nonhydrostatic MITgcm model and an observed stratification that is distinct from the present study. The conversion rate at bottom depths shallower than 200 m (Figure 9) is nearly $0\,\mathrm{W\,m^{-2}}$, which is negligible compared to the estimates from MITgcm. Parts of the disparity in conversion can be explained by the depth-averaged buoyancy frequency of Rippeth et al. (2017) ($N \sim 5.5\,\mathrm{x}\,10^{-3}\,\mathrm{s^{-1}} = 3.15\,\mathrm{cph}$) which is considerably larger than the area- and depth-averaged buoyancy frequency found here at the central bank ($N \sim 3.2\,\mathrm{x}\,10^{-4}\,\mathrm{s^{-1}} = 0.18\,\mathrm{cph}$). The calculated MITgcm dissipation at approximately 100 m isobath, averaged in the thermocline, has a mean value of $4.5\,\mathrm{x}\,10^{-5}\,\mathrm{W\,m^{-3}}$ accounting for 37 % of the observed dissipation below the surface mixed layer. With a surface mixed layer of approximately 18 m shown in Figure 4 of Rippeth et al. (2017) an equivalent depth-integrated and time-averaged dissipation rate is $\sim 10^{-2}\,\mathrm{W\,m^{-2}}$. The baroclinic dissipation in Figure 10 at

the 100 m isobath is one order of magnitude less, where values are below $10^{-3}\,\mathrm{W\,m^{-2}}$. Baroclinic dissipation is taken as the difference between baroclinic radiation and conversion rate, and for inaccurate velocity amplitudes, this simplified balance could produce considerable baroclinic energy flux divergence and an irregular dissipation pattern is produced. Overall, the steady-state, simplified balance used in this study in the conversion, radiation and dissipation calculations is a limitation of the approach, but is consistent with other studies in the literature.

If the buoyancy frequency N becomes so small that it approaches f, no possibility exists for transferring motion between sub- and super-inertial regions following Eq. 2.29. This predicts that a freely propagating linear internal wave would reflect at the interface separating homogeneous and stratified waters. Low buoyancy frequency occurs mostly in shallow regions over the SB, the Barents Sea and in the deep ocean bottom mixed layer. Above the 100 m isobath of SB, the buoyancy frequency approaches the M_2 tidal frequency $\omega_{M_2} = 2.2\,\mathrm{x}\,10^{-5}\,\mathrm{s^{-1}}$, which is lower than the local inertial frequency, in the lower layer that would make the horizontal component of the Earth's rotation important. Here, in the upper mixed layer, even smaller buoyancy frequencies occur which would make the non-traditional terms of the momentum equation significant and the frequency boundaries of freely internal wave propagation must be adjusted.

5.2 Effect of trapped waves

The pathway of wave energy of the astronomical forced tides to scattering into high frequency and nonlinear waves followed by dissipation and mixing is typically based on the conditions of freely propagating internal tides (Kang and Fringer, 2012). The traditional calculations of the energy conversion between barotropic and baroclinic modes over rough topography in presence of subinertial trapped internal waves leads to incorrect estimates as the barotropic mode has a depth-variable vertical structure which cannot be separated from the baroclinic mode (Musgrave, 2019). When trapped waves are formed, a set of modal structures is created where the gravest mode has small baroclinic components and the higher modes have large depth means, meaning that the gravest 'barotropic' mode cannot be isolated by simply taking the depth mean. Therefore, the astronomical forcing can force the baroclinic modes directly without going through the gravest mode. The formulations outlined in Section $2.2 - 2.3$, and see also Kang and Fringer (2012), are applied by many authors to calculate the energy budget and fluxes of subinternal trapped waves. These results may lead to incorrect estimates of energy transitions directed toward and between modal structures, and must be interpreted with caution. When the current and pressure are decomposed, the gravest mode is assumed to fully account for the

depth mean. The barotropic to baroclinic conversion rate and baroclinic energy flux are then underestimated since the depth mean component of the baroclinic mode has been removed and incorrectly added into the gravest mode. This error in the estimate of barotropic and baroclinic energy remains unquantified and can be significant where trapped internal waves are dominant.

While the estimate of astronomical forcing is incorrectly added to the different modes, also the wave modes do not in general form an orthogonal basis, which means that the total wave energy is not the sum of individual modes (Huthnance, 1978). This is particularly problematic over sloping bottoms (as the orthogonal modes are typically solved for flat bottom). For internal wave modes to be separated, the orthogonality relation (Eq. 2.28) needs the Kronecker-delta δ_{nm} to be zero for all existence of mode $n \neq m$, whereas when $n = m$, the $\delta_{nm} = 1$. This is not true for short trapped internal waves present in shallow seas as the magnitude for the cross product Γ_n is non-zero (Musgrave, 2019). By numerically solving the internal wave Eq. (2.25), Musgrave (2019) found that the underestimated depth-offshore integrated baroclinic energy flux accounted for around $10-40\,\%$ of the total wave flux for the first three modes. These errors likely account for a large part of the nontrivial baroclinic energy flux patterns seen in each subdomain (Figures 9, 14 and 23).

5.3 Barotropic structure of the tidal current

Brink (1989a) showed with idealized seamounts that when the height of the seamount or the stratification increases, the tendency for bottom trapping increases. The SBs with an average $N = 2.2\,\mathrm{x}\,10^{-3}\,\mathrm{s}^{-1}$ (1.26 cph) over the slope of a characteristic length $1/k_h = 48\,\mathrm{km}$ gives a Burger number $B \sim 0.08$. Brink (1989a) found that when stratification is weak, the dynamics are essentially barotropic. This is the case for low B and the shown depth-independent tidal current in the SBs (Figure 11a). For the semidiurnals, no zero crossing occurs at the slope, which suggests that only the gravest mode is present from the results of Brink (1989a). The YPSs has a slightly larger $N = 2.8\,\mathrm{x}\,10^{-3}\,\mathrm{s}^{-1}$ (1.60 cph) and $1/k_h = 83\,\mathrm{km}$, which gives a smaller $B \sim 0.02$, and Figure 16c,d show one zero-crossing in its along-shelf current. Similarly, YPNs and NBSs have $B < 0.04$ over the slope region of approximately $1/k_h = 50\,\mathrm{km}$ with a similar buoyancy frequency as the YPSs. The tendency of the barotropic structure of the velocity and curving towards the topography at the bottom of the shelf envelops through the sections except for SBs. In addition, zero to one zero-crossing along the sections suggests that the gravest mode and the first baroclinic modes are present. The weak stratification seems to only trap a portion of the velocity structure at the bottom. The YPSs, YPNs and NBSs have their plateau

and shelf height (h_0, elevation from deep ocean) of approximately between 2200 and 2500 m, whereas SBs has a shelf height of 1200 m. With a small Burger number, the topographic height might have larger importance of the produced vertical structure of the baroclinic current in each section. The tidal excursion parameter through the four analyzed sections is much less than unity (maximum 0.025), and therefore, one expects that the tides are mainly linear. This indicates that the generation of solitary waves, bores and lee waves is less probable as they are known for their non-linearity (Kang and Fringer, 2012).

5.4 Comparison with earlier investigations at the Yermak Plateau

An Earlier investigation of tidal conversion rates and internal wave energetics in the YP region has been performed with the global ocean circulation and tide model simulator STORMTIDE (Fer et al., 2015). This linear and hydrostatic numerical model that implicitly resolves mesoscale ocean circulation and without internal wave drag has conversion rates in deep ocean in the range of previous estimates (Fer et al., 2015). The STORMTIDE M_2 barotropic energy flux is very similar in direction and magnitude to what is found here (Figure 13a). In contrast, the STORMTIDE K_1 barotropic HKE energy flux has a different direction with the fluxes moving towards north at the center of the plateau with an off-shelf direction at the northern flank and a slightly on-shelf direction at the southern flank. These results from the STORMTIDE model are from January when the stratification and the ocean response can be different than employed in this study. In addition, coarser resolution ($5-10$ km in the horizontal and 40 vertical depth levels) (Fer et al., 2015) would not be able to resolve the contribution from smaller scale dynamics into the energetics. Also note that the ROMS fields analyzed here are initiated and forced by boundary conditions from a global model, which will differ from the STORMTIDE. The barotropic HKE energy flux between the models is on the same order. In the present analysis, the K_1 barotropic energy flux (Figure 13c) circulates over the plateau with a strength and direction following the surface displacement (Figure 5c). This clockwise circulation and trapping of tidal energy suggests a resonance at the K_1 frequency as the tide takes approximately one forcing period to propagate around the perimeter of the Plateau. This cause favors the enhancement of energy conversion and dissipation at the northern and southern flanks. Then the local amplification by the periodic tidal forcing at least partially accounts for the generation of high-frequency wave packets and induced diapycnal mixing (Padman et al., 1992). The O_1 has a different barotropic energy flux direction at the northern flank of the YP (Figure 13d), but still in a circulation, in which the resonance and the favorable on-shelf

direction generates intensified baroclinic energy flux.

The regions of weak energy conversion around the plateau (Figure 14a) do not always correlate with the energy conversion of the M_2 constituents at the YP produced by the STORMTIDE model. Likewise, the baroclinic energy flux distribution differs. These values are small over the plateau compared to the strongly tidal forced Monterey Bay Area (Kang and Fringer, 2012) with values reaching $0.2\,\mathrm{W\,m^{-2}}$. The difference from STORMTIDE also suggests that the results can be sensitive to changes in the stratification.

The K_1 energy conversion produced by the STORMTIDE over the YP is similar in showing the hotspot at the northern and southern flanks, but the conversion rates presented here are around one order of magnitude larger and are confined to one region. Likewise, the K_1 baroclinic energy flux at the hotspots is approximately 2 times larger, about $4000\,\mathrm{W\,m^{-1}}$, directed mostly off-shelf (Figure 14c) compared to a more along-shelf direction for the STORMTIDE model. For comparison, baroclinic energy fluxes are $5000\,\mathrm{W\,m^{-1}}$ over the Monterey Submarine Canyon (Kunze et al., 2002) and $2400\,\mathrm{W\,m^{-1}}$ over the Great Meteor Seamount (Gerkema and van Haren, 2007). At the northern flank hotspot, approximately at bottom depths of 2000 m, the energy conversion rate ranges between $0.05 - 0.10\,\mathrm{W\,m^{-2}}$ that is comparable with $0.05\,\mathrm{W\,m^{-2}}$ produced by the STORMTIDE model. Energy dissipation has been observed with microstructure measurements down to 520 m depth at the southern flank in summer 2007 (Fer et al., 2010). Depth-integrated energy dissipation was typically on the order of $10^{-3}\,\mathrm{W\,m^{-2}}$ which is comparable to the lower values shown in Figure 15.

For water depths between 1500 m and 2000 m, the Coordinated Eastern Arctic Experiment (CEAREX) showed a maximum $0.24\,\mathrm{m\,s^{-1}}$ diurnal cross-shelf current on the northern flank for the upper 300 m. The cross-shelf diurnal current was 2.4 times larger than the along-shelf diurnal current (Padman et al., 1992) which corresponds well with Figure 18c,d. Hunkins (1986) showed diurnal current amplitudes up to $0.15\,\mathrm{m\,s^{-1}}$ from the ice drifting camp, Fram IV, on the northern flank of YP down to 300 m depth for bottom depths of 2000 m (Padman et al., 1992). This is comparable with the K_1 and O_1 tidal current amplitude ($\mathbf{u_a}$) of approximately $0.1\,\mathrm{m\,s^{-1}}$ and $0.06\ \mathrm{m\,s^{-1}}$, respectively at this position (not shown). This agrees with earlier current meter observations presented by Hunkins (1986) where the diurnal tidal ellipses are aligned in the cross-shelf direction of the region.

5.5 Energy conversion region with off-shelf baroclinic energy flux

5.5.1 Yermak Plateau

The diurnal conversion rate at the northern flank of the YP is strong. The trapped and radiating K_1 internal tides around Izu-Oshima Island located off Sagami Bay (Japan) show comparable energy conversion rates up to $0.8\,\mathrm{W\,m^{-2}}$, with contributing factors as resonance interactions from internal tide propagation around the islands and generation of high frequency internal wave packets due to either shoaling of the barotropic wave or lee-wave generation (Masunaga et al., 2017). At the northern flank of the YP, the K_1 baroclinic energy flux is not transported around the plateau since the baroclinic energy flux is mostly directed off-shelf (Figure 14) in complete difference to the K_1 trapped internal tides around Izu-Oshima Island. The maximum baroclinic energy flux is $11\,\mathrm{W\,m^{-2}}$ for the K_1, which is comparable to the values found by simulating asymmetric Gaussian shaped topographies representing the Hawaiian Ridge (Holloway and Merrifield, 1999). In that study, the internal waves are free to propagate with strong baroclinic energy flux emanating from the slope with a pronounced beam pattern even after 250 km from the ridge.

In the eastern region of the Mendocino Ridge (eastern Pacific Ocean), the dissipation in the subinertial K_1 simulation decays by two orders of magnitude close to the surface with corresponding low currents (Musgrave et al., 2017). Criteria for spatial separation of super- and sub-inertial baroclinic tides were considered in a numerical study by Tanaka et al. (2013). Here, the maximum velocity for bottom trapped internal waves occurs at the bottom, whereas the maximum for freely propagating internal waves is in the intermediate layer with a velocity structure that detaches from the bottom in the form of a beam. At the YP and NBS, a strong convergence of baroclinic energy flux is seen both in the upper and lower layer separated with a minimum in between (Figure 19c). Each of these two intensified layers has a maximum baroclinic energy flux at the boundaries. Their off-shelf baroclinic energy flux direction and magnitude are similar and the decrease of density amplitude's phase with depth is nearly constant from the surface to the minimum baroclinic energy flux for the surface trapped energy. Below, with a 40° change of phase from above, the phase is nearly constant for the bottom trapped energy.

The cause of off-shelf intensified subinertial baroclinic energy flux in the bottom and the upper water column is not fully clarified. Approximately 100 % of the converted barotropic to baroclinic energy is used up for dissipation within each grid cell for each constituent and subdomain (Table 1), making the baroclinic radiation along isobaths negligible. One explanation

can be that small changes in the steepness of the topographic slope would generate waves with changed trapped wave modes, inhibiting along-shelf radiation. The trapped wave flux would converge at these places, and also when the topography varies in the along isobath direction. As the baroclinic energy is generated, the fluxes may be constrained for propagating along the slope due to the topographic corrugations, and therefore, the flux can only travel a short distance in the across shelf distance for constant depth until the conservation of vorticity initiates. This would produce a large change in the cross-slope baroclinic velocity which could be the reason for the large off-shelf K_1 baroclinic energy flux at the northern flank of the YP.

5.5.2 Nansen Basin Slope

The same reason for the off-shelf K_1 baroclinic energy flux at the northern flank of YP is applicable for the M_2 at the NBS. Here, the slope changes in steepness along the shelf and with a relatively large change of the isobath direction towards north. Unlike at the YP, here the M_2 baroclinic energy flux at 500 m and 1000 m has a considerable along-shelf component compared to the cross-shelf, shown in Figure 23a, revealing the influence of the M_2 bottom intensified baroclinic energy flux seen in the section between these depths. This means that the surface baroclinic energy flux is directed in the cross-shelf direction whereas the bottom intensified flux also has a comparable along-shelf direction. This is confirmed with larger values of cross-shelf baroclinic energy flux (not shown) originating from the surface and slightly less values at the bottom slope hotspots for both M_2 and S_2 constituents. In the conversion region with bottom velocity intensification, the density amplitude's phase generally decreases with depth, meaning an upward phase propagation which can be an indication of existing semidiurnal trapped waves originating from the bottom. In approximately the same section location as NBSs, Renner et al. (2018) found enhanced shear of several M_2 overtides indicating nonlinear interaction of the M_2 tide with the topography. The existence of trapped internal waves may be the reason for the observed M_2 baroclinic bottom intensification in NBSs.

The M_2 depth-integrated and time-averaged barotropic to baroclinic energy conversion is entirely dissipated along the section except for the surface intensification at a distance of 140 km. This small remainder of converted energy could be the reason for the weak baroclinic energy propagating downward into deeper ocean. Where the bottom intensification occurs, the depth-integrated and time-averaged dissipation is much larger than the converted energy. This may be attributed to trapped internal waves propagating along the wave guide along the slope from their generation site or to baroclinic bottom drag. Where the along-shelf baroclinic energy flux

is negative, the corresponding dissipation is also negative indicating additional contribution to the simplified energy balanced used to infer the dissipation rate.

5.6 Heat loss and water mass transformation in the AOBC

The Arctic Ocean Boundary Current (AOBC) is typically observed with warm AW over the upper slope and the shelf break, co-located with the energetic sites of conversion rates, dissipation and mixing. The dissipation of baroclinic tidal energy, particularly the local dissipation of topographically trapped waves, plays an important role in the transfer of energy to vertical mixing processes resulting in substantial heat-flux contributing to the cooling of the AW north of Svalbard. At the northern and southern flank of YP, the stratification is weak below ∼500 m depth. An average internal tidal displacement amplitude of $\zeta_a > 100$ m is produced in the bottom trapped energetic layer of Figure 17c and 19c. This is comparable to the displacement of internal tides on the Oregon Continental Slope (Martini et al., 2011). In the upper layer, above ∼500 m, the average displacement is 6 m. At the NBS slope, typical internal displacement of 20 m occurs.

At the SB the AW is still at the surface without any pycnocline that inhibits upward heat flux towards the atmosphere. In the other subdomains, the cooling of the AW core temperature and salinity depends on the strength of the forcing to create turbulence within the pycnocline. In summer 2007 at the southern flank of YP, Fer et al. (2010) found strong observed stratification between 17 and 80 m over approximately 1000 m bottom depth that prohibited mixing across the pycnocline in the marginal ice zone. Close to the station 1 of Fer et al. (2010) at 1000 m bottom depth along the YPSs, similar $N > 5$ cph or 8.7×10^{-3} s^{-1} (maximum 9.8 cph or 1.7×10^{-2} s^{-1}) is found in the pycnocline layer between 8 and 50 m with a shallow upper mixed layer of 6 m. The shallow mixed layer presented in Figure 4c is similar to the mixed layer of the N_ICE2015 drifting expedition in May 2015 in the same region which took place during large basal sea ice melt driven by ocean heat flux from the AW. This would produce a freshening of the upper surface layer and an increased buoyancy. The marginal ice zone in autumn 2017 is located close to the southern flank of YP. The conversion and dissipation rate of K_1 is 0.1 W m^{-2} over the 1000 m bottom depth of Figure 17c. As the pycnocline is strong in this region, the upward heat flux towards the surface would be weak. Cooling of the AW can occur due to lateral heat exchange with the colder ambient waters, or downward heat flux from the AW core. The downward heat flux would contribute to a warming of the Arctic Intermediate Water that escapes with the East Greenland Current and a loss term in the heat budget of the Arctic basin (Fer et al., 2010).

North of the YPSs, the AW is advected below the ice pack, and northern flank of the YP is

covered with sea ice in the autumn period. As a consequence, we expect much lower heat flux to the atmosphere as the wind stress driven mixing in the surface layer is weakened. At the northern flank, the mixed layer is 10 m deep for bottom depths of 2000 m in comparison to 30 m mixed layer from April observations of the CEAREX O Camp (Padman and Dillon, 1991) in the same region and over equal bottom depth. The CEAREX O Camp in April 1989 followed a path along the 2000 m isobath of the northern flank of YP. A similar temperature in Figure 4e of 2°C at the same depth of 250 m is observed in the O Camp. Over approximately 2000 m bottom depth, the O Camp showed a maximum $N = 5\,\text{cph}$ ($8.7\,\text{x}\,10^{-3}\,\text{s}^{-1}$) at a depth of 120 m in comparison with $N = 5.5\,\text{cph}$ ($9.6\,\text{x}\,10^{-3}\,\text{s}^{-1}$) between 22 and 50 m depth in the YPNs. The dissipation in the O Camp was found in two distinct regions, in the near-surface layer as a result of stress from ice-water interaction, and in the pycnocline, where the maximum energy in the isotherm displacements occurred during its drift (Padman and Dillon, 1991). The dissipation in the pycnocline layer ($\epsilon > 10^{-7}\,\text{W}\,\text{kg}^{-1}$) had a significantly near-diurnal energy signal with broader bandwidth than in the near-surface region. This corresponds to the depth-integrated and time-averaged of the YPNs of approximately $1.5\,\text{x}\,10^{-7}\,\text{W}\,\text{kg}^{-1}$ (Figure 19c) at 2000 m bottom depth. From this, the O Camp pycnocline dissipation was suggested to be related to the enhanced tidal current over the bottom topography. The convergence of calculated heat flux of $25\,\text{W}\,\text{m}^{-2}$, similar to heat fluxes found by Fer et al. (2015) in the YP region, was estimated to warm the upper pycnocline region, vanishing at the base of the mixed layer, near 80 m (Padman and Dillon, 1991). The small fraction of upward heat flux that reaches the surface layer would lead to a slightly warmer mixed layer over the slope region as the upward heat flux is much larger than the flux over deeper water. At the topographically enhanced diurnal tidal regions, mixing would occur due to intense shear-driven currents, whereas outside, mixing would typically occur due to double-diffusive processes (Padman and Dillon, 1991). This topic is beyond the scope of this thesis.

Close to the NBSs, data from an array of three deployed moorings over 1 year show a relatively stable upper layer of 100 m with temperature between 2 and 4°C in the late autumn and early winter (Renner et al., 2018). Sea ice was present at the beginning of February 2013 with a pycnocline established between 20 and 100 m that persisted until sea ice disappeared in August. Figure 4g (NBSs) shows a conservative temperature of −1.4°C in the 22 m upper mixed layer with a pycnocline between 30 and 140 m with $N > 2.5\,\text{cph}$ ($4.4\,\text{x}\,10^{-3}\,\text{s}^{-1}$). Between 2008 and 2013, transects of measured dissipation of turbulent kinetic energy have been taken at the shelf break north-east of Svalbard through dense ice cover and more open water conditions

(Rippeth, 2015). There and over bottom depths of $500 - 2000\,\mathrm{m}$, dissipation of tidal origin was estimated between $0.01 - 0.06\,\mathrm{W\,m^2}$ under conditions of both with and without dense ice cover ($> 70\,\%$). The NBSs (Figure 26a) is in the lower range of these observations, with a maximum of $0.02\,\mathrm{W\,m^2}$ close to the 1000 m isobath.

The distribution of AW heat fluxes would eventually contribute to spatial inhomogeneity in response to climate change in the Arctic Ocean sea ice environment with impacts on sea ice cover and intensified heat transfer from the atmosphere in the region of rough topography and efficient tidal conversion. In reaction to sea ice retreat, the tides have the possibility to increase the regional scale of turbulent mixing to certain regions of rough topography where at present flows are too small to produce instability and mixing. The local mixing contributes to the removal of heat from the AW that affects the heat budget of the Arctic Ocean in changing the mass properties of the AW in the inflowing AOBC.

5.7 Limitation of autumn stratification

The analysis is limited to one autumn month average stratification which gives the possibility that the internal wave activity can be different in the other seasons as the stratification and forcing will be different. The effect on the AW core temperature and salinity depends on the strength of the forcing to create turbulence within the pycnocline. The surface mixed layer is shallow during large melting events of basal sea ice, whereas during freezing, the surface mixed layer depth increases. Brine release during ice freezing weakens the stratification in the upper layer, which would affect the depth where tidal induced dissipation and propagation of internal waves occur. Therefore, weaker stratification would decrease upper layer dissipation. This correlates with the study of internal waves in the southeastern Bering Sea by Tanaka et al. (2013), who switched between weak upper layer ($< 100\,\mathrm{m}$) stratification ($N \sim 1.5\,\mathrm{cph} = 2.6\,\mathrm{x}\,10^{-3}\,\mathrm{s^{-1}}$) during winter and stronger ($N \sim 6\,\mathrm{cph} = 1.0\,\mathrm{x}\,10^{-2}\,\mathrm{s^{-1}}$) during summer. There, the reached off-shelf distance and the off-shelf velocity amplitude of the freely propagating internal waves was reduced during weak stratification in the upper layer. Locally to the place of internal wave generation, minimal change was shown in the tidal velocity shear at the bottom of the shelf in terms of changing upper layer stratification (Tanaka et al., 2013).

In the present study, the YPSs has a shallow mixed layer, most likely due to basal ice melting during spring and summer time. The large stratification in this region would enhance the upper layer baroclinic velocity field as the generation of baroclinic energy increases with larger cross-shelf velocity amplitude. The time of freeze-up would leave a deeper mixed layer

that induces less dissipation from tidal activity in the upper layer, whereas in the bottom layer less or no reduction in baroclinic dissipation is expected. At the northern flank of YP, the sea ice cover is present throughout the year, and reduced wind stress transfer limited by the sea ice cover would cause less vertical mixing and heat transfer from the upper layer. Not only does freeze-up and ice melting change the stratification, but also the seasonal variations of the AW transport and temperature including a steadily warming of the West Spitsbergen Current (WSC) on long-term (decadal) trends. A temperature increase of 0.8°C over 13 years was found in the WSC (Beszczynska-Möeller et al., 2012). The variability in the AW temperature and volume transport in the Fram Strait is characterized by a strong seasonal signal in the upper ~ 250 m to the degree that AW is present. With data from 1997−2010, Beszczynska-Möeller et al. (2012) observed maximum temperature of AW in the WSC in early autumn (September−October). This would give stronger stratification if ice cover with ice melting is present. When the water column is occupied only by AW, as is the development at the shallowest depths in the YPSs (Figure 4c), where bottom temperatures are slightly below 2°C, the bottom stratification would no longer exist. This would decrease the generation of bottom trapped internal waves. As the surface layer is shallow and with an incoming larger volume of AW in a future release, a retreat of the marginal ice zone would change the temperature and salinity at the southern flank towards weak stratification as shown in the SBs following up by weaker internal wave activity.

At the NBS, the surface temperature is approximately -1.4°C and is close to the marginal ice zone of this period. The AW is located below a cold surface mixed layer of 22 m, likely a result of the period of freeze-up. Therefore, the observed stratification is largest below late spring and early summer mixed layers (Renner et al., 2018). Whereas in winter, observed mixed layer is as deep as 100 m. A thinner surface mixed layer because of basal sea ice melting and a shallower placed AW core temperature would benefit internal wave generation as the stratification increases. More efficient transfer of wind energy to the upper mixed layer can generate baroclinic currents and internal waves as the momentum travels over shallower mixed layer. This will be important in marginal ice zones as the wind speed generally increases from transitioning in ice to open ocean underlay where upwelling or downwelling can take place (Carmack and Chapman, 2003).

6 Summary and conclusions

In this study, we address the tidal forcing and internal tide generation over continental shelves and plateaus in the vicinity of Svalbard using a high-resolution (2.5 km) Regional Ocean Model System (ROMS) setup. Fields are analyzed to quantify linear and hydrostatic form of the depth-integrated and time-averaged barotropic and baroclinic energy equations. The domain is separated into three subdomains of interest, denoted the Spitsbergen Bank (SB), the Yermak Plateau (YP) and the Nansen Basin Slope (NBS), each characterized by different tidal impacts and regional importance. The distribution of the tidal energy conversion rates and dissipation are computed for each subdomain. The results are based on one autumn month in 2017, but with realistic and spatially varying stratification. Four tidal constituents (M_2, S_2, K_1 and O_1) are forced and analyzed separately. Harmonic analysis of the model fields is used to quantify the energetics of linear internal tides, the distribution of barotropic tidal energy conversion to baroclinic energy, baroclinic dissipation and baroclinic radiation.

Tidal energetics are enhanced in distinct regions. The YP is dominated by the luni-solar and the principal lunar diurnal tides, and the continental shelf-slope northeast of Svalbard by the semidiurnal tides. The tidal forcing has the largest impact in the generation of baroclinic motion where on- and off-shelf barotropic energy flux occurs. This cross-isobath forcing generates significant baroclinic energy concentrated at the slopes. In general, weak radiation of baroclinic energy occurs at the upper part of the continental slope or the flanks of the YP, whereas at the central part of the slope, conversion rates exceed dissipation rates. At the lower slope, more baroclinic energy is dissipated than generated, especially for the diurnal constituents at the YP. Why the off-shelf directed baroclinic energy flux at the northern flank of the YP and the NBS slope occurs is not fully understood. This direction of baroclinic energy flux is not seen at the SB where the low stratification with more along-shelf directed barotropic energy flux and less topographic steepness (compared to the YP and NBS) are probably the reason for the weak energy conversion rates and baroclinic energy flux.

The diurnal tidal currents ($0.1 - 0.3\,\mathrm{m\,s^{-1}}$) are particularly strong over the shelf breaks and the central YP, and tend to increase towards shallower regions. No clear bottom intensification is seen in the tidal velocity or the velocity amplitude. The topographic tidal interaction dominates over the benthic stress, whereas the stress towards the sea ice has not been investigated.

The modeled depth-integrated and time-averaged baroclinic dissipation rate ($0.1 - 0.5\,\mathrm{W\,m^2}$ at the YP and $0.02\,\mathrm{W\,m^{-2}}$ at the NBS) supports previous observations showing strong mixing

at these hotspots. Exponential decay in both current and baroclinic energy flux from regions of strong barotropic to baroclinic energy conversion is seen. Generally, a substantial part of the converted energy dissipates locally in the $1.5 - 2.5$ km isobath range (central and lower slope), implying an important contribution to vertical mixing and the evolution of water mass properties in the region. This local mixing can initiate water mass modification if the stratification becomes too weak between the surface mixed layer and the warm AW. The slopes of the YP and the NBS have a shallower surface and bottom mixed layer where the subducted AW is found, indicating regions of melting since the stratification is stronger and the upper water is close to the freezing temperature. Further investigation of trapped internal waves and their sensitivity to changing stratification due to e.g., sea ice melting, increasing temperature and shallower upper mixed layer, is needed.

Subinertial internal waves are trapped and can only propagate freely and redistribute their energy along a boundary. Radiation is minimal relative to the numerical resolution and the model cannot resolve if there is a local redistribution. Variations in topography can influence the trapped internal wave propagation along topographic waveguide as each tidal frequency gives different dispersion properties. The YP has a dominant diurnal tidal motion with clockwise rotation and considerable baroclinic energy that at least indirectly is responsible for the intensification of energy dissipation over shelf-slopes. The enhanced diurnal activity is consistent with tidal resonance as the K_1 tide takes one cycle to propagate around the perimeter of the YP. In strong conversion regions of each subdomain, the tidal phase and amplitudes are nearly barotropic, indicating the possibility of a stronger barotropic component in higher modes in which the astronomical force can project onto.

At the YP, the sum of the volume-integrated and time-averaged M_2, S_2, K_1 and O_1 total baroclinic tidal dissipation is 918 MW (7.6 % of the barotropic radiation) compared to the other subdomains where the NBS has 81 MW (1.7 %) and the SB with less than 1 MW (<1 %). The YP is the most efficient at diurnal baroclinic energy generation (∼26 %) whereas the NBS gives the largest contribution from the M_2 constituent with 70 MW.

High resolution and realistic simulations are crucial to obtain a realistic distribution of internal tide energetics. Although the domain-averaged barotropic to baroclinic energy conversion rate and baroclinic energy dissipation from a coarser resolution global tidal model are similar to the results from the ROMS model, they differ in locations and distribution of these enhanced energetic terms. While these disparities are partly due to variations in the amplitude and the forced direction of the barotropic forcing, higher resolution simulations improve the representation of

the near-bottom and surface stratification over the topographic slope.

This study contributes to an improved description of the diurnal and semidiurnal tidal currents and how they interact with bathymetry around Svalbard. A more accurate description of tidal energy conversion and pathways of this energy to vertical mixing will lead to better representation of water mass transformations in the region and more reliable predictions of Arctic Ocean climate change. However, improved methods for analysis are needed to allow for the trapped-nature of internal tides at these latitudes and to accordingly quantify the associated conversion and dissipation rates. Furthermore, the role of tidally-driven nonlinear internal waves and non-steady lee waves merits further studies that require higher resolution numerical models.

7 References

Alford, M. H., MacKinnon, J. A., Nash, J. D., Simmons, H., Pickering, A., Klymak, J. M., Pinkel, R., Sun, O., Rainville, L., Musgrave, R., Beitzel, T., Fu, K.-H., and Lu, C.-W. (2011). Energy flux and dissipation in luzon strait: Two tales of two ridges. *Journal of Physical Oceanography*, 41(11):2211–2222.

Bentsen, M., Evensen, G., Drange, H., and Jenkins, A. D. (1999). Coordinate transformation on a sphere using conformal mapping. *Monthly Weather Review*, 127(12):2733–2740.

Beszczynska-Möeller, A., Fahrbach, E., Schauer, U., and Hansen, E. (2012). Variability in atlantic water temperature and transport at the entrance to the arctic ocean, 1997-2010. *ICES Journal of Marine Science*, 69:852–863.

Boyd, T. J. and D'Asaro, E. A. (1994). Cooling of the west spitsbergen current: Wintertime observations west of svalbard. *Journal of Geophysical Research: Oceans*, 99(C11):22597–22618.

Brink, K. H. (1989a). The effect of stratification on seamount-trapped waves. *Deep Sea Research Part A. Oceanographic Research Papers*, 36(6):825–844.

Brink, K. H. (1989b). Energy conservation in coastal-trapped wave calculations. *Journal of Physical Oceanography*, 19(7):1011–1016.

Carmack, E. and Chapman, D. C. (2003). Wind-driven shelf/basin exchange on an arctic shelf: The joint roles of ice cover extent and shelf-break bathymetry. *Geophysical Research Letters*, 30(14).

Carmack, E., Polyakov, I., Padman, L., Fer, I., Hunke, E., Hutchings, J., Jackson, J., Kelley, D., Kwok, R., Layton, C., Melling, H., Perovich, D., Persson, O., Ruddick, B., Timmermans, M.-L., Toole, J., Ross, T., Vavrus, S., and Winsor, P. (2015). Toward quantifying the increasing role of oceanic heat in sea ice loss in the new arctic. *Bulletin of the American Meteorological Society*, 96(12):2079–2105.

Carter, G. S., Merrifield, M. A., Becker, J. M., Katsumata, K., Gregg, M. C., Luther, D. S., Levine, M. D., Boyd, T. J., and Firing, Y. L. (2008). Energetics of m2 barotropic-to-baroclinic tidal conversion at the hawaiian islands. *Journal of Physical Oceanography*, 38(10):2205–2223.

Chassignet, E. and Verron, J. (2006). *Ocean weather forecasting: An integrated view of oceanography*. Springer.

Chen, Z.-W., Xie, J., Xu, J., Zhan, J.-M., and Cai, S. (2013). Energetics of nonlinear internal waves generated by tidal flow over topography. *Ocean Modelling*, 68:1–8.

Crews, L., Sundfjord, A., and Hattermann, T. (2019). How the yermak pass branch regulates atlantic water inflow to the arctic ocean. *Journal of Geophysical Research: Oceans*, 124(1):267–280.

Cushman-Roisin, B. and Jean-Marie, B. (2011). *Introduction to Geophysical Fluid Dynamics: Physical and Numerical Aspects*, page 789. Academic Press.

Denman, K. L. (1976). Covariability of chlorophyll and temperature in the sea. *Deep Sea Research and Oceanographic Abstracts*, 23(6):539–550.

Dong, J., Robertson, R., Dong, C., Hartlipp, P. S., Zhou, T., Shao, Z., Lin, W., Zhou, M., and Chen, J. (2019). Impacts of mesoscale currents on the diurnal critical latitude dependence of internal tides: A numerical experiment based on barcoo seamount. *Journal of Geophysical Research: Oceans*, 124(4):2452–2471.

Doodson, A. T. and Lamb, H. (1921). The harmonic development of the tide-generating potential. *Proceedings of the Royal Society of London. Series A, Containing Papers of a Mathematical and Physical Character*, 100(704):305–329.

Egbert, G. D., Bennett, A. F., and Foreman, M. G. G. (1994). Topex/poseidon tides estimated using a global inverse model. *Journal of Geophysical Research: Oceans*, 99(C12):24821–24852.

Egbert, G. D. and Erofeeva, S. Y. (2002). Efficient inverse modeling of barotropic ocean tides. *Journal of Atmospheric and Oceanic Technology*, 19(2):183–204.

Egbert, G. D. and Ray, R. D. (2001). Estimates of m2 tidal energy dissipation from topex/poseidon altimeter data. *Journal of Geophysical Research: Oceans*, 106(C10):22475–22502.

Falahat, S. and Nycander, J. (2015). On the generation of bottom-trapped internal tides. *Journal of Physical Oceanography*, 45(2):526–545.

Fer, I., Müller, M., and Peterson, A. K. (2015). Tidal forcing, energetics, and mixing near the yermak plateau. *Ocean Science*, 11(2):287–304.

Fer, I., Skogseth, R., and Geyer, F. (2010). Internal waves and mixing in the marginal ice zone near the yermak plateau. *Journal of Physical Oceanography*, 40(7):1613–1630.

Garrett, C. and Kunze, E. (2007). Internal tide generation in the deep ocean. *Annual Review of Fluid Mechanics*, 39(1):57–87.

Gerkema, T. and van Haren, H. (2007). Internal tides and energy fluxes over great meteor seamount. *Ocean Science*, 3(3):441–449.

Gerkema, T. and Zimmerman, J. (2008). An introduction to internal waves.

Gill, A. E. (1982). *Atmosphere–Ocean Dynamics*, volume 30. Cambridge University Press.

Griffies, S. M., Böning, C., Bryan, F. O., Chassignet, E. P., Gerdes, R., Hasumi, H., Hirst, A., Treguier, A.-M., and Webb, D. (2000). Developments in ocean climate modelling. *Ocean Modelling*, 2(3):123–192.

Hibiya, T. and Nagasawa, M. (2004). Latitudinal dependence of diapycnal diffusivity in the thermocline estimated using a finescale parameterization. *Geophysical Research Letters*, 31(1).

Holloway, G. and Proshutinsky, A. (2007). Role of tides in arctic ocean/ice climate. *Journal of Geophysical Research*, 112(C4).

Holloway, P. E. and Merrifield, M. A. (1999). Internal tide generation by seamounts, ridges, and islands. *Journal of Geophysical Research: Oceans*, 104(C11):25937–25951.

Hunkins, K. (1986). Anomalous diurnal tidal currents on the yermak plateau. *Journal of Marine Research*, 44(19):51–69.

Huthnance, J. M. (1978). On coastal trapped waves: Analysis and numerical calculation by inverse iteration. *Journal of Physical Oceanography*, 8(1):74–92.

Kang, D. and Fringer, O. (2012). Energetics of barotropic and baroclinic tides in the monterey bay area. *Journal of Physical Oceanography*, 42(2):272–290.

Kelly, S. M., Nash, J. D., and Kunze, E. (2010). Internal-tide energy over topography. *Journal of Geophysical Research: Oceans*, 115(C6).

Koenig, Z., Provost, C., Sennèchael, N., Garric, G., and Gascard, J.-C. (2017). The yermak pass branch: A major pathway for the atlantic water north of svalbard? *Journal of Geophysical Research: Oceans*, 122(12):9332–9349.

Koentopp, M., Eisen, O., Kottmeier, C., Padman, L., and Lemke, P. (2005). Influence of tides on sea ice in the weddell sea: Investigations with a high-resolution dynamic-thermodynamic sea ice model. *Journal of Geophysical Research: Oceans*, 110(C2).

Kunze, E., Rosenfeld, L. K., Carter, G. S., and Gregg, M. C. (2002). Internal waves in monterey submarine canyon. *Journal of Physical Oceanography*, 32(6):1890–1913.

Kurapov, A. L., Egbert, G. D., Allen, J. S., Miller, R. N., Erofeeva, S. Y., and Kosro, P. M. (2003). The m2 internal tide off oregon: Inferences from data assimilation. *Journal of Physical Oceanography*, 33(8):1733–1757.

Li, Z., Storch, J.-S. v., and Müller, M. (2015). The m2 internal tide simulated by a 1/10 ogcm. *Journal of Physical Oceanography*, 45(12):3119–3135.

Manley, T. O. (1995). Branching of atlantic water within the greenland-spitsbergen passage: An estimate of recirculation. *Journal of Geophysical Research: Oceans*, 100(C10):20627–20634.

Martini, K. I., Alford, M. H., Kunze, E., Kelly, S. M., and Nash, J. D. (2011). Observations of internal tides on the oregon continental slope. *Journal of Physical Oceanography*, 41(9):1772–1794.

Masunaga, E., Fringer, O., Kitade, Y., Yamazaki, H., and Gallager, S. (2017). Dynamics and energetics of trapped diurnal internal kelvin waves around a midlatitude island. *Journal of Physical Oceanography*, 47.

Menze, S., Ingvaldsen, R. B., Haugan, P., Fer, I., Sundfjord, A., Beszczynska-Moeller, A., and Falk-Petersen, S. (2019). Atlantic water pathways along the north-western svalbard shelf mapped using vessel-mounted current profilers. *Journal of Geophysical Research: Oceans*, 124(3):1699–1716.

Meyer, A., Fer, I., Sundfjord, A., and Peterson, A. K. (2017). Mixing rates and vertical heat fluxes north of svalbard from arctic winter to spring. *Journal of Geophysical Research: Oceans*, 122(6):4569–4586.

Mohanty, S., Rao, A. D., and Latha, G. (2018). Energetics of semidiurnal internal tides in the andaman sea. *Journal of Geophysical Research: Oceans*, 123(9):6224–6240.

Müller, M., Batrak, Y., Kristiansen, J., Køltzow, M. A. Ø., Noer, G., and Korosov, A. (2017).

Characteristics of a convective-scale weather forecasting system for the european arctic. *Monthly Weather Review*, 145(12):4771–4787.

Müller, P., Holloway, G., Henyey, F., and Pomphrey, N. (1986). Nonlinear interactions among internal gravity waves. *Reviews of Geophysics*, 24(3):493–536.

Munk, W. H. and Wunsch, C. (1998). Abyssal recipes ii: Energetics of tidal and wind mixing. *Deep-Sea Res I*, 45:1977–2010.

Musgrave, R. C. (2019). Energy fluxes in coastal trapped waves. *Journal of Physical Oceanography*, 49(12):3061–3068.

Musgrave, R. C., MacKinnon, J. A., Pinkel, R., Waterhouse, A. F., Nash, J., and Kelly, S. M. (2017). The influence of subinertial internal tides on near-topographic turbulence at the mendocino ridge: Observations and modeling. *Journal of Physical Oceanography*, 47(8):2139–2154.

Nash, J. D., Alford, M. H., and Kunze, E. (2005). Estimating internal wave energy fluxes in the ocean. *Journal of Atmospheric and Oceanic Technology*, 22(10):1551–1570.

Padman, L. and Dillon, T. M. (1991). Turbulent mixing near the yermak plateau during the coordinated eastern arctic experiment. *Journal of Geophysical Research: Oceans*, 96(C3):4769–4782.

Padman, L., Plueddemann, A., Muench, R., and Pinkel, R. (1992). Diurnal tides near the yermak plateau. *Journal of Geophysical Research*, 97:12639–12652.

Plueddemann, A. J. (1992). Internal wave observations from the arctic environmental drifting buoy. *Journal of Geophysical Research: Oceans*, 97(C8):12619–12638.

Rainville, L., Lee, C., and Woodgate, R. (2011). Impact of wind-driven mixing in the arctic ocean. *Oceanography*, 24:136–145.

Renner, A. H. H., Sundfjord, A., Janout, M. A., Ingvaldsen, R. B., Beszczynska-Möller, A., Pickart, R. S., and Pérez-Hernández, M. D. (2018). Variability and redistribution of heat in the atlantic water boundary current north of svalbard. *Journal of Geophysical Research: Oceans*, 123(9):6373–6391.

Rippeth, T. P., Lincoln, B., Lenn, Y. D., Green, M., Sundfjord, A., and Bacon, S. (2015). Tide-mediated warming of arctic halocline by atlantic heat fluxes over rough topography. *Nature Geoscience*, 8:191–194.

Rippeth, T. P., Vlasenko, V., Stashchuk, N., Scannell, B. D., Green, J. A. M., Lincoln, B. J., and Bacon, S. (2017). Tidal conversion and mixing poleward of the critical latitude (an arctic case study). *Geophysical Research Letters*, 44(24):12,349–12,357.

Shchepetkin, A. and McWilliams, J. (2005). The regional oceanic modeling system (roms): a split-explicit, free-surface, topography-following- coordinate ocean model. *Ocean Modelling*, 9:347–404.

Simmons, H., Jayne, S., Laurent, L., and Weaver, A. (2003). Tidally driven mixing in a numerical model of the ocean general circulation. *Ocean Modelling*, 6:245–263.

Sirevaag, A. and Fer, I. (2012). Vertical heat transfer in the arctic ocean: The role of double-diffusive mixing. *Journal of Geophysical Research: Oceans*, 117(C7).

Smith, K. A., Merrifield, M. A., and Carter, G. S. (2017). Coastal-trapped behavior of the diurnal internal tide at o'ahu, hawai'i. *Journal of Geophysical Research: Oceans*, 122(5):4257–4273.

Staquet, C. and Sommeria, J. (2002). Internal gravity waves: From instabilities to turbulence. *Annual Review of Fluid Mechanics*, 34(1):559–593.

Tanaka, T., Yasuda, I., Tanaka, Y., and Carter, G. S. (2013). Numerical study on tidal mixing along the shelf break in the green belt in the southeastern bering sea. *Journal of Geophysical Research: Oceans*, 118(12):6525–6542.

Thomson, R. E. and Emery, W. J. (2014). *Data Analysis Methods in Physical Oceanography*. Elsevier, Boston, third edition.

Vlasenko, V., Stashchuk, N., and Hutter, C. (2012). *Baroclinic Tides: Theoretical Modeling and Observational Evidence*. Cambridge University Press.

Warner, T. T. (2011). *Numerical Weather and Climate Prediction*. Cambridge University Press.